



---

**Universidad de Valladolid**

FACULTAD DE MEDICINA

INSTITUTO DE OFTALMOBIOLOGÍA APLICADA

TESIS DOCTORAL:

**ACCOMMODATION: OPTICAL FUNCTION AND  
CRYSTALLINE LENS IMAGING**

Presentada por Enrique Gamba Urralburu para optar al grado de  
doctor por la Universidad de Valladolid

Dirigida por:  
Susana Marcos Celestino





**Universidad de Valladolid**

Impreso 2T

**AUTORIZACIÓN DEL DIRECTOR DE TESIS**

*(Art. 2.1. c de la Normativa para la presentación y defensa de la Tesis Doctoral en la UVa)*

Dña. SUSANA MARCOS CELESTINO, con D.N.I. nº 07954600G, Profesora de Investigación en el Instituto de Óptica "Daza de Valdés" del Consejo Superior de Investigaciones Científicas (CSIC)

como Directora de la Tesis Doctoral titulada "Accommodation: optical function and crystalline lens imaging" presentada por D. ENRIQUE GAMBRA URRALBURU alumno del programa CIENCIAS DE LA VISIÓN.

impartido por el departamento INSTITUTO UNIVERSITARIO DE OFTALMOBIOLOGÍA APLICADA, FACULTAD DE MEDICINA autoriza la presentación de la misma, considerando que la tesis presenta resultados originales y novedosos para la comprensión de la función acomodativa del ojo, utilizando tecnologías estado-del-arte (Óptica Adaptativa y Tomografía de Coherencia Óptica), con impacto en la comunidad científica, clínica e industrial, a través de publicaciones en revistas de alto impacto y comunicaciones en congresos.

Madrid, 29 de mayo de 2015

El Director de la Tesis,

Fdo.: Susana Marcos Celestino

SR. PRESIDENTE DE LA COMISIÓN DE DOCTORADO



1. INTRODUCTION.....	5
1.1. Motivation .....	5
1.2. The human eye.....	6
1.2.1. Cornea .....	6
1.2.2. Anterior chamber of the eye.....	7
1.2.3. Crystalline lens .....	8
1.2.4. The vitreous chamber.....	9
1.2.5. Retina .....	9
1.2.6. Axis of the eye.....	10
1.3. Optical quality of the eye .....	11
1.3.1. Wave aberrations .....	11
1.3.2. Zernike polynomials .....	12
1.3.3. Optical quality metrics.....	12
1.3.4. Aberrations on the human population.....	14
1.3.5. Techniques to evaluate the optical quality .....	15
1.3.6. Adaptive Optics .....	16
1.4. Accommodation.....	20
1.4.1. The accommodation mechanism .....	20
1.4.2. The accommodative response. Optometers.....	20
1.4.3. Changes of the human lens with accommodation .....	24
1.4.4. Pupil size and accommodation .....	26
1.4.5. Fluctuations of accommodation .....	27
1.4.6. Accommodative cues .....	28
1.4.7. Change of high order aberrations with accommodation.....	29
1.4.8. High order aberrations and accommodative lag.....	30
1.5. The aging crystalline lens: presbyopia and cataracts.....	31
1.5.1. Crystalline lens changes with age.....	31
1.5.2. Changes in ocular optical quality with age .....	33
1.6. Imaging of the crystalline lens .....	36
1.6.1. Ultrasound-based techniques.....	36
1.6.2. Purkinje imaging.....	36
1.6.3. Magnetic resonance imaging (MRI).....	37
1.6.4. Scheimpflug cameras .....	38
1.6.5. Optical coherence tomography.....	39
1.7. Open questions addressed in this thesis .....	46

1.8.	Goals .....	47
1.9.	Hypothesis .....	48
1.10.	Structure of the thesis .....	48
2.	METHODS .....	50
2.1.	Adaptive Optics system .....	51
2.1.1.	Description of the AO system .....	51
2.1.2.	AO-correction procedure .....	56
2.1.3.	Setting up of the system.....	58
2.1.4.	Automatic control interface.....	60
2.2.	Infrared recording retinoscope .....	63
2.2.1.	Apparatus .....	63
2.3.	Spectral-Domain OCT system.....	64
2.3.1.	Configuration of the system.....	64
2.3.2.	Control of the system.....	67
3.	INFLUENCE OF HIGH ORDER ABERRATIONS ON ACCOMMODATION PERFORMANCE.....	69
3.1.	Methods.....	70
3.1.1.	AO set-up .....	70
3.1.2.	Experimental protocol.....	71
3.1.3.	Subjects .....	72
3.1.4.	Data analysis.....	72
3.2.	Results .....	74
3.2.1.	Aberrations correction and induction .....	74
3.2.2.	Changes in pupil with accommodation and aberration condition .....	76
3.2.3.	Change of aberrations with accommodation.....	77
3.2.4.	Influence of aberrations on the accommodative response .....	81
3.2.5.	Influence of demand and aberrations on the fluctuations of accommodation .....	84
3.3.	Discussion .....	84
3.4.	Open question.....	87
4.	DYNAMIC ACCOMMODATION WITH SIMULATED TARGETS BLURRED WITH HIGH ORDER ABERRATIONS.....	88
4.1.	Methods.....	89
4.1.1.	Dynamic accommodation system.....	89
4.1.2.	Accommodative targets.....	89
4.1.3.	Experimental protocols .....	90

4.1.4.	Subjects .....	91
4.1.5.	Data processing .....	91
4.2.	Results .....	92
4.3.	Discussion .....	95
4.4.	Open question .....	96
5.	STATIC AND DYNAMIC CRYSTALLINE LENS ACCOMMODATION EVALUATED USING QUANTITATIVE 3-D OCT .....	97
5.1.	Methods.....	98
5.1.1.	OCT system.....	98
5.1.2.	Subjects .....	99
5.1.3.	Imaging protocols .....	99
5.1.4.	3-D image processing: denoising, segmentation, merging, distortion correction and surface fitting .....	100
5.1.5.	Data analysis.....	102
5.2.	Results .....	104
5.2.1.	3-D imaging of the segment.....	104
5.2.2.	Biometry and phakometry with dynamic central B-scan cross-sections	105
5.2.3.	Dynamics of the central B-scan.....	106
5.3.	Discussion .....	108
6.	CONCLUSIONS.....	111
6.1.	Achievements .....	111
6.2.	Conclusions .....	111
6.3.	Future work .....	112
7.	RESUMEN EN ESPAÑOL.....	114
7.1.	Introducción.....	115
7.1.1.	Objetivos .....	116
7.2.	Métodos.....	116
7.3.	Resultados .....	117
7.3.1.	Influencia de las aberraciones de alto orden en la acomodación.....	117
7.3.2.	Acomodación dinámica ante estímulos emborronados con aberraciones de alto orden .....	118
7.3.3.	Geometría estática y dinámica del cristalino durante la acomodación usando tomografía de coherencia óptica tridimensional cuantitativa .....	119
7.4.	Conclusiones.....	120
7.4.1.	Logros .....	120
7.4.2.	Conclusiones .....	121

7.4.3. Trabajo futuro.....	122
8. BIBLIOGRAPHY .....	123
<i>AGRADECIMIENTOS</i> .....	141

# 1. INTRODUCTION

## 1.1. Motivation

This thesis addresses the study of the accommodation process of the human eye using multiple techniques *in vivo*. Although the mechanism of accommodation was thoroughly described in 1855 by Helmholtz, there are still many open questions. A better understanding of accommodation will help to develop solutions for some visual problems, in particular presbyopia.

Presbyopia is the gradual loss of ability to focus near targets due to the physiological changes of the crystalline lens with age, which affects all people over the age of 45. Taking into account that the world's mean life expectancy is around 70 years -almost ten years more in the most developed countries-, presbyopia is a large public health issue and a business opportunity for ophthalmic companies. Today, new solutions for presbyopia are emerging that attempt the full restoration of accommodation by means of novel intraocular lenses. Although the technology is still far from success, the first generation accommodating-IOLs are already been commercialized.

Reliable techniques able to account for the accommodative response, the optical quality of the eye and their potential interactions are important to assess the accommodative mechanism in the young eye, among others, as a potential inspiration for new accommodation restoration solutions, and to evaluate performance of the new lenses. Adaptive Optics, a technique capable of manipulating and measuring optical aberrations dynamically, appears as an ideal tool to simulate the effect of potential corrections on the accommodative response. In this thesis, we used adaptive optics as well as computationally degraded images to study the influence of high order aberrations on the accommodative response.

Besides, imaging techniques able to quantify statically and dynamically the biometry and geometry of the anterior segment of the eye will provide information of the structural changes undergone by the accommodating crystalline lens, and relate those to the accommodative response measured by other techniques. In this thesis, we used custom developed optical coherence tomography to image and quantify geometrically the human crystalline lens as a function of accommodation, for the first time in 3D at high resolution and dynamically.

## 1.2. The human eye

Figure 1.1 shows a cross-section of the human eye. The eye is approximately spherical, with an average axial length of 24 mm in an adult human being. The eye projects images of the outer world on the retina. This section describes the main components of the eye -in particular those playing a role on image formation-

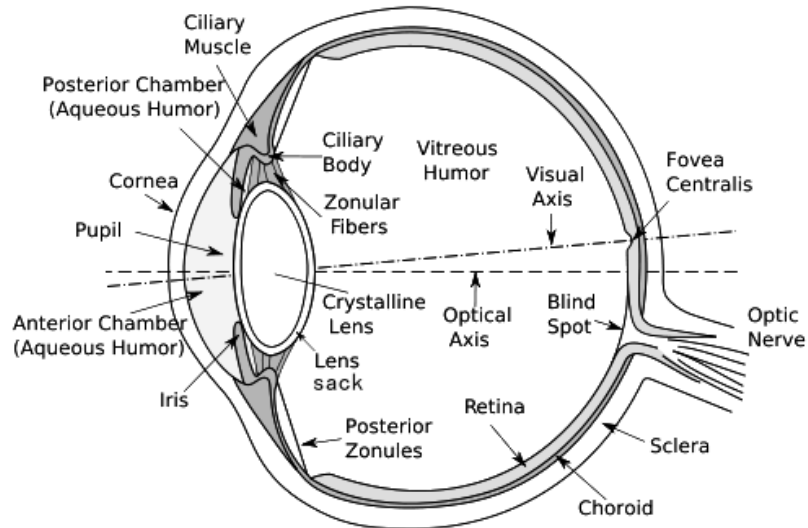


Figure 1.1. Cross-section of the human eye showing its main parts.

### 1.2.1. Cornea

The external part of the eye is a dense fibrous layer called the sclera, which gives structure to the eye. In its front part, the sclera becomes transparent allowing the entrance of the light to form the images. This transparent area, called the cornea, is thinner in the centre (~550  $\mu\text{m}$ ) than at the edge (~700  $\mu\text{m}$ ).

Histologically, the human cornea can be divided in 5 layers: epithelium, Bowman's membrane, stroma, Descemet's membrane and endothelium. Besides, the cornea is covered by a 4-10  $\mu\text{m}$  thick tear film layer [Prydal et al., 1992; Kaufman, 1998; Atchison and Smith, 2000] which maintains a smooth optical surface. Although each layer (including the tear film) has its own refractive index [Patel et al., 1995; Barbero, 2006], a mean value ( $n=1.376$ ) is typically used [Atchison and Smith, 2000]. Corneal inhomogeneities produce light scattering, what allows the use of optical-based instruments for the visualization of the cornea and, depending on the resolution of the instruments, its different layers.

Anatomically, a front view of the cornea reveals that its shape is not circular but ellipsoidal: its vertical and horizontal diameters are about 12 and 11 mm, respectively. The contour of both surfaces of the cornea can be approximated to a conicoid with rotational symmetry about the z-axis. Equation 1.1 provides the analytical expression for this conicoid [Malacara, 1988], where  $\rho$  are the polar coordinates,  $z$  is the axial coordinate,  $R$  is the radius of the surface and  $Q$  the conic constant.

$$\rho - 2zR + (1+Q)z^2 = 0 \quad \text{Equation 1.1}$$

The accessibility of the cornea -and most especially of its anterior surface- has led to the existence of multiple studies interested in determining its shape *in vivo* in a large number of subjects. Different techniques have been used to measure the geometry of both corneal surfaces, including keratometers [Patel et al., 1992; Lam et al., 1997], slit-lamps [Lowe and Clark, 1973; Royston et al., 1990], Placido disk videokeratoscopy [Campbell, 1997], Purkinje imaging systems [Royston et al., 1990; Dunne et al., 1992; Edmund et al., 1994; Garner et al., 1997] and Scheimpflug cameras [Dubbelman et al., 2002]. Some of these techniques are described in section 1.6 of this chapter.

On average, mean radii of curvature of the anterior and posterior surface of the cornea are around 7.7-7.8 mm and 6.4-6.5 mm, respectively. Besides, the mean values of asphericity are -0.2 for the anterior surface and 0.3 for the posterior one. Recently, Optical Coherence Tomography has been used to measure the geometry of the cornea [Ortiz et al., 2011; Karnowski et al., 2011], although those studies only included a small sample of subjects.

Most of the previous studies assumed that the corneal surfaces could be fitted by a conicoid. However, measurements of the corneal geometry reveal that the vertical meridians of the two surfaces are steeper than the horizontal ones [Atchison and Smith, 2000; Dubbelman et al., 2006], what produces astigmatism. Recent studies [Ortiz et al., 2011] have considered a biconicoid fitting for a more accurate description of the corneal surfaces.

The cornea contributes to about two-thirds of the optical power of the relaxed eye (~42 D) [Atchison and Smith, 2000]. The optical powers of the anterior and posterior surfaces are of about +49 D and - 6D, respectively [Charman, 1991]. The contribution of the anterior surface to the total optical power of the cornea is larger because the difference of refractive indices in the anterior interface is also larger.

### **1.2.2. Anterior chamber of the eye**

The space between the cornea and the crystalline lens is filled with the aqueous humor, a transparent fluid with a refractive index of 1.337. The iris is placed overlying the crystalline lens, “dividing” the cavity in two: the anterior chamber (between the cornea and the iris) and the posterior chamber (between the iris and the crystalline lens).

The iris is a structure made of thin elastic tissue with an opening in the center (the pupil) which is surrounded by a circular muscle or sphincter [Gold et al., 2010]. By varying its size, the pupil controls the amount of light reaching the retina. In bright light, the pupil gets smaller and the image projected on the retina is mainly diffraction-limited, while in a low-light environment the pupil dilates and the image sharpness depends highly on the optical aberrations of the eye [Campbell et al., 1960]. The pupil can change from about 2 mm to 8 mm in young eyes, but its maximum aperture decreases with age (miosis). The natural pupil can be artificially enlarged by means of mydriatics (pupil dilating drops). There are two main groups of mydriatics: parasympathetic antagonists (such as Tropicamide), which act by paralyzing the iris sphincter muscle but also paralyze the ciliary muscle and, therefore, the ability to accommodate; and sympathetic agonists (Phenylephrine), which act by stimulating the iris dilator muscle and, although dilating the pupil to a lesser extent, do not affect accommodation ability.

### 1.2.3. Crystalline lens

The crystalline lens (which for now on will be often referred to as the lens, as it is common practice in visual optics) is a biconvex transparent elastic structure situated behind the iris, suspended radially at its equator by the zonular fibers and the ciliary body (see Figure 1.1). The action of the ciliary body and the elasticity of the lens allow the ocular system to focus images on the retina. This accommodation process will be explained in depth in section 1.4.

The main parts of the lens are the following:

- *Lens Capsule*: the crystalline lens is embedded in this transparent membrane, which thickness varies from 3  $\mu\text{m}$  at the posterior pole to 14  $\mu\text{m}$  at the equator.
- *The lens epithelium*: a single line of cells lying on the anterior capsule and to the equator. Throughout life, these cells divide and elongate wrapping the older fibers, under the capsule and the epithelium, meeting at the sutures of the lens.. In the human, these sutures have a “Y” form in the embryonic lens, but the suture patterns become more complex with age, adopting a star-like appearance [Koretz et al, 1994].
- *Lens fibers*: the lens is composed of cells originated in the lens epithelium that have lost their nuclei and other intracellular organelles, arranging compactly from the oldest in the center to the newest in the periphery. Therefore, two main structures can be observed: (1) the nucleus, consisting of the older fibers (from the embryonic to the early adult nucleus), a less elastic region due to water loss, with the highest refractive index (about 1.41) [Charman, 1991]; and (2) the cortex, the peripheral part which comprises the youngest fibers, with a lower refractive index (up to 1.38). This “onion-like” layered structure leads to the so-called Gradient of Refractive Index (GRIN) of the lens, which plays an important role on the formation of the images on the retina.

Although the lens is less accessible than the cornea some studies have measured the geometry of the lens *in vivo* using different techniques (see section 1.6 for a description of this techniques): slit-lamps [Lowe, 1972; Brown, 1974], magnetic resonance imaging [Koretz et al., 2004], Purkinje imaging [Rosales et al., 2006] and Scheimpflug camera [Dubbelman, 2001a; Koretz et al., 2004, Rosales et al., 2006]. The contour of both surfaces of the crystalline lens can also be approximated to a conicoid, as is commonly done to describe the corneal geometry.

Dubbelman and Van de Heijde [2001a] reported an age-dependent expression for the anterior and posterior lens radius of human lenses *in vivo* based on corrected Scheimpflug measurements: for a 25-year-old subject, these equations provide 11.25 mm and 5.85 mm for the anterior and posterior lens radii, respectively. Rosales et al. [2006] measured the crystalline lens radii of curvature using both Purkinje and Scheimpflug imaging, reporting average values of 10.8 mm and 11.1 mm, and 6.7 mm and 6.1 mm from each technique, for anterior and posterior lens radius of curvature, respectively. Koretz et al. [2004] used both Scheimpflug and MRI in a comparative study, and obtained values of 11.90 mm and 5.58 mm for the anterior and posterior lens radii of curvature, respectively, with Scheimpflug photography, and 11.20 mm and 6.15 mm, respectively, with MRI.

Compiling the results from these studies, the anterior and posterior radii of curvature of the lens range from 10.8 to 11.9 mm and from 5.58 to 6.7 mm, respectively. Thus, the

accordance across studies is lower than for the cornea, due to the difficulty of measuring, *in vivo*, the lens surfaces behind other ocular structures.

The measurement of the asphericity of the crystalline lens surfaces *in vivo* is still challenging: MRI is not capable of measuring the asphericity due to its poor resolution ( $\pm 0.2$  mm), while the access of optical techniques to imaging the crystalline lens is limited by the diameter of the iris. Thus, there are few studies trying to assess the asphericity. Dubbelman and Van der Heijde [2001b] found that the curvature of the two surfaces of the lens steepened toward periphery, reporting an age-dependent value for the conic constant ( $k$ ) of  $-5.0 + 0.07 \cdot \text{age}$  for the anterior surface and  $-5.4 + 0.03 \cdot \text{age}$  for the posterior one. *Ex vivo* studies [Manns et al., 2004; Borja et al., 2008, Birkenfeld et al., 2014; Sun et al., 2014] have found that the anterior surface of the lens steepens toward periphery, in agreement with Dubbelman and Van der Heijde.

### 1.2.4. The vitreous chamber

The vitreous chamber is limited by the posterior surface of the lens and the retina (see Figure 1.1). It is filled with the vitreous humor, a transparent gel thicker than the aqueous humor but with the same refractive index that helps to maintain the structure of the eye. The vitreous is the largest chamber in the eye, allowing the optics of the eye to focus the image on the retina.

### 1.2.5. Retina

The retina is a light-sensitive tissue located at the eye fundus where the images formed by the optical system of the eye are projected. It is composed of ten different layers in which several kinds of cells detect (the photoreceptors) and preprocess (the Müller, horizontal, bipolar, amacrine and ganglion cells) the optical signal (see Figure 1.2). At the retina, light reaches first the inner limiting membrane and crosses several highly transparent before reaching the photoreceptors. There are two kinds of photoreceptors: rods -sensitive to low luminance conditions-, and cones. There are three types of cones, L, M and S, which are sensitive to long (red), medium (green) or short (blue) wavelengths of the visible spectrum, respectively. Cones are responsible for the human color vision, but are only operative in high-luminance conditions.

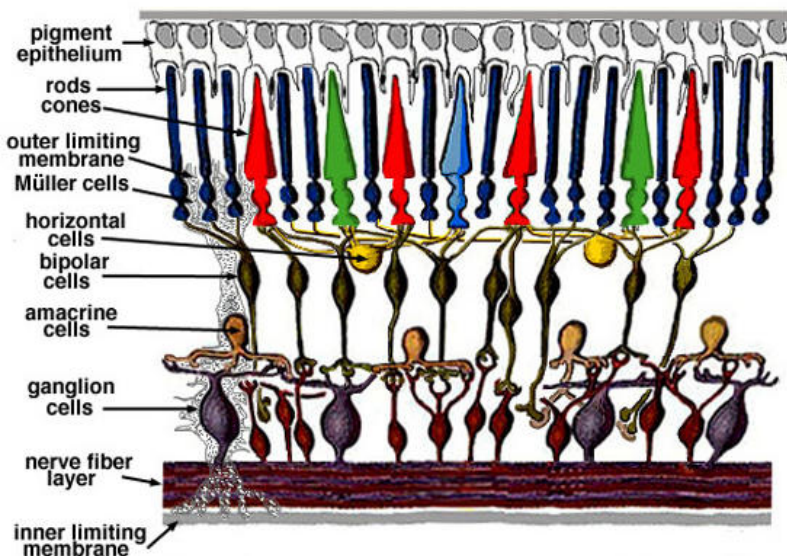


Figure 1.2. The layers of the retina. Source: <http://retina.umh.es>

The fovea is a 1.5 mm in diameter depression on the retina, which center is located at about 5° from the optical axis (see next subsection). Most of receptors are cones in this area. Figure 1.3 shows the distribution of both types of photoreceptors on the retina. In the center of the fovea (a 0.35 mm in diameter region called *foveola*), there are only cones. As the distance to the fovea increases, cones density dramatically decreases. On the other hand, the number of rods is higher on the periphery, also decreasing with the eccentricity but in a much lower rate. In the optical disk, where the optical nerve is situated, no photoreceptors can be found.

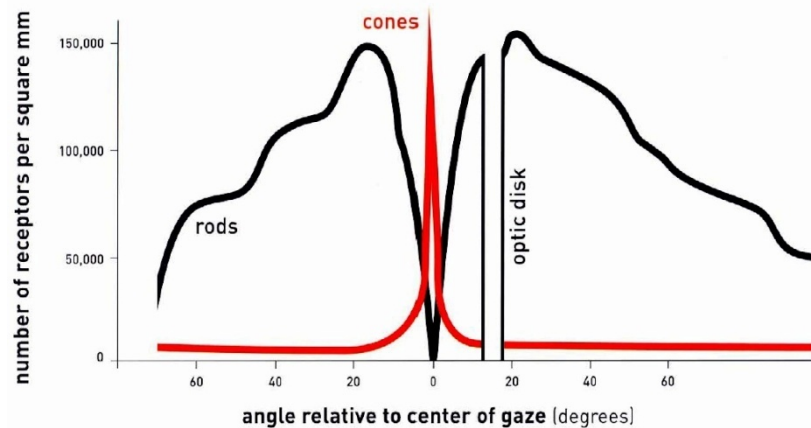


Figure 1.3. Photoreceptor density along the retina

The axial (or eye) length is defined as the distance between the anterior pole of eye and the retina. Numerous studies have shown that the axial length varies greatly across subjects [Hosny et al., 2003; Kubo et al., 2006; Nangia et al., 2010]. In a population study, Nangia et al. reported values ranging from 18.2 to 33.4 mm for the axial length (mean value:  $22.5 \pm 1.16$  mm). This variability is related to the existence of ametropia: myopia and hyperopia. Myopic eyes are usually longer, while hyperopic eyes tend to be shorter [Hosny et al., 2003; Llorente et al., 2004a]. In a group of young subjects, Llorente et al. [2004a] reported a mean eye length of  $25.16 \pm 1.23$  mm for myopes and  $22.62 \pm 0.76$  mm for hyperopes. Therefore, while emmetropic eyes focus the image of an object placed at infinity on the retina when the crystalline lens is unaccommodated, myopic eyes focus the same object in front of the retina, and hyperopic eyes, behind it. Ophthalmic corrections (such as glasses or contact lenses) are needed to properly focus the images on the retina in subjects suffering from myopia or hyperopia. Hyperopes can image far objects on the retina using the ability of the crystalline lens to accommodate, if their amplitude of accommodation is larger than their refractive error. However, as the amplitude of accommodation is limited and decreases dramatically with age (as it will be shown in section 1.5) that may prevent them from focusing near objects.

### 1.2.6. Axis of the eye

The eye is not a centered optical system, as the curvature centers of the ocular surfaces and the fovea do not lie in a single common axis [Thibos et al., 2002a]. For the purpose of this thesis, we are going to define the two following axis:

- Optical axis of the eye: the line joining the centers of curvature of the anterior cornea and the posterior lens surfaces.
- Line of sight: the line joining the fixation point and the centre of the entrance pupil of the eye.

### 1.3. Optical quality of the eye

Since Helmholtz, in the second half of the 19th century, it has been known that the eye is far from being a perfect optical system: optical imperfections, misalignments, ametropia, etc degrade the image projected on the retina, reducing image contrast and limiting spatial frequencies. The major optical errors of the eye, contributing in the greatest proportion to retinal image degradation, are defocus and astigmatism. These low order aberrations are typically corrected, by use of standard sphero-cylindrical corrections. However, other high-order aberrations, not-possibly corrected by standard ophthalmic lenses, further degrade the optical quality, even in eyes accurately corrected for defocus and astigmatism. High order aberrations -first reported by Helmholtz [1885]- vary greatly in magnitude and distribution across the population [Castejón-Mochón et al., 2002; Porter et al., 2001; Thibos et al., 2002b; Hartwig and Atchison, 2012; Plainis and Pallikaris, 2008].

There are two different classes of aberrations: chromatic and monochromatic aberrations. Chromatic aberrations are due to chromatic dispersion (the variation of a lens's refractive index with wavelength), while monochromatic aberrations are measured for a single wavelength. This thesis addresses the interaction between the high order aberrations -and therefore, the optical quality- of the human visual system and its mechanism for focusing images. This section will describe mathematically the monochromatic aberration. The next sections of this chapter will introduce the concepts of optical quality, the accommodation process and the interaction between them.

#### 1.3.1. Wave aberrations

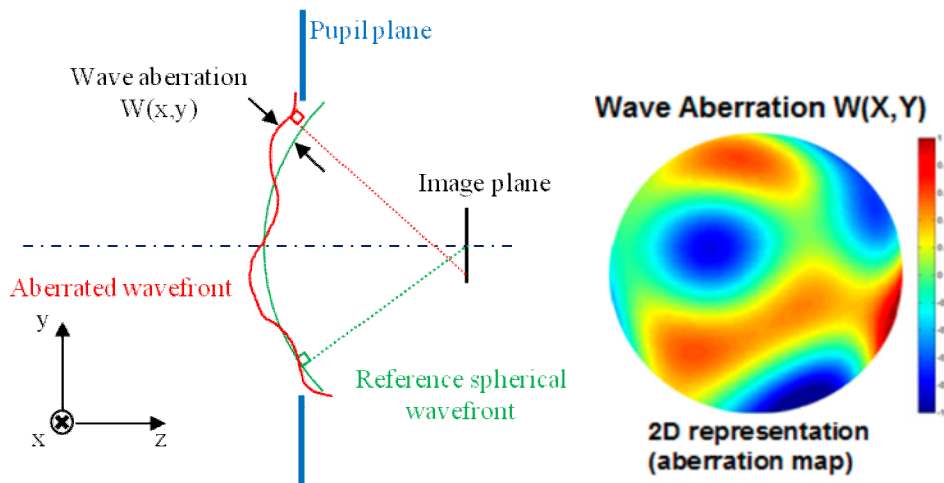


Figure 1.4. The elevation maps represent in a color scale the wave aberration function, that is, the difference between the aberrated wavefront and the reference one.

The optical performance of an optical system is usually described in terms of its wave aberration,  $W(x, y)$ , which defines how the phase of a monochromatic light is affected as it passes through the optical system. In its propagation, the light can be characterized by its wavefront, a line that joins all the points that have the same phase and which is perpendicular to the direction of propagation. Essentially, the wave aberration is the difference between the ideal wavefront (corresponding to a perfect optical system) and the real one. For a single object point, the reference surface would be a sphere (a plane if the point is placed at infinity). Wave aberration function is usually estimated in a

pupil plane, and can be represented graphically with an elevation map (see Figure 1.4). Colors in the map indicate the magnitude of the deviation of the real wavefront from the reference one.

### 1.3.2. Zernike polynomials

The wave aberration is often defined mathematically by a series of polynomials. The most popular polynomials in Visual Optics are Zernike polynomials, first introduced by Frits Zernike [Zernike, 1934]. The reasons for its extended use in the visual optics field are mainly two: (1) Due to the presence of the eye's pupil, the region of interest in the wave aberration function is circular, and Zernike polynomials are orthonormal in a unit circle; (2) The terms of second order have a direct correspondence with the classic optometric magnitudes of defocus and astigmatism.

Therefore, wave aberration  $W(x,y)$  can be represented as a sum of polynomials (Equation 1.2). Each Zernike term is formed by the product of a radial  $n$  function, an angular  $m$  function and a normalization factor, specified by radial indexes. The weights of polynomials are called the Zernike coefficients ( $C_m^n$ , corresponding to the radial order  $n$  and the meridional frequency  $m$ ) and represent the magnitude of each particular ocular aberration present in the wave aberration. The Optical Society of America has established a set of recommendations [Thibos et al., 2002a] about sign, normalization and ordering, which has been followed in this thesis.

$$W(x, y) = \sum_{n,m} c_m^n Z_m^n(x, y) \quad \text{Equation 1.2}$$

where  $W(x, y)$  is the wave aberration expressed in Cartesian coordinates and  $Z_m^n(x, y)$  is the Zernike polynomial expressed in Cartesian coordinates for radial order  $n$  and meridional frequency  $m$ .

Piston and tilt (the zero and first terms, respectively) are not actually true optical aberrations, as they do not affect the curvature of the wavefront; they only shift the wavefront to a different position. For that reason, they are not going to be considered during this thesis.

### 1.3.3. Optical quality metrics

Due to the simplicity of its calculation, one of the most common metrics to evaluate the optical quality of the eye is the Root Mean Square (RMS) wavefront error. The RMS is computed directly from the Zernike coefficients, using the equation 1.3

$$RMS = \sqrt{\sum_{n,m} (c_m^n)^2} \quad \text{Equation 1.3}$$

where  $c_m^n$  is the Zernike coefficient corresponding to the order  $n$  and frequency  $m$ . Furthermore, the Zernike terms are normalized so that the coefficient of a particular term or mode is the RMS contribution of that term.

Alternatively, several retinal image quality metrics can be obtained from the wave aberration function. These metrics consider the effects of diffraction and aberrations on the retinal image by applying numerical Fourier optics to the wave aberration. Figure

1.5 shows in a diagram the relationship between different retinal image quality metrics, including the Point Spread Function (PSF), the Optical Transfer Function (OTF), the Modulation Transfer Function (MTF) and the Strehl Ratio (SR). PSF and MTF are going to be used during this thesis.

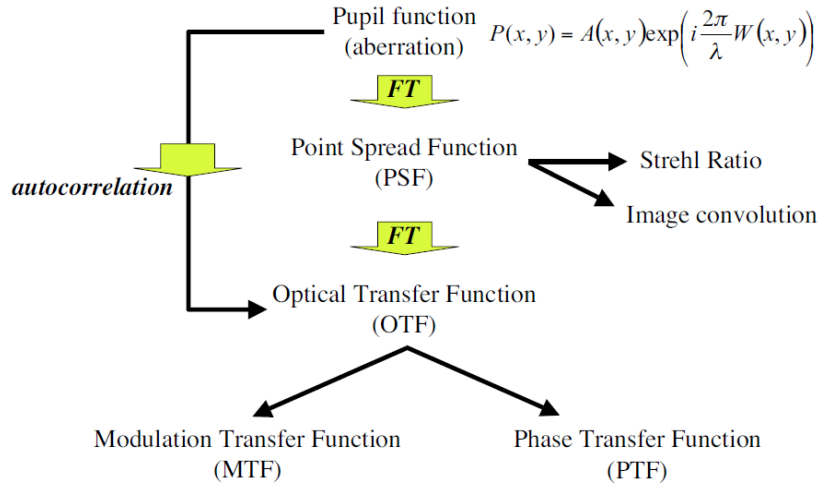


Figure 1.5. Relationship between the different optical quality metrics.  
Source: <http://cfao.ucolick.org>

The **Point Spread Function (PSF)** is the image of a point object through the optical system. Mathematically, the PSF is calculated as the squared magnitude of the inverse Fourier transform of the pupil function,  $P(x, y)$ , which defines how light is transmitted by the eye optics.

$$P(x, y) = A(x, y) e^{i \frac{2\pi}{\lambda} W(x, y)} \quad \text{Equation 1.4}$$

$$PSF(x, y) = K \left| FT[P(x, y)]_{f_x = \frac{x}{z}, f_y = \frac{y}{z}} \right|^2 \quad \text{Equation 1.5}$$

where  $K$  is a constant,  $P(x, y)$  is the pupil function,  $A(x, y)$  is an apodization function (when the waveguide nature of cones is considered) and  $W(x, y)$  is the wave aberration.  $P(x, y)$  is zero outside the pupil. FT is the Fourier Transform operator,  $z$  is the distance from the pupil to the image (eye length).

In a perfect optical system (only limited by diffraction), the PSF corresponds to the Airy disk. In a normal eye, both diffraction and aberrations contribute to spread out the light. The effect of aberrations is predominant for pupils larger than 3 mm in diameter. Figure 1.6 shows the PSF of the same subject for different pupil sizes.

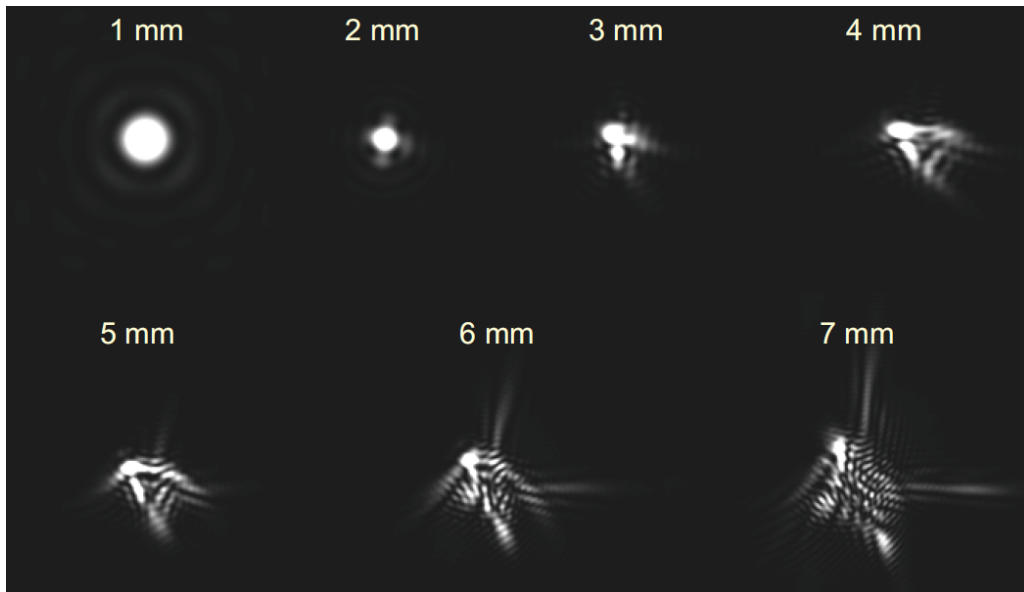


Figure 1.6. PSF of the same subject for different pupil sizes.  
Source: <http://cfao.ucolick.org/>

The **Optical Transfer Function** (OTF) is the autocorrelation of the pupil function, or equivalently, the Fourier Transform of the PSF (see Figure 1.5). The modulus of the OTF is the Modulation Transfer Function (MTF), which indicates the reduction in contrast; and its phase is the Phase Transfer Function (PTF), which is associated with the presence of asymmetrical aberrations.

The **Strehl Ratio** (SR) is a scalar metric used to describe the quality of the PSF in an eye. It was introduced by K. Strehl at the end of 19th century. In the spatial domain, it can be calculated directly from the PSF. It is the maximum value of the PSF in the presence of aberrations, normalized by the maximum of the diffraction limited PSF for the same pupil size. The SR ranges from 0 to 1, with 1 defining a perfect optical system. The Marechal criterion states that a system is regarded as diffraction limited if the SR is 0.8 or greater.

In the frequency domain, the SR is computed as the volume under the OTF of an aberrated system normalized by the diffraction-limited OTF, for the same pupil diameter. As the SR includes in the calculation regions of the OTF with spatial frequencies beyond those relevant to the visual system, new metrics (such as visual Strehl) have been introduced [Iskander, 2006].

In this thesis the **volume under the MTF** truncated at 100 c/deg [Marcos et al., 1999a] will be used. This definition (and the visual Strehl) has been shown to provide the best prediction of subjective refractive error in previous works [Guirao and Williams, 2003; Marcos et al., 2008], and takes into account interactive effects between different Zernike terms as well as diffraction. It also allows comparisons across states with different pupil sizes.

### 1.3.4. Aberrations on the human population

There is a great variability across the population in the amount and distribution of aberrations but, on average, lower terms usually contribute more to the total RMS. On a population study, Porter et al. [2001] reported that defocus and astigmatism (second

order terms) contribute to the 80% and 12.7% of the total RMS, respectively, while the contribution of the 3rd order terms was a 4.3% of the total RMS.

Typically, the population average of nearly all high order terms is zero. Porter et al. reported that spherical aberration was the only mean coefficient significantly different from zero (mean value of  $0.138 \pm 0.13 \mu\text{m}$  for a 5.7 mm pupil). Other studies reported a negative mean significant value for oblique trefoil [Cheng et al., 2004, Thibos et al., 2002b, Wang and Koch, 2003].

Salmon and Van de Pol [2006] collected data from 10 laboratories that measured high order aberrations (HOA) in normal, healthy adult eyes using Shack-Hartmann aberrometry (2560 eyes of 1433 subjects). The most prominent Zernike modes and their mean absolute values (6.0-mm pupil) were  $Z_3^1$  (0.14mm),  $Z_4^0$  (0.13mm) and  $Z_3^3$  (0.11 mm). The mean total higher-order RMS up to 6th order was 0.33 mm.

Finally, some of the population studies show a relative symmetry between aberration pattern of right and left eyes [Porter et al., 2001; Thibos, et al. 2002b], although other works suggested a lower degree of symmetry [Marcos and Burns, 2000; Castejon-Mochon et al., 2002].

### 1.3.5. Techniques to evaluate the optical quality

From Scheiner in 1619 to the new aberrometers, different techniques have been proposed to measure the optical quality of the eye, including the double-pass technique, Laser Ray Tracing (LRT) and Hartmann-Shack wavefront sensing, among others.

#### *Double-pass*

Wave aberration can be obtained from double-pass intensity images of a point source at infinity [Santamaría et al., 1987, Artal et al., 1988]. In the first pass, the PSF of the aberrated eye is projected on the retina. On the second pass (a camera imaging this PSF) the auto-correlation of the PSF of the eye is captured [Artal et al., 1995], from which the MTF can be retrieved, but not the PSF.

Many aberrometers are based on the trajectories of rays through the optical system. Although there are some *subjective* (or psychophysical) aberrometry techniques, we will limit the description to the *objective* techniques: LRT and HS wavefront sensing.

#### *Laser Ray Tracing*

A Laser Ray Tracing aberrometer measures the optical aberrations of the eye by delivering narrow laser beams sequentially through different pupil positions, and simultaneously collecting on a CCD camera the light reflected of the retina corresponding to each entry position [Navarro and Losada, 1997]. The local ray aberration (proportional to the local derivative of the wave aberration) is obtained from the corresponding aerial image as the deviation of the centroid position from the reference (position corresponding to chief ray). The wave aberration for each position is then estimated by integration from ray aberrations.

As LRT-based aberrometers measure the ray aberration on the retina or image space (i.e., they measure the deviation of the rays as they enter the eye), they are called “ingoing aberrometers”. LRT has a high dynamic range that makes it very convenient to measure aberrations in highly aberrated eyes, such as keratoconus [Barbero et al., 2002].

### Hartmann-Shack wavefront sensor

A Hartmann-Shack wavefront sensor (HSWS) consists of a matrix of microlenses (lenslet array) of the same focal length and a CCD camera placed at the focal distance of the lenslet. When a flat wavefront reaches the HS wavefront sensor, each microlens focuses a portion of the incident wavefront at its focal on the CCD camera, creating a regular array of “reference” spots (Figure 1.6). If the incident wavefront is not flat, the local tilt at each subaperture will determine the position of each spot centroid at the focal plane. If the wavefront is locally approximated by a tilted plane, the displacement of each aberrated spot with respect to the reference spot is proportional to the local slope of the wavefront. Therefore, the wavefront aberration can be reconstructed from the first derivatives of the wave aberration by equations 1.5.

$$\left. \frac{\partial W(x,y)}{\partial x} \right|_{x=x_i, y=y_i} = \frac{\Delta x_i}{f} \quad \text{Equation 1.5a}$$

$$\left. \frac{\partial W(x,y)}{\partial y} \right|_{x=x_i, y=y_i} = \frac{\Delta y_i}{f} \quad \text{Equation 1.5b}$$

where  $i$  is the lenslet considered;  $f$ , the focal length of the lenslet,  $\Delta x_i$  and  $\Delta y_i$  are the displacements of the “aberrated” spots in the CCD camera with respect to the reference spot, and  $\left. \frac{\partial W(x,y)}{\partial x} \right|_{x=x_i, y=y_i}$  and  $\left. \frac{\partial W(x,y)}{\partial y} \right|_{x=x_i, y=y_i}$  the average partial derivatives of the wavefront aberration over the  $i$  lenslet area.

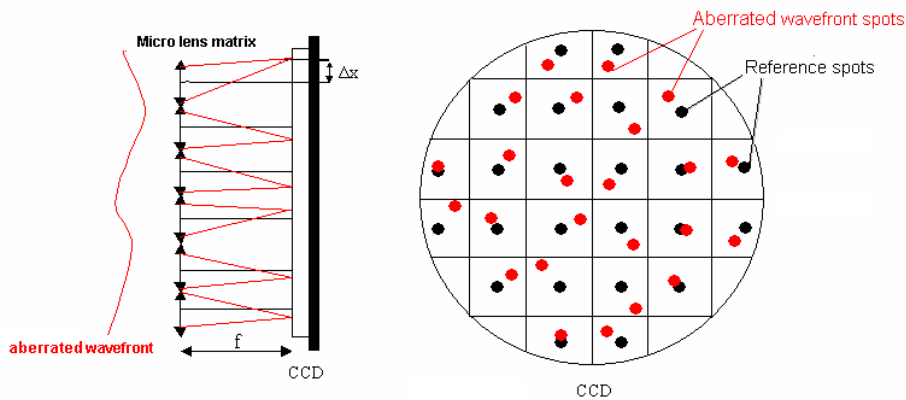


Figure 1.6. The microlenses matrix samples the aberrated wavefront. The wavefront can be estimated from the difference between the spots for this aberrated wavefront and the reference spots of the ideal one

### 1.3.6. Adaptive Optics

Adaptive Optics is a technique initially used to obtain diffraction-limited images of the sky in ground-based telescopes since 1977. Turbulence of the atmosphere creates dynamical changes in the optical path, originating wave aberrations. This technique was later applied to the vision field, especially after Liang et al. [1994] succeeded in the construction of an AO system to overcome the imperfections of the eye optics and visualize better the eye fundus.

There are two main elements in an AO system: a wavefront sensor that captures the wavefront from the object of interest (eye, star...); and a phase modulator that, placed in the optical path between the object and the sensor, modifies the wavefront.

An AO system can work in two different configurations:

(1) Open-loop: In this modality, the state of the phase modulator is fixed: changes in the incoming wavefront will not be compensated by the system. Therefore, a static correction is performed.

(2) Closed-loop: In this configuration, the wavefront is continuously monitored and the state of the phase modulator is changed to achieve the targeted condition. Therefore, a dynamic correction is performed.

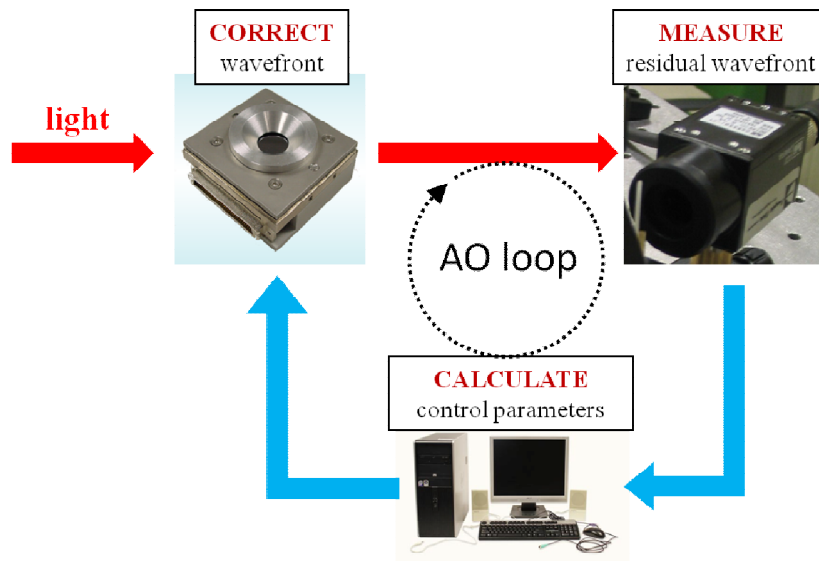


Figure 1.7. Adaptive Optics loop: The wavefront passing through the correction element is measured, the parameters to change it are calculated and sent for its correction. If no further operation is performed, the system is said to be working in open-loop. If the process is continuously performed in order to correct any temporal variation of the incoming wavefront, the system is said to be working in closed-loop.

### 1.3.6.1. Wavefront sensor

An Adaptive Optics system is necessarily composed of two elements: a wavefront sensor and a phase modulator. In section 1.3.5, different techniques that allow measuring the aberrations of the eye have been described. However, not all of them are appropriate for an AO system, which requires the fulfillment of some conditions such as accuracy, high speed, high dynamic range, sensitivity to details, safe intensity levels, and comfortability. Some of them, such as Double Pass systems and LRT, are not suited or sufficiently fast for its integration in an AO system. On the other hand, Hartmann-Shack wavefront sensors appear to be ideal for its use in AO systems.

The most important characteristics that a corrector element has to fulfill on an AO system are the following:

- *Dynamic range*: which amount of aberrations can it correct/induce?
- *Speed*: how long does it take to reach the requested state?
- *Accuracy*: how close to the requested state is it able to reproduce?

### 1.3.6.2. Phase modulator

Depending on the mechanism used to modify the wavefront, there are two main types of phase modulators: liquid-crystal modulators and deformable mirrors.

#### 1.3.6.2.1 Liquid-crystal phase modulators

In these devices there is no movable macroscopic element: the optical path is modified by local changes in the refractive index. The liquid-crystal molecules are birefringent and polar, tending to be aligned in the same direction so that the macroscopic behavior is a uniaxial anisotropic material. By applying an external electric field, the mean angle of the molecules -and therefore, the effective refractive index for a linearly polarized beam- can be controlled.

#### 1.3.6.2.2 Deformable mirrors

Phase modulation is always performed by changing the optical path of the rays that cross a plane, altering the wavefront. In a deformable mirror, this is achieved by locally moving the reflective surface. Depending on how is the surface, the mirrors can be continuous or segmented (Figure 1.8).

Segmented mirrors are composed of a set of prisms with an anterior specular surface where the wavefront is reflected (see Figure 1.8a). These mirrors can be moved in the piston direction (Figure 1.8b) and/or tip/tilt (Figure 1.8c) to modify the optical path of the wave. However, the discontinued reflecting surface produces diffraction losses.

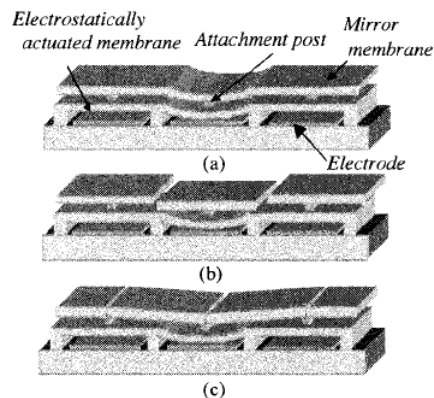


Figure 1.8. Lateral views of a deformable mirror: (a) continuous, (b) segmented with piston displacement, and (c) segmented with tip-tilt movement

Continuous mirrors consist of a continuous reflective membrane and a set of actuators behind. To determine the voltages that must be applied to every actuator to produce the desired shape of the membrane, the following control procedure is performed:

1. The response of the membrane to a voltage applied to every individual actuator (the *influence function* of the actuator) is measured.
2. From the influence functions, the *influence matrix* is obtained. This matrix indicates which surface would correspond to a certain set of voltages, assuming the existence of linearity.
3. The *control matrix*, defined as the inverse of the influence matrix, is calculated.

- An iterative process is used to determine the values of the voltages for each actuator, measuring the wavefront until the desired state is reached.

It is important to remark that not any surface can be accurately reproduced by the mirror. The interaction matrix defines the set of spatial modes (see Figure 1.9) of the membrane that can be obtained: any surface that could be expressed as a linear combination of these modes could be exactly reproduced by the mirror. Otherwise, there is always a residual error.

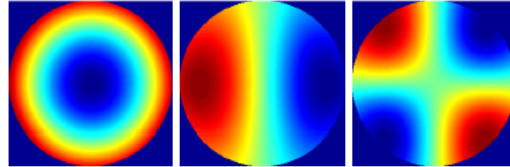


Figure. 1.9. Some low order modes that can be generated by an electrostatic mirror. From left to right: Defocus, horizontal tilt and astigmatism at  $0^\circ$

Continuous mirrors can be sub-classified according to the principle in which are based to deform of the membrane:

- Electrostatic mirrors.** The deformation of the surface is obtained by applying different voltages to the set electrodes placed under the membrane, which has a constant voltage (usually connected to ground).
- Piezoelectric mirrors.** In this mirrors a set of piezoelectric ceramic actuators are attached to the membrane. These piezo-actuators change their length depending on the applied voltage, modifying the surface of the mirror.
- Magnetic mirrors.** To manipulate the deformable membrane, a set of magnets is attached to it. Every magnet has a corresponding coil under the surface. By applying a voltage to the coil, a magnetic field is created that pushes or pulls the magnet (see Figure 1.10).

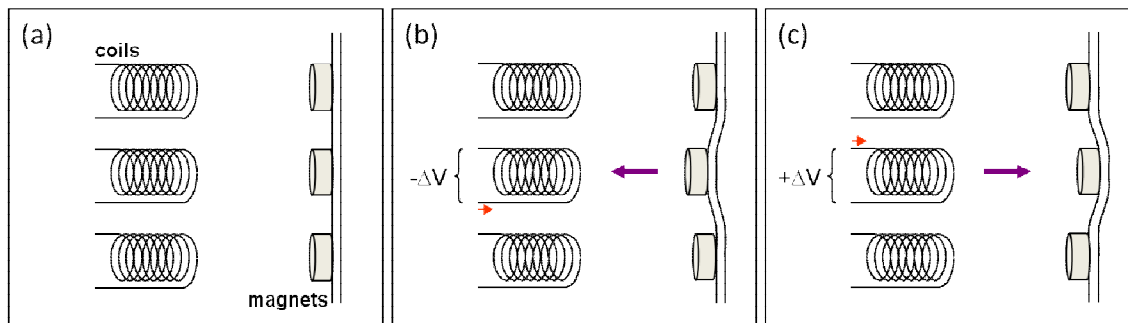


Figure 1.10. Magnetic deformable mirror. Applying a voltage in the coils creates a magnetic field that, depending on the sign, pulls (b) or pushes (c) the magnets attached to the mirror surface.

Deformable mirrors have become the most popular phase modulators for visual applications, mainly due to the low light losses (which can be important on vision due to light limitations for safety reasons) and the achromaticity. In particular, magnetic deformable mirrors have been widely used in vision because of their high stroke ( $50 \mu\text{m}$ ), linearity and fidelity correcting and generating aberrations [Fernández et al, 2006].

In this thesis an AO system was developed for testing the influence of high order aberration on the accommodation accuracy, using a Hartmann-Shack wavefront sensor and a magnetic deformable mirror. The system is described in Chapter 2.

## 1.4. Accommodation

The focusing system of the human eye is based on the ability of the crystalline lens to change its shape and, therefore, its contribution to the optical power of the eye. This process is called accommodation. Although the term accommodation is sometimes used to describe the focusing process, it refers to the far-to-near focusing process, while the near-to-far change of focus is called disaccommodation.

This thesis addresses the study of the accommodation mechanism the interaction of the optical quality of the eye with the accommodation accuracy. And imaging the crystalline lens during accommodation using Optical Coherence Tomography.

### 1.4.1. The accommodation mechanism

Anatomically, the crystalline lens is embedded in the lens capsule, an elastic membrane attached to the ciliary muscle by the zonules (see Figure 1.11). According to the accommodation theory of Helmholtz, a contraction of the ciliary muscle within the ciliary body releases the tension of the zonules (see Figure 1.11, right). Due to the crystalline lens elasticity, its equatorial diameter decreases, its thickness increases, and the radius of curvature of its two surfaces increases. The result is an increase on the optical power, what allows focusing the near objects.

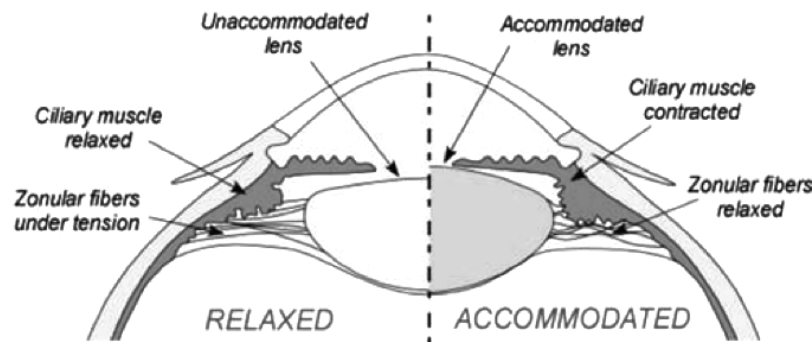


Figure 1.11. Accommodation process: When looking at infinity, the ciliary muscle is relaxed and the zonular fibers under tension (left). To focus near targets, the ciliary muscle contracts and the zonules relax, allowing the lens to become steeper and increase its optical power (right).

Schachar et al., [1993] proposed an alternative theory of the accommodation mechanism, based on Thscherning's theory [Tscherning, 1904]. Schachar considered that the contraction of the ciliary muscle contraction would produce a relaxation of the anterior and posterior zonular fibers, but an increased tension in the equatorial ones [Schachar, 1994]. This would increase the lens diameter with accommodation, flattening the lens in the periphery but, according to his theory, making the central part more convex (increasing lens power). However, it has been shown experimentally that the equatorial lens diameter decreases with accommodation [Glasser et al., 2006].

### 1.4.2. The accommodative response. Optometers

Figure 1.12 shows the typical accommodative response (or accommodative effort) of an emmetropes as a function of the accommodative demand (or vergence) using Hartmann-Shack aberrometry. Ideally, the response should be a 1:1 correspondence with the stimulus (dashed line). Instead, it is well-known that the eye tends to over-accommodate when viewing at infinity, and under-accommodates for near targets. In the first case, the

difference between the real and the ideal responses is called the accommodative lead, while the second receives the name of accommodative lag (and would correspond to the residual refractive error). If defined as the real response minus the ideal one, the lead is a positive magnitude while the lag is expected to be negative.

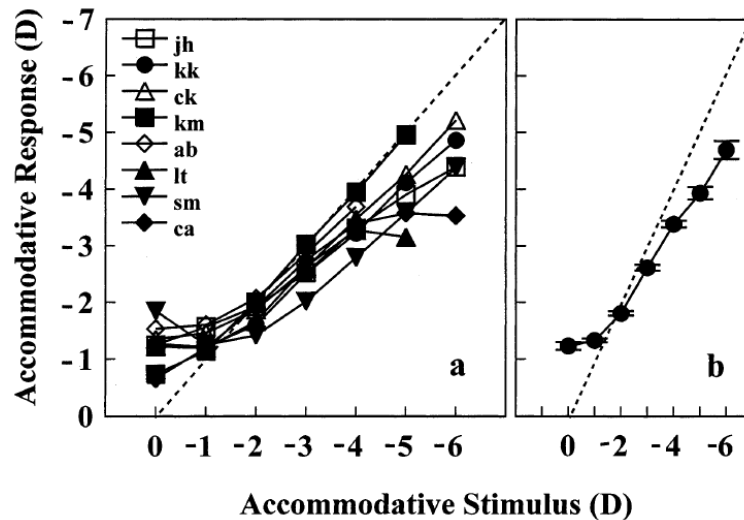


Figure 1.12. (a) Accommodative response of a group of eight young subjects and (b) the mean response of these subjects, which represents the typical dependence between the accommodative response and stimulus. Data from He et al. [2002].

The refractive power of the eye can be measured with an instrument called “optometer”. Optometers can be subjective and objective. Subjective optometers rely on the verbal feedback from the patient, regarding the clarity of distant targets, while objective techniques provide the measurement independently of the subject’s experience. Subjective techniques for assessing the accommodation techniques, such as push-up (manually approach of the target) or the use of negative lenses (to change vergence), are widely used in the clinic: they are simple and require no alignment, but tend to overestimate the accommodative response.

Objective optometers usually operate using an infrared signal to avoid interaction with the visual stimulus. They can be based on different principles, the most relevant of which are the principle of Scheiner, the eccentric photorefraction, the analysis of the retinal image and the analysis of the wavefront.

#### 1.4.2.1. Scheiner optometers

In 1619, Scheiner discovered that the refractive state of the eye could be precisely determined by placing a double pinhole aperture in front of the eye (see Figure 1.13). Heron, et al. [1989] replaced the double pinhole by a biprism to produce two bundles of light from the infrared irradiated object. When the eye is focused at infinity a single image of the slits is formed on the retina. If the eye accommodates, the single slit image on the retina is split in two separate slits. Optometers based on the Scheiner principle have a resolution of around 0.05 D, and allows dynamic measurements. However, these optometers require precise alignment to the patient’s pupil to be maintained throughout the measurement.

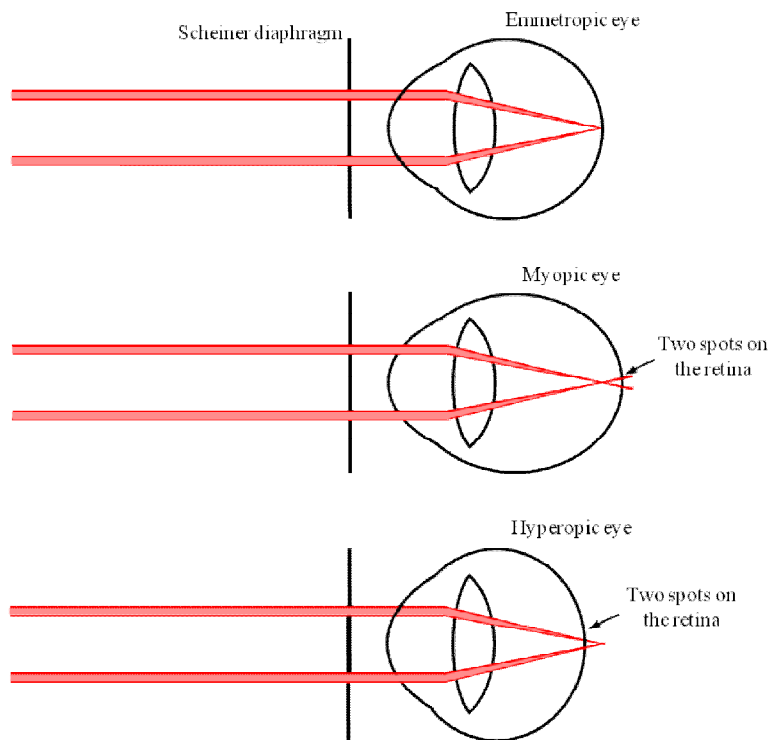


Figure 1.13. When introducing the Scheiner filter, the image of a far point produces a single point on the retina for the emmetropic eye, but two points for the myopic or hyperopic eye.

#### 1.4.2.2. Eccentric photorefracton (photoretinoscopy)

In eccentric photorefracton, the refractive state of the eye is determined based on the appearance of the light distribution -or reflex- that appears in the pupil from a double passage of light through the optical system [Howland, 1985; Schaeffel et al., 1987]. Figure 1.14 shows an optometer designed by Roorda et al. [1998] using this principle. The light arises from an infrared LED placed at one side of the camera aperture (in a retinal plane), therefore eccentric to the optical axis of the system. A CCD camera conjugated to the pupil plane allows the registration of the light distribution on the pupil, called the *pupil reflex*, after reflecting in the retina.

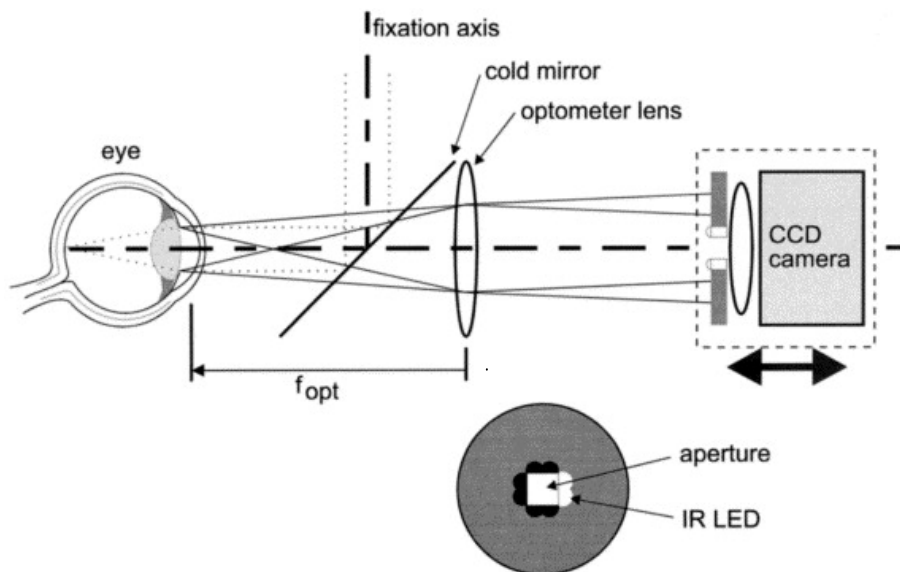


Figure 1.14. Eccentric photo-optometer design by Roorda et al, [1998]

The refractive measurement is done by analyzing the image in the pupil plane received by the CCD camera. If the subject is emmetrope, the reflex has a uniform intensity, but in the presence of any refractive error, the intensity distribution shows a slope. The direction of the slope indicates the sign of the refractive error: a higher intensity on the side of the infrared source indicates a *myopic* error, while the opposite occurs for a *hyperopic* error (Figure 1.15). The slope of the intensity gradient increases with the refractive error, allowing its quantification [Roorda et al., 1998].

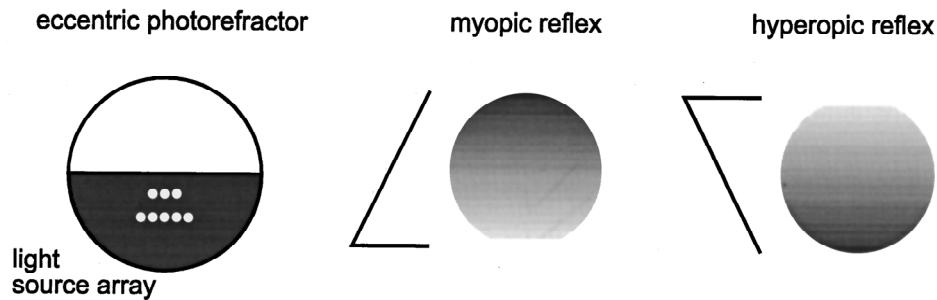


Figure 1.15. Typical illumination pattern of an eccentric photorefractor (a) -such as the PowerRefractor, or the design by Schaeffel et al. and intensity distribution or reflex that appears in the pupil for a myopic subject (b) and a hyperopic subject. The line to the left of each pupil shows the intensity profile across the vertical meridian of the pupil. The reflex fills the pupil, and the slope of the intensity profile is used to deduce the refractive state. From Roorda et al. [1998]

A commercial system based on this technique, the Power Refractor (Plusoptix), has been used in this thesis to test the accommodative range of the subjects.

#### 1.4.2.3. Autorefractors

Autorefractors project an image on the retina and estimates refraction by analyzing this image with a CCD camera. For example, the Shin-Nippon SRW500 autorefractor is based on the projection of an annular light source [Mallen et al., 2001]. Figure 1.16 shows how the presence different refractive errors have differential impact on the shape of the projected ring.

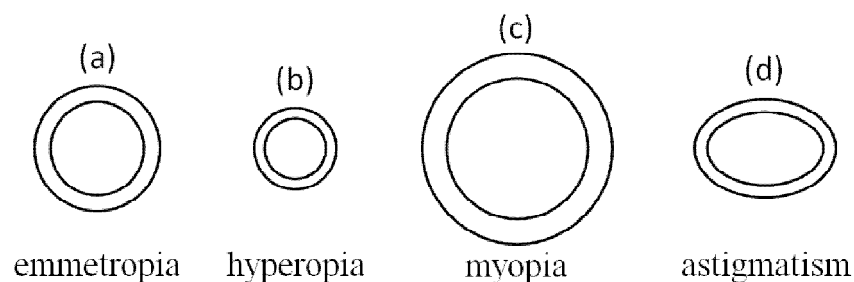


Figure 1.16. (a) Retinal image of the ring projected by the Shin-Nippon autorefractor in an emmetropic eye. The pattern changes when the subject has myopia (b), hyperopia (c) and/or astigmatism (d), what can be used to assess the refractive error.

#### 1.4.2.4. Aberrometry and refractive error

Wave aberrations measured by aberrometers are usually expressed in terms of its Zernike expansion, which second order aberrations are defocus and astigmatism. Thus, refraction could directly be obtained from these Zernike coefficients of the second-order. However, several studies have shown that eliminating the second-order Zernike

aberrations does not necessarily optimize the objective measurement of visual performance [Thibos et al., 2002a; Applegate et al., 2003a]. Thus, alternative metrics of optical quality that are optimized by subjective refraction when higher-order aberrations are present have been proposed [Cheng et al., 2003; Girao et al., 2003; Chen et al., 2005].

Thibos et al. [2004] analyzed the accuracy and precision of 33 methods to determine objective refraction from wavefront aberrations. They found paraxial curvature matching of the wavefront aberration map to be the most accurate method for determining the spherical equivalent error. Paraxial curvature matching can be easily computed from the Zernike coefficients terms of frequency  $m=0$ . Equation 1.6 shows how to obtain the refractive error from the Zernike coefficients up to the sixth Zernike order but could be extended to higher orders if warranted [Atchison et al. 2004].

$$M = -\frac{4\sqrt{3}c_2^0 - 12\sqrt{5}c_4^0 + 24\sqrt{7}c_6^0 - \dots}{R^2} \quad \text{Equation 1.6}$$

### 1.4.3. Changes of the human lens with accommodation

Lens geometry changes with accommodation. The study of the changes in lens geometry, such as the lens position, thickness and radii of curvature, is essential to understand the mechanism of accommodation and the age-related changes leading to presbyopia.

Biometric changes with accommodation are frequently presented per diopter of accommodative response. If the accommodative response has not been measured/estimated, biometric changes can be reported per diopter of accommodative demand. However, the reliability of the values obtained for a biometric parameter per accommodative demand is compromised by the uncertainty on the actual accommodative response of the subject, as it may lead to underestimations in case of poor accommodation performance. Furthermore, comparisons of the biometric changes per accommodation reported by different studies have to consider this discussion. From a quantitative point of view, the dependence of any biometric magnitude with the accommodative response is preferable. During this thesis manuscript, unless otherwise noted, changes of magnitudes with accommodation are assumed to be referred to the accommodative response.

#### 1.4.3.1. Radii of curvature

There are several studies in the literature reporting the change of human crystalline lens radii of curvature *in vivo* as a function of accommodative response or demand, using different techniques. Table 1.1 shows the results reported by Garner and Yap [1997], using Purkinje imaging; Dubbelman et al. [2005], using 2-D Scheimpflug photography; and Rosales et al. [2006], using both Scheimpflug and Purkinje. The absolute values of the radii of curvature of both surfaces decrease with the accommodative demand, as the lens gets steeper.

		Dubbelman 2005	Rosales 2006		Garner & Yap 1997
Method		Scheimpflug	Scheimpflug	Purkinje	Purkinje
Subjects		65	11		11
Age (yr)	range	16-51	22-36		
	mean $\pm$ s.d.	32 $\pm$ 9	28.5		21.2 $\pm$ 2.6
Accommodative demand range (D)		0-8	0-8		0-8
Anterior radius (mm/D)		-0.61	-0.64	-0.57	-0.62
Posterior radius (mm/D)		0.13	0.23	0.29	0.17

*Table 1.1. Review of the changes of lens radii of curvature with accommodation in the literature. Both radii of curvature decrease in absolute value: the initially positive anterior radius decreases, while the negative posterior radius increases. The crystalline lens gets steeper with accommodation*

#### 1.4.3.2. Axial magnitudes

A steepening of the lens with accommodation is expected to result in increased lens thickness. Several studies have explored the axial changes in the anterior segment with accommodation. Anterior movement of the anterior crystalline lens surface, resulting in a decrease of the anterior chamber depth (ACD), and an increase in LT have been shown [Zadnik et al., 1992; Beers and Van der Heijde, 1994a; Garner & Yap, 1997; Dubbelman et al., 2005; Ostrin et al., 2006; Bolz et al., 2007].

Using Scheimpflug imaging, Dubbelman et al. [2005] studied the age-related changes in ACD and LT of the accommodating crystalline lens. They reported the following age-related expression for an accommodative range of 8D:

$$\Delta ACD (mm)/D = -4.8(0.33) \times 10^{-2} + 4.0 (\pm 1.2) \times 10^{-4} * Age$$

$$\Delta Lens (mm)/D = 5.8 (\pm 0.7) \times 10^{-2} - 4.8 (\pm 2.5) \times 10^{-4} * Age$$

Using MRI, Kasthurirangan et al. [2011] reported changes of  $-0.062$  mm/D (ACD) and  $0.066$  mm/D (LT), in 15 subjects, with an accommodative demand of 5 D. Using ultrasound biometry Ostrin et al. [2006] reported changes of  $-0.057$  mm/D (ACD) and  $0.067$  mm/D (LT) in 22 subjects.

Once the changes of ACD and LT with accommodation are measured, the movement of the posterior surface of the lens can immediately be assessed. Most of studies have reported that anterior segment depth increases with accommodation [Bolz et al., 2007; Drexler et al., 1997; Dubbelman et al., 2005; Ostrin et al., 2006]. Koepl et al. [2005] did not find this with partial coherence interferometry although two other studies using the same technique did find an increase [Bolz et al., 2007; Drexler et al., 1997]. The increase in anterior segment depth reported in these studies, for  $\sim 5$  D accommodation, ranged from 0.04 to 0.09 mm. For example, Ostrin et al., [2006] reported an increase in anterior segment length of  $0.017 \pm 0.005$  mm/D.

In this thesis, and for the first time, systematic measurements as a function of accommodation of phakometry and axial distances will be presented using an OCT system (see Chapter 5).

### 1.4.3.3. Equivalent refractive index

The equivalent refractive index is the refractive index that a homogeneous lens with the same shape and of the GRIN lens should have in order to produce the same optical power.

The equivalent refractive index has been studied *in vivo* combining keratometry, phakometry, refraction and axial length measurements. However, the change of refractive index distribution with accommodation is still unclear. Garner and Smith [1997] found a constant equivalent refractive index with accommodation, while Dubbelman's studies using Scheimpflug imaging [Dubbelman et al., 2005] reported a significant increase in the equivalent refractive index with accommodation. However, Hermans et al. [2008] incorporated the accommodative lag to the calculations and reported an almost constant equivalent refractive index consistent with that of Garner. Hermans et al. [2008] also studied the shape of the nucleus of the lens and concluded that the GRIN could be approximated with a two-compartment model with a homogeneous refractive index in the nucleus and in the cortex, which would not change significantly with accommodation. Recent studies in cynomolgus monkeys by de Castro et al. [2013], reported that a lens with a reconstructed GRIN has more negative spherical aberration and a larger shift toward more negative values with accommodation compared with the same lens with a homogeneous equivalent refractive index.

### 1.4.4. Pupil size and accommodation

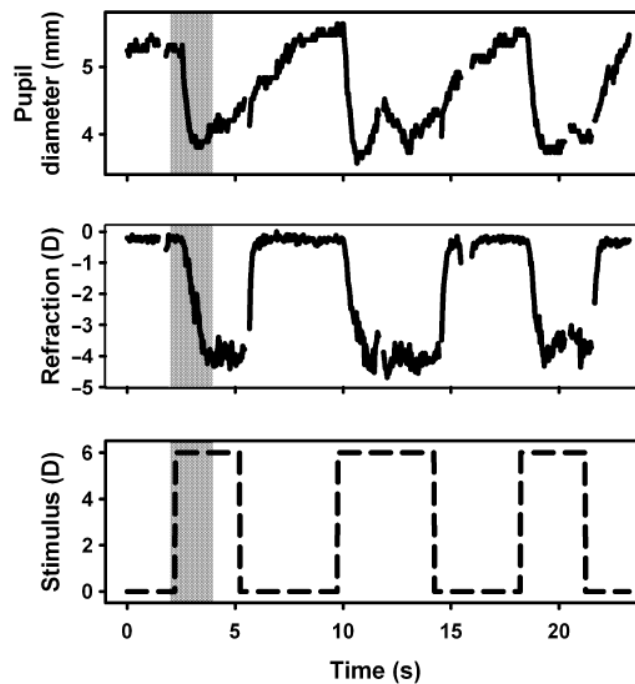


Figure 1.17. Temporal evolution of the pupil diameter and refraction as a response to the accommodative stimulus. The change of pupil size is more drastic in accommodation than in disaccommodation.

Pupil size has been widely shown to be correlated with accommodation. Marg and Morgan [1949] measured the amount of pupil change per diopter of accommodation in a group of young subjects, which ranged from 0.12 to 0.53 mm/D, with a mean value of 0.30 mm/D. For a similar age group, Schaeffel et al. [1993] found pupil response to range from approximately 0 to 0.50 mm/D. Finally, Kasthurirangan and Glasser [2005] obtained a range from 0.20 to 0.76 mm/D, with a mean value of 0.39 mm/D. They also determined the amount of pupil change with disaccommodation, obtaining a mean value of 0.17 mm/D, significantly lower than the accommodation slope. Figure 1.17, obtained from that work, shows the difference in the pupil behavior between accommodation and disaccommodation.

Charman and Radhakrishnan [2009] studied the change of pupil size with accommodation in two groups of 20 myopes and emmetropes, reporting rates of  $0.313 \pm 0.298$  mm/D and  $0.215 \pm 0.148$  mm/D, respectively. This difference was not significant, and can be due to subject inter-variability.

#### **1.4.5. Fluctuations of accommodation**

The accommodative response when focusing on a stationary target is not constant throughout time but fluctuates [Charman and Heron, 1988]. Fluctuations of accommodation have been suggested to be an active method to maintain accommodation response and to play a role in obtaining directional cues for the dynamic accommodative response [Kotulak and Schor, 1986a, Gray et al., 1993a]. However, other authors have suggested that fluctuations of accommodation could be a passive consequence of the reduction in zonular tension with increasing accommodative response, which would allow increased freedom of movement of the crystalline lens [Miege and Denieul, 1988].

The magnitude of the fluctuations of accommodation has been shown to depend also on different factors affecting the depth of focus, such as pupil size [Stark and Atchison, 1997] or luminance [Gray et al., 1993b]. The fluctuations of accommodation to steady target have been reported to be higher in myopes than emmetropes [Harb et al., 2006]. They have also been reported to increase with accommodative response [Kotulak and Schor, 1986b], although some studies have found a maximum for intermediate values of accommodation response [Miege and Denieul, 1988; Plainis et al., 2005]. As aberrations affect depth of focus it is likely that they also play a role in the fluctuations of accommodation, what is going to be study in this thesis.

Finally, several studies have explored the power spectrum of the microfluctuations of accommodation [Winn et al., 1990; Winn and Gilmartin, 1992; Collins et al., 1995a]. In the spectra two different regions has been identified: the low frequency range, between 0–0.6 Hz, primarily associated to the fluctuations of the accommodation plant, and the high frequency range, between 0.9 and 2.5 Hz. The high-frequency component of the microfluctuations in accommodation has been attributed to the heartbeat. Collins et al. [1995a] even found a correlation between components of the microfluctuations in accommodation and harmonics of the pulse rate. They have also been related to mechanical and elastic characteristics of the lens and its support system [Charman and Heron 1988].

### **1.4.6. Accommodative cues**

The mechanism that drives accommodation and the factors that determine the accommodative response are not completely understood. Several cues and factors related to the optical quality of the image projected on the retina have been implicated in accommodative control: blur, aberrations and fluctuations of accommodation. Other factors, including stimulus size, Stiles-Crawford effect, convergence, volition, and cognition [Fincham, 1951; Alper, 1958; Campbell and Westheimer, 1959; Provine and Enoch, 1975; Malmstrom et al., 1980; Kruger, 1980], either play a secondary role or are beyond the scope of this thesis.

#### **1.4.6.1. Blur**

Improper focus of the eye (defocus blur) is considered to be the primary stimulus for accommodation [Campbell and Westheimer, 1960; Tucker and Charman, 1979; Kruger and Pola, 1986; Schor et al., 1992], although blurring of the retinal image results also from other factors including, diffraction and the various aberrations of the eye [Fry, 1955]. However, the even-error nature of defocus blur, which leads to identical blurred images being formed on either side of the point of focus of an optical system that is free of aberrations, opens the debate on the role that blur plays as a stimulus. If the eye were such a system, the same degree of blur would result from either over- or under-accommodation, and the system would have to respond in a trial-and-error manner to reduce blur. The debate is complicated by the fact that the eye suffers from aberrations and sensory peculiarities (Stiles-Crawford effect) which may be useful in converting the even-error nature of blur to an odd-error signal incorporating directional information [Fincham, 1951].

#### **1.4.6.2. Chromatic aberration**

Several studies have shown that the longitudinal chromatic aberration plays a role in reflex accommodation [Aggarwala et al., 1995a; Aggarwala et al., 1995b; Kotulak et al., 1995; Kruger et al., 1993, 1995, 1997; Kruger and Pola, 1986; Lee et al., 1999; Stark et al., 2002] although other studies have provided evidences of the contrary [Charman and Tucker, 1978; Kotulak et al., 1995]. Lee et al. [1999] showed that chromatic aberration drives accommodation to both moving and stationary objects, viewed through a 0.75 mm pin-hole and simulated defocus of +1 D or -1 D. Kruger et al. [1997] showed that some individuals are able to accommodate in the absence of chromatic aberration, which suggested the existence of other achromatic cues driving reflex accommodation.

#### **1.4.6.3. High order aberrations**

Monochromatic high order aberrations have also been identified as possible odd-error cues for accommodation [Charman and Tucker, 1977; Walsh and Charman, 1989]. Wilson et al. [2002] showed with natural pupils that the presence of high order aberrations will result in different point spread functions in combination with either hyperopic or negative defocus (see Figure 1.18). They suggested that these differences might be used by the visual system to identify the correct direction of focus shift.

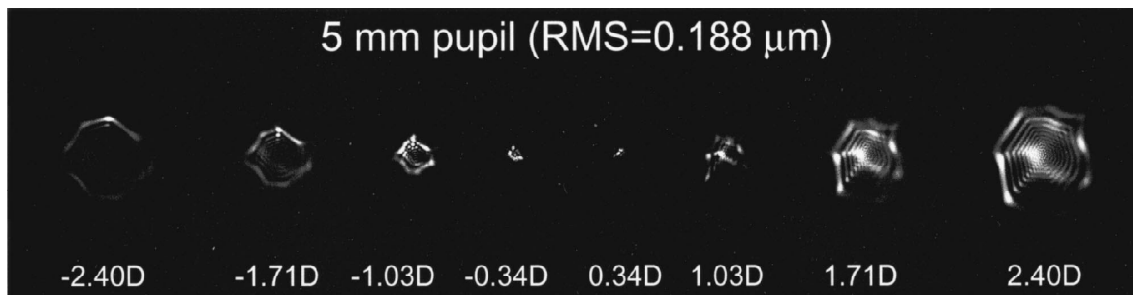


Figure 1.18. Simulated PSFs for a particular subject, based on his monochromatic aberrations, for a 5-mm pupil. The amount of defocus mathematically induced is listed below each PSF. The side of defocus can clearly be appreciated. Extracted from Wilson et al. [2002]

Several studies have further explored the possible impact of aberrations on determining the direction of accommodation, altering the aberration pattern either using adaptive optics – a deformable mirror to correct totally or partially the subject’s aberrations – or lenses. Chen et al. [2006] measured the accommodative response to a 0.5-D step change in vergence on six subjects. One subject clearly required higher order aberrations to accommodate, while four did not. None of the subjects improved their accommodation to a small change of focus when high order aberrations were removed. Fernandez and Artal [2005] measured the accommodative response to a change of 1.5 D or 2 D in two subjects with their normal aberrations and with the asymmetric Zernike terms corrected. They found a significant and systematic increase in the accommodation response time, and a reduction in the peak velocity in both subjects when the aberrations were corrected in real time. However, neither the latency time nor the precision of the accommodation were affected.

More recently, Stark et al. [2009] simulated targets using the subject’s own monochromatic high order aberrations and Stiles–Crawford apodization functions in combination with positive or negative defocus to assess their potential cue on accommodation. They found that monochromatic aberrations provided a statistically significant but rather small cue to monocular accommodation.

#### 1.4.6.4. Fluctuations of accommodation

Charman and Heron [1988] suggested that fluctuations of accommodation could play an active role on controlling accommodation not only maintaining accommodative response, but also obtaining directional cues for the dynamic accommodative response [Kotulak and Schor, 1986a, Gray et al., 1993a]. Gray et al.[1993a] found that lower frequency fluctuations (i.e. under 0.5 Hz) increase when pupil size decreases, showing a correlation between fluctuations and depth-of-focus that may indicate they play a role in the control process which maintains the steady-state accommodation. However, it has been shown previously that when all cues other than blur are removed the initial accommodation response to large step stimuli (>2D) is random [Stark et al., 1965; Smithline, 1974] suggesting that the microfluctuations play no role in guiding the initial direction of the accommodation response at least for large step stimuli.

#### 1.4.7. Change of high order aberrations with accommodation

Aberrometers have been extensively used to measure the wave aberration of the eye, and in recent years they have been used to assess the optical quality of the eye as a function of accommodation either statically [He et al., 2000; Wilson et al., 2002] or dynamically [Hampson et al., 2006; Hofer et al., 2001; Plainis et al., 2005]. Several

authors have measured the change of low and high order aberrations of the accommodated eye [Atchison et al., 1995; He et al., 2000; Lu et al., 1993; Cheng et al., 2004].

It is widely accepted that the only systematic change across subjects occurs for spherical aberration, which shifts toward more negative values with accommodation, and that these changes must be primarily related to changes in shape and structure of the crystalline lens as the eye accommodates [Kotulak and Schor, 1986b, Mieke and Denieul, 1988, Rosales et al., 2008, Birkenfeld et al., 2012]. Cheng et al. [2004], for an artificial pupil of 5-mm, reported a decrease of spherical aberration with accommodation of  $-0.043 \mu\text{m/D}$ , similar to the  $-0.048 \mu\text{m/D}$  of Plainis et al. [2005] for natural pupils, while He et al. [2000] obtained a higher value of around  $-0.083 \mu\text{m/D}$ , for an effective 6.5-mm pupil.

#### **1.4.8. High order aberrations and accommodative lag**

In section 1.4.6, we have seen that monochromatic aberrations (and also longitudinal chromatic aberration) may play a role in determining the direction for accommodation. But, on the other hand, it can be expected that the presence of high order aberrations result in a reduction of the accuracy of accommodation (i.e. larger accommodative lag), as aberrations increase the depth of focus [Marcos et al., 1999b] and changing focus beyond a certain amount will not significantly increase image sharpness. However, to our knowledge no work has systematically explored how the presence of high order aberrations affects the accommodative response.

Several studies have demonstrated that specific combinations of either negative spherical aberration and negative defocus (hyperopic defocus) or positive spherical aberration and positive defocus (myopic defocus) produce sharper images than the same amounts of either defocus or spherical aberration alone [Applegate et al, 2003a, Cheng et al 2004, Chen et al 2005]. On accommodation, this suggests that images will appear less blurred with negative defocus (a lag of accommodation) due to the shift in spherical aberration from positive to negative values with accommodation.

To our knowledge, very few studies have attempted to evaluate the influence of induced spherical aberration on accommodation. Collins et al., [1997] added between  $-3 \text{ D}$  and  $+3 \text{ D}$  of spherical aberration through the use of aspheric surface rigid contact lenses. They found that negative spherical aberration caused an increase of the accommodative response and positive spherical aberration a decrease of it. On the other hand, J. Tarrant [2010] reported in her PhD dissertation that the accommodative response increased when wearing contact lenses adding more positive spherical aberration, while the response decrease with contact lenses adding negative spherical aberration. However, the results were not published in a peer review journal.

Another study looked at the influence of coma and trefoil, induced by contact lenses on the accommodative gain [López-Gil et al., 2007]. They studied the accommodative response in subjects wearing contact lenses that induced low and high values of third order aberrations and found a decrease in gain when around  $1 \mu\text{m}$  (for a 5 mm pupil) of coma or trefoil was induced, which approached but not reached statistical significance, suggesting that 3rd order aberrations may not play a major role in the dynamics of the accommodation response. Several studies have also studied the dynamic accommodative response in the presence of astigmatism [Stark et al., 2003], although the conclusions differ across studies.

## 1.5. The aging crystalline lens: presbyopia and cataracts

### 1.5.1. Crystalline lens changes with age

The human crystalline lens continues to create new cells and grow throughout life, what affects its thickness, the radii of curvature of its surfaces, its refractive index and the value of the spherical aberration, among others.

#### 1.5.1.1. Lens thickness.

Numerous studies have reported that the lens increases in thickness with age [Hoffer et al., 1993; Zadnik et al., 1995; Koretz et al., 1997; Glasser and Campbell, 1998; Strenk et al., 1999; Dubbelman et al., 2001a; Richdale et al., 2008], showing also a great intersubject variability. Hoffer et al. [1993] found that the thickness of the cataractous lens was directly proportional to age, with a mean of  $3.78 \pm 0.21$  mm in the third decade and a mean of  $5.03 \pm 0.46$  mm in the 10th decade. Using Scheimpflug imaging, Dubbelman et al. [2001] reported a linear dependency between lens thickness increases and age of  $LT = 2.93 (\pm 0.07) + 0.0236 (\pm 0.002) * \text{age}$ , while the posterior surface of the eye moved backward 0.015 mm per year. Atchison et al., [2008] found very similar rates using ultrasonography: anterior chamber depth decreased 0.011 mm/year and lens central thickness increased 0.024 mm/year.

#### 1.5.1.2. Anterior and posterior surface curvatures.

Several studies have shown that the unaccommodated lens steepens with age. Using Scheimpflug imaging, Dubbelman and Van der Heijde [2001] reported the following expressions for the change of the lens radii of curvature from the ages of 20 to 70:  $12.9 (\pm 0.4) - 0.057 (\pm 0.009) * \text{age}$ , for the anterior; and  $6.2 (\pm 0.2) - 0.012 (\pm 0.006) * \text{age}$  for the posterior surface.

Similarly, Atchison et al., [2008] reported a decrease of  $12.283 - 0.0438 * \text{age}$  in the anterior radius of curvature and  $7.1857 - 0.0076 * \text{age}$  in the posterior one, using Purkinje imagery.

If the refraction index of the lens was homogeneous and constant throughout live, this increase of the radii of curvature with age should result in an increase of the optical power of the lens. However, no tendency for myopia has been found. This has been called the lens paradox [Koretz & Handelman, 1986].

#### 1.5.1.3. Refractive index

Age-dependent changes in the refractive index distribution which compensate the decrease of the radii of curvature (and therefore increased surface power) of the relaxed crystalline lens with age were postulated by several authors [Koretz and Handelman, 1986; Hemenger et al., 1995; Garner et al., 1998]. The changes in the GRIN distribution with age have been suggested to be the reason behind the lens paradox [Moffat et al., 2002], compensating for the increased surface curvatures. While Glasser and Campbell [1998] found no age dependence of the *in vitro* lens equivalent refractive index, Moffat et al. [2002] and, more recently, Borja et al. [2008] and De Castro et al. [2011] reported a decrease in the equivalent refractive index with age. Finally, Uhlhorn et al. [2008] reported a decrease in the average (not to be mistaken with the equivalent) axial refractive index with age, using OCT.

*In vivo* studies in unaccommodated crystalline lenses with Scheimpflug [Dubbelman and Van der Heijde, 2001] and Purkinje images [Garner and Smith, 1997; Atchison et al., 2008] also found a decrease in the equivalent refractive index with age.

Besides, several authors have studied the refractive index distribution as a function of age. Using Purkinje photography and a very simple GRIN model, Hemenger et al. [1995] reported a significantly flatter refractive index near the lens center in older than in younger lenses. Jones et al [2005], Augustey et al [2008], de Castro et al. [2011] and Birkenfeld et al. [2014] also describe the progressive development of a central refractive index plateau area in the lens with aging using more direct techniques.

These results suggest that the change of the crystalline lens optics with age is not only due to the change of its shape but also to the GRIN distribution and others factors, such as the spherical aberration. However, the relative contribution of each factor to the optical power is still under discussion. Borja et al. [2008] found that surfaces contribute with a 40% to total lens power, a percentage that they report to remain nearly constant with age.

#### **1.5.1.4. Spherical aberration**

Different studies have reported an increase in the spherical aberration of the crystalline lens (and therefore, in the total one) with age, from the ordinary negative values in young eyes to less negative or even positive values in the old lens [Glasser & Campbell, 1999; Artal et al., 2002; Smith et al., 2001; McLellan et al., 2001]. In fact, the change of spherical aberration has been associated to the change of the refractive index distribution [Birkenfeld et al., 2013; de Castro et al., 2013; Birkenfeld 2014]. De Castro et al. [2013] found that the presence of GRIN shifts the spherical aberration of the lens from positive values (considering the same surface and a homogeneous refractive index) towards negative values. In *ex vivo* crystalline lenses, Birkenfeld et al. [2014] reported that both geometrical changes and GRIN contribute to the age-dependent shift of negative spherical aberration.

#### **1.5.1.5. Other changes**

It is known that the lens hardens with age, probably due to changes in the proteins and a decrease in its water content [Fisher, 1971; Fisher, 1977; Glasser and Campbell, 1999], while the lens capsule becomes thicker and less extensible [Krag et al., 1997].

The aging of the ciliary muscle has also been studied. In a sample of 95 enucleated eyes (age 33-87 years. mean 63.2), a morphometric study by Tamm et al. [1992] showed that ciliary muscle atrophies with age. However, Strenk et al. [1999] reported the presence of muscle contraction in all the 25 subjects (age range: 22-83) of their study, finding only a slight reduction with advancing age. On the other hand, they reported a decrease in the diameter of the unaccommodated ciliary muscle ring.

## 1.5.2. Changes in ocular optical quality with age

The age-related changes of the human crystalline lens affect our visual performance. After the age of 40-45 years, near objects cannot be focused any longer due to *presbyopia*. And after 60, many people experience blurring vision due to *cataracts*.

### 1.5.2.1. Presbyopia

Presbyopia is the loss of accommodation with age, what results in an inability to focus near objects in emmetropic individuals. The loss of accommodation ability occurs throughout all our life (see Figure 1.19), but generally goes unnoticed until accommodative amplitude is almost completely lost around the age of 40-45, causing problems to perform daily near vision tasks such as reading.

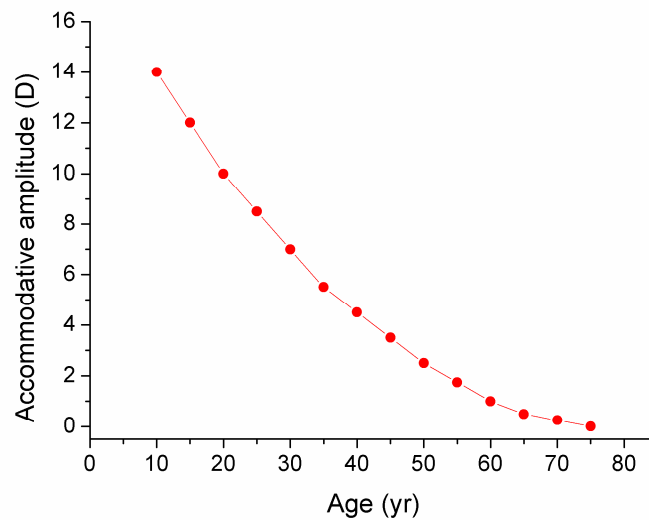


Figure 1.19. Loss of accommodative amplitude with age.  
Data obtained from Katz and Kruger [2009]

Presbyopia is generally assumed to be caused by the gradual hardening of the crystalline lens described above. The crystalline lens of the young eye is elastic, what allows its deformation for accommodating. The lens gradually hardens with age, losing its ability to deform and accommodate.

The most common solution for presbyopia is the use of spectacle lenses that the individual wears when performing near tasks, which introduce the needed optical compensation. An alternative solution is the use of bifocal, multifocal or progressive spectacles, generally known as alternating vision presbyopic corrections, contact lenses or intraocular lenses, which simultaneously allow vision at different distances, although at the cost of reducing the optical quality. Simultaneous vision corrections are also attempted in corneal surgery (LASIK or corneal inlay implantation). Another approach is monovision corrections, in which only one eye wears a correction (contact or intraocular lens) for near vision, while the other is corrected for far.

### 1.5.2.2. Cataracts

The loss of transparency of the crystalline lens (see Figure 1.20) is called a cataract. The development of cataracts with age is a common problem which reduces the clarity of

vision. The most common approach for treating cataracts is to surgically replace crystalline lens by an artificial intraocular lens (IOL). IOL's can be designed with a bifocal or multifocal profile in order to treat.

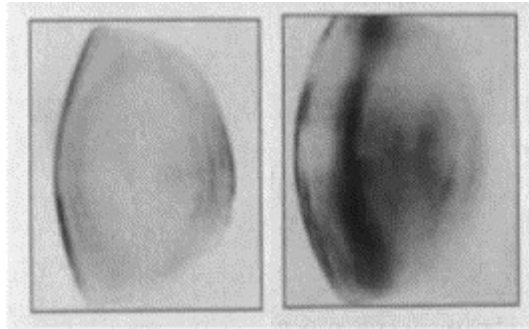


Figure 1.20. MRI cross-sections of a 19-year-old eye (left) and a cataractous 69-year-old eye (right).  
Obtained from Strenk et al. [2005]

### 1.5.2.3. The future: restoring accommodation

The solutions for presbyopia (and cataracts) described above do not allow the subject to regain the accommodation capability of a young eye. This implies the discomfort of either temporal solution (spectacles for near vision) or a permanent solution that decreases the optical quality of the images. Today, researchers and ophthalmic companies are working on solutions allowing the restoration of accommodation. While the aging crystalline lens loses elasticity and transparency, there is some evidence that the ciliary muscle functionality is partially preserved. Accommodative IOLs (A-IOL) aim at replacing the crystalline lens and most of them make use of the ciliary muscle contraction to restore accommodation. Different approaches have been proposed, such as a forward movement of a single optic IOL, increased separation of dual optic IOLs or a change in surface curvatures.

Up to now, the only model of accommodating-IOL approved by the FDA (US Food and Drug Administration) is the Crystalens (Bausch & Lomb, Rochester, NY). This first generation of A-IOLs is expected to move forward with the ciliary muscle contraction, changing the total power of eye. However, Koepl et al. [2005] evaluated a sample of 28 patients implanted with Crystalens and reported a backward shift of the lens of 151  $\mu\text{m}$  on average. Moreover, in a recent study with 20 patients implanted with Crystalens, using quantitative 3-D OCT anterior segment imaging Marcos et al. [2014] reported that the A-IOL did not shift systematically with accommodative effort: 9 lenses moved forward and 11 lenses moved backward (under natural conditions). The average A-IOL shift under stimulated accommodation with pilocarpine was  $-0.02 \pm 0.20$  mm. Other pseudo-accommodative solutions based on the same mechanism are the Tek-Clear (Tekia, Irvine, CA), the 1CU Akkommodative (Human Optics AG, Erlangen, Germany), the Tetraflex (Lenstec, St Petersburg, Russia) and the WIOL-CF (Medicem, the Czech Republic).

There are other approaches attempting to fully restore accommodation. The Synchrony IOL (AMO, Santa Ana, CA) is a single-piece dual-optic, silicone lens, composed of an anterior positive lens and a posterior negative one. These two lenses are separated by a spring-activated mechanism. The haptics separate the lenses at a given distance under constriction of the capsule, and during relaxation of the capsule -following accommodative effort- anterior movement of the positive anterior optic produces increased power for near tasks. This A-IOL is approved in Europe, but AMO

discontinued it in 2014 and did not further pursue the FDA approval in the United States.

The Lumina (Akkolens, The Netherlands) is also an accommodative IOL composed of two lenses based on the Alvarez principle: a lateral displacement between two lenses with a particular shape produces a change in the optical power of the system.

Other types of lenses try to emulate the morphological changes of the crystalline lens with accommodation. DynaCurve (NuLens Ltd., Herzliya, Israel) and FluidVision (PowerVision Inc., Belmont, CA) A-IOLs are two deformable silicon or fluid based lenses which pretend that the ciliary muscle constriction pressures them equatorially, changing their shape similarly to the crystalline lens. Potentially, they have the ability to provide a larger range of focus (between 5 and 10 D) than pseudo-accommodative IOLs.

Finally, a very different approach is followed by the Sapphire AutoFocal IOL (Elenza, Virginia). This electronically driven lens senses the pupil constriction and lighting conditions to change the index of refraction of a liquid crystal embedded within the IOL.

## 1.6. Imaging of the crystalline lens

The geometry of the two main optical elements of the anterior segment of the eye (the cornea and the lens) has been reported using different techniques and approaches. This chapter is mainly focused on the techniques providing *in vivo* imaging of the crystalline lens. However, it must be noted that the lens is viewed through the cornea, so that the measurement of the lens shape usually requires the prior measurement of the corneal geometry.

### 1.6.1. Ultrasound-based techniques

A widespread technique to measure axial intraocular distances is A-scan ultrasound biometry [Mundt and Hughes, 1956]. The technique has also been developed to produce 3-D images of the anterior segment of the eye (ultrasound biomicroscopy). These are contact techniques, which are routinely performed under topical anesthesia, what implies a great disadvantage with respect to the non-contact optical techniques.

Ultrasound techniques rely on the generation of high frequency sound waves (around 10 MHz) that penetrate the eye and give a measurement of distances between the probe and specific structures. The A-scan biometer sound beam produces echoes when it encounters a media interface with different densities. These echoes are then converted to characteristic spikes and visualized on the biometer's display system.

This technique was adapted by Beers & van der Heijde [1994b] to dynamically monitor biometric changes at 100 Hz. Thus, microfluctuations in the lens and axial length during steady state accommodation could be measured [van der Heijde et al., 1996].

A-scan ultrasonography has been extended to 2-D (B-scan ultrasonography) and 3-D (Ultrasound Biomicroscope, UBM). The first ocular UBM was developed by Pavlin et al., [1990]. It needs a higher scanning frequency (35–50 MHz) than the one used in ophthalmic A/B-scanners, resulting in an improved reported resolution up to 40  $\mu\text{m}$ . Figure 1.21 shows a cross sectional image of an *in vivo* anterior segment collected by an UBM.

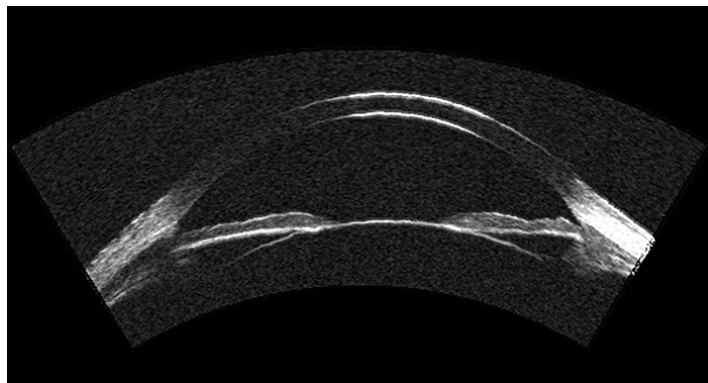


Figure 1.21. Anterior segment of the eye imaged with a UBM [Silverman, 2009]

### 1.6.2. Purkinje imaging

First described by Jan Evangelista Purkyně in 1832, Purkinje images are reflections of the light from the different ocular surfaces: PI and PII from the anterior and posterior surfaces of the cornea, respectively, and, more interestingly for us, PIII and PIV from the anterior and posterior surfaces of the crystalline lens. Purkinje images PIII and IV

(also PI) can be captured by imaging the eye's pupil, as they are formed close to the pupillary plane (see Figure 1.22). Although this technique does not provide an image of the anterior segment of the eye, it has been used to study the change of equivalent and gradient refractive index of the crystalline lens with accommodation [Garner & Smith, 1997], the biometric and phakometric changes with accommodation [Garner & Yap, 1997; Rosales et al, 2006], and the refractive index of the crystalline lens in young and aged eyes [Garner et al., 1998].

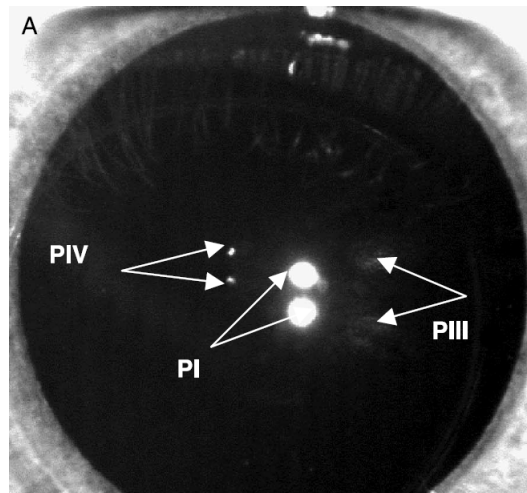


Figure 1.22. Purkinje images at the pupil plane. From Rosales et al. [2006]

### 1.6.3. Magnetic resonance imaging (MRI)

MRI is a non-ionizing technique that produces high quality images of the internal structures of the body. After applying a strong magnetic field to align the magnetic moments of the water hydrogen protons, the exciting electromagnetic field is turned off. The rates at which the protons decay to the initial state depends on the tissue, what produces different relative contrasts across the image. This technique is capable of producing undistorted images of the whole eye *in vivo*, and has been used to obtain quantitative information of the eye geometry and anterior segment biometry [Strenk et al., 2004; Jones et al 2005; and Kasthurirangan, et al, 2011]. Figure 1.23 shows two cross sectional images of an *in vivo* eye globe for different accommodative states. Among other disadvantages, MRI requires long acquisition times, with significantly lower resolution (around 0.2 mm) than optical techniques, which imposes major problems (including motion artifacts or low sampling density), preventing both quantification of the crystalline lens geometry with high accuracy and the study of its dynamics.

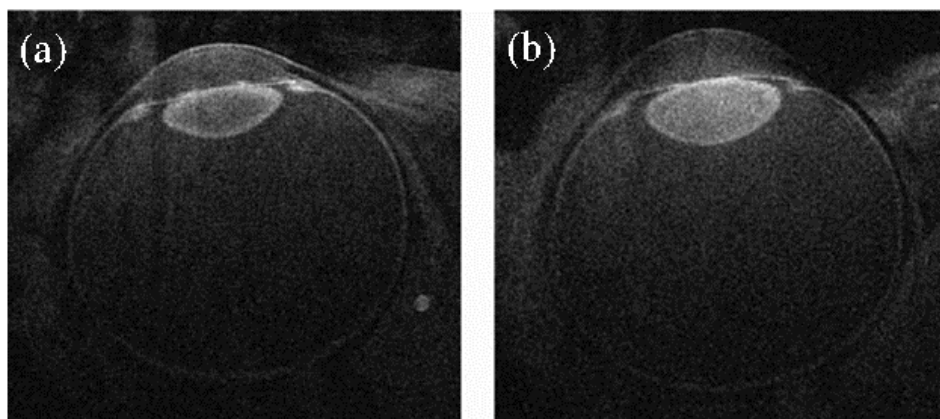


Figure 1.23. MRI images of the *in vivo* eye globe of a 23 years old subject with the crystalline lens unaccommodated (a) and accommodated (b). Adapted from Kasthurirangan *et al.* [2011]

#### 1.6.4. Scheimpflug cameras

Named after Theodor Scheimpflug, Scheimpflug's principle states that the object plane, the lens plane and the image plane intersects in a line (see Figure 1.24). The most familiar case of the object, lens and image planes being parallel one to each other would also satisfies Scheimpflug's principle, as they intersect at infinity.

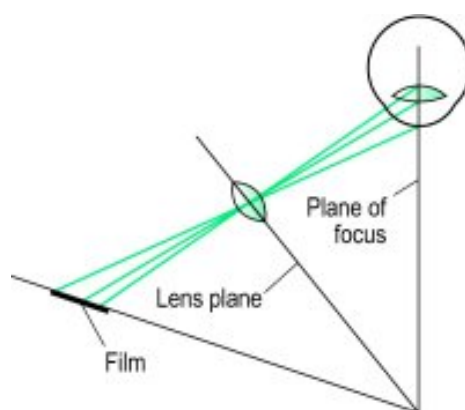


Figure 1.24. Scheimpflug's principle: object plane (in the eye), lens plane and image plane (the detector) intersect in a line

Scheimpflug systems take advantage of this geometric rule to achieve greater depth of focus and thus sharp images of the anterior segment, but it introduces a geometrical distortion because the magnification is not constant over the image. Additionally, Scheimpflug images are also affected by optical distortion, due to the fact that each of the ocular surfaces is seen through the previous one. Optical distortion is produced when a sample imaging embedded in a medium different from vacuum (air) is imaged. As light is bended at the media interfaces, it produces a very significant loss of the geometrical features of the observed surface, and therefore its geometrical parameters, such as curvature and thickness cannot be retrieved directly from the image. In order to obtain reliable information from those images, those distortions must be corrected.

Today, commercial Scheimpflug cameras record images of the anterior segment of the eye by rotating a "slit" beam of narrow light to obtain cross-sections across 25-50 meridians and reconstructing the maps of the structures. However, the slit-lamp configuration of Scheimpflug imaging-based systems frequently limits the view of the posterior lens. Commercial instruments provide quantitative information for the cornea

but not for the lens, since they do not correct from optical distortion in the lens region, which has to be performed in the post-processing processing with the approximation of a constant refractive index in the lens. Different studies report partial or total geometrical and optical distortion correction of Scheimpflug images to study the shape of the crystalline lens and its change with age and accommodation [Brown, 1973, 1974; Koretz et al., 1984, 2001; Dubbelman et al., 2001a, 2005; Rosales et al., 2006; Rosales and Marcos, 2009]. Figure 1.25 shows an image obtained with a Scheimpflug camera.

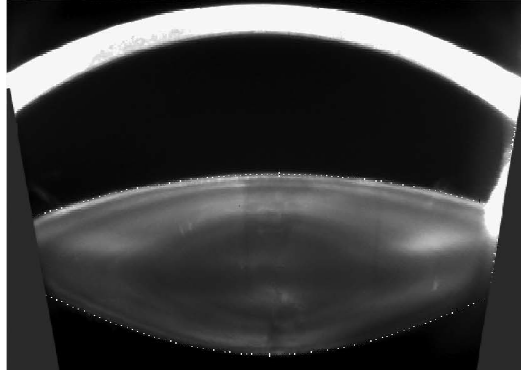


Figure 1.25. Corrected Scheimpflug image of an accommodated lens. Adapted from Rosales et al. [2006]

### 1.6.5. Optical coherence tomography

Optical coherence tomography (OCT) is a non-invasive, non contact imaging technique for high resolution, cross-sectional imaging of quasi-transparent media. OCT uses low-coherence interferometry to produce images from the light backscattered from tissue structures. An OCT image can be described as a collection of partial coherence interferograms (PCI), achieved using a scanning device to sweep the sample.

#### 1.6.5.1. Background: Partial Coherence Interferometry

Partial coherence interferometry (PCI) was first used in a 1-D optical technique called Optical Coherence Domain Reflectometry (OCDR) for inspection of fiber optic cables or network components [Youngquist et al, 1987, Takada et al, 1987]. The technique was soon applied to measure the axial length of the eye by Fercher et al. [1988], who used the interferometric properties of broadband light sources to measure optical distances.

PCI is most usually implemented on a Michelson interferometer configuration (see Figure 1.26). A low-coherence light beam is divided in two by a beam splitter, one directed to the sample (of amplitude  $U_S$ ), and the other to a reference mirror (of amplitude  $U_R$ ). The back reflected light coming from each arm (sample and reference) produces an interference signal that is recorded as a depth profile (A-Scan). The back reflected light from the sample is recombined with light from the reference arm by the beam splitter and it is led to a photoreceiver, passes through a signal processing unit and is stored in a computer for future displaying and post-processing.

If the object and reference beam had the same polarization, the intensity of the interference would be determined by Equation 1.7:

$$I=I_R+I_S+2E_R E_S \cos \delta, \quad \text{Equation 1.7}$$

Where  $I_{R/S}=(E_{R/S})^2$ , and  $\delta$  is the phase difference between both beams. Therefore, the first two terms are the DC term, resulting from the average temporal amplitude from the sample and reference arm, while last term is the AC part which expresses the difference in optical path of the two arms.

However, we cannot expect the object and reference beam to have the same polarization, so that the intensity of the interference is going to be fulfill Equation 1.8, a generalization of equation 1.7 that includes the concept of the complex degree of

$$\text{coherence } \mu_{RS} = \frac{\langle E_R E_S^* \rangle}{\sqrt{I_R I_S}}$$

$$I(\tau) = I_S + I_R + 2I_R I_S |\mu_{RS}| \cos(2\pi\nu_0\tau + \delta), \quad \text{Equation 1.8}$$

Where  $\tau$  is time difference produced by the spatial shift between arms and  $\nu_0$  is the central frequency of light spectrum. The last term can be seen as a narrow band signal, since it is the product of the band-limited signal  $|\mu_{RS}|$  and a carrier  $\cos(2\pi\nu_0\tau + \delta)$ , where, is the central frequency of the light spectrum and  $\delta$  is the phase difference.

Furthermore, Equation 1.8 does not take into account the random scattering of light in the tissue, which is generally not negligible and reduces the amount of back-reflected light. Although this scattering will produce a decrease in the contrast of the image, it will not prevent us from obtaining a high quality imaging of the anterior segment of the eye.

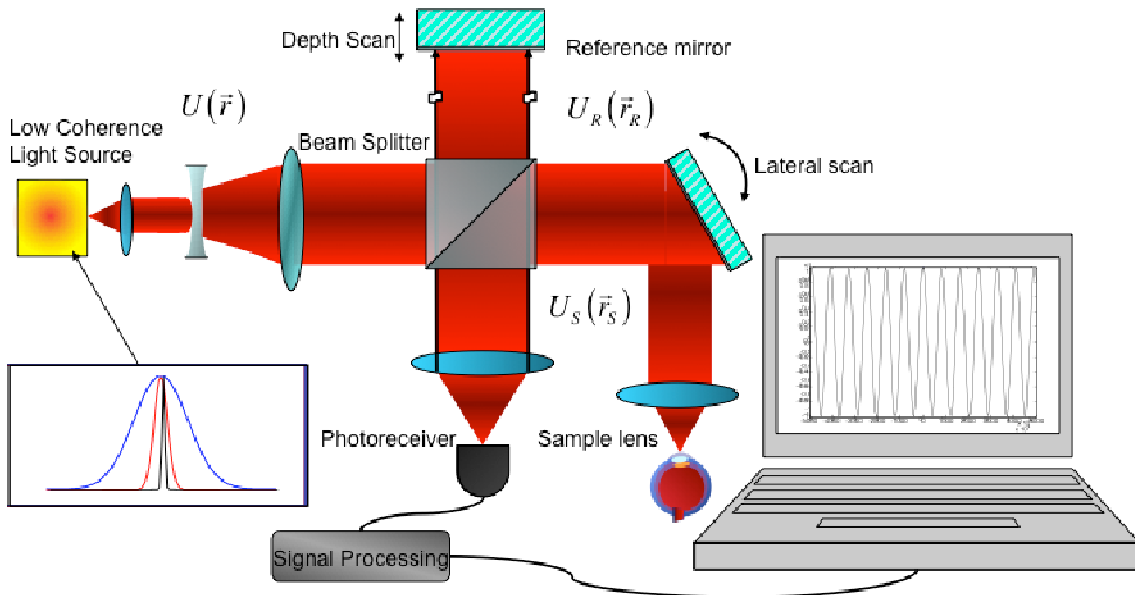


Figure 1.26. OCT with a Michelson interferometer configuration. The lateral scan of the mirror placed in front of the sample lens converts the PCI into an OCT system. From Sergio Ortiz's thesis manuscript

### 1.6.5.2. OCT techniques

An OCT system is basically the 3-D extension of PCI by using a pair of X-Y-scanners to obtain a volume image of the sample. Since the first development of Optical Coherence Tomography by Huang et al, [1991], the OCT technology has evolved from

the initially intuitive Time Domain OCT (TD-OCT) to the faster and more sensitive systems using Fourier analysis: Spectral-Domain OCT (SD-OCT) and Swept source (SS-OCT).

#### 1.6.5.2.1 Time Domain OCT

In a TD-OCT the location of scatters in the axial dimension of the sample is performed moving axially the reference mirror (see depth scan in Figure 1.26). The variable position of the reference mirror scans the sample and, when a structure backscatters light, interferometric fringes are generated. The photoreceiver detects the interference, which is electronically filtered and stored in the computer.

TD-OCT is generally implemented with a broadband light source (femtosecond laser, super luminescence diode) in the illumination channel. The bandwidth of the source has to be slim to guarantee a certain degree of coherence, but not too narrow to allow the detection of the scatter. This is illustrated in Figure 1.27, which shows how a change in the bandwidth of an ideal Gaussian spectrum affects the determination of the location of a scattering event.

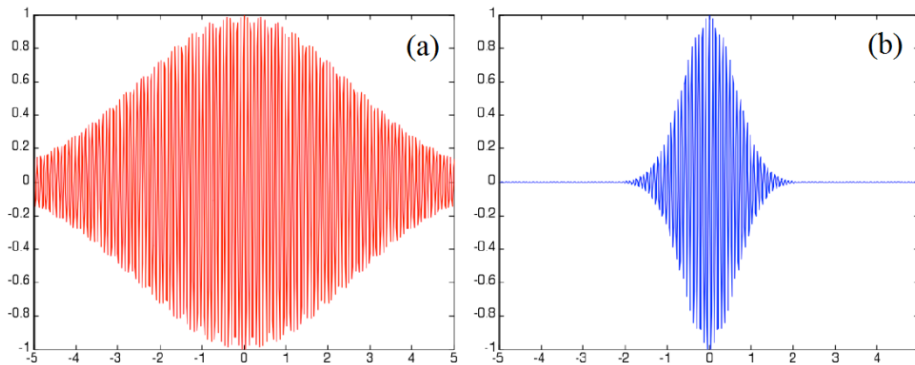


Figure 1.27. Influence of the bandwidth of the spectrum in the determination of the sample position. AC component is obtained for a Gaussian spectrum with a 5-nm bandwidth (a); and a 20-nm bandwidth (b)

#### 1.6.5.2.2 Fourier-Domain OCT

Fercher et al. [1995] were the first to propose Fourier domain OCT (FD-OCT). In these systems the reference arm stays fixed and the optical path length difference between sample and reference reflections is encoded by the frequency of the interferometric fringes modulating the power spectrum of the light source: increasing frequencies correspond to larger optical path lengths mismatches.

Two configurations have prevailed in Fourier domain systems: spectral domain OCT [Häusler et al, 1998; Wojtkowski et al, 2003; and Park et al 2005], and swept source OCT [Chinn et al, 1997, Yun et al, 2003, and Choma et al, 2005].

##### *Spectral Domain OCT*

Figure 1.28 shows the configuration of a fiber SD-OCT (or sOCT) consisting of a Michelson interferometer, a broadband light source and a spectrometer for decoding the spectral interferogram. The spectrometer is composed of a diffraction grating to separate the spectrum of light, a collecting lens and of a linear array sensor (linear CCD or CMOS camera).

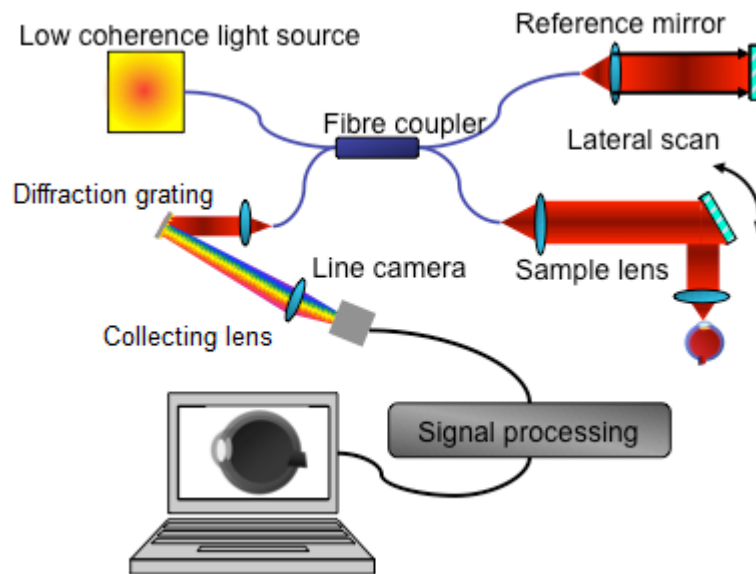


Figure 1.28 .SD-OCT configuration. The diffraction grating separates the spectrum and the line camera registers it to resolve the axial structures

If a population of  $n$  scatters is illuminated by an incoming beam, as in the PCI, the measured interferometric signal is the combination of  $n$  interferograms multiplied by the source spectrum. The resultant interferogram can be expressed as the sum of two non-interferometric spectral artifacts or DC terms, a cross correlation term (in which the terms of different frequency are involved), and an autocorrelation artifact.

The back-scattered axial profile can be obtained performing a Fourier transform. However, as a consequence of the symmetry properties of Fourier transform, a complex conjugate image is generated (see Figure 1.29). Further development of the FD-OCT system has been necessary to solve this problem [Szkulmowski et al., 2009].

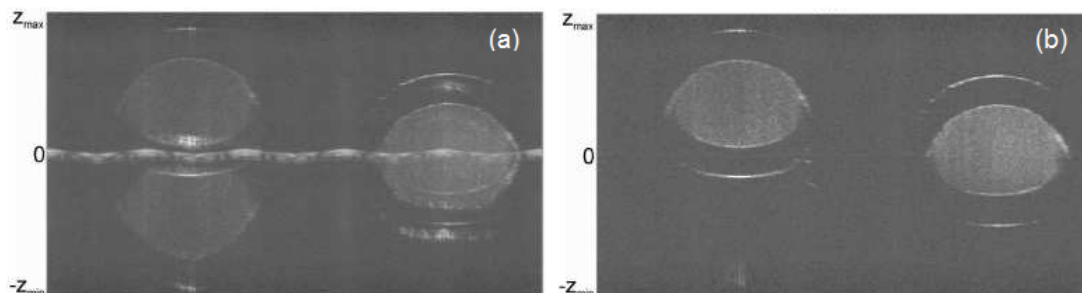


Figure 1.29. (a) FD-OCT image of the two vessels. (b) When removing the complex ambiguity image, the number and shape of the vessels become clear. Adapted from Szkulmowski et al. [2009]

### Swept Source OCT

While SD-OCT systems encode the frequencies in space to retrieve the A-scan, in SS-OCT modality they are they are encoded in time. The setup is again a Michelson interferometer with a narrow band laser, which is swept in time across a broad spectrum, for producing the partial coherence interferometry. A photodetector is responsible for the light detection.

Similarly to what happens in the SD-OCT modality, the temporal encoded light can be converted into an A-scan by performing a Fourier transform, but now the conversion

between time and wavenumber is used. Similarly, an echo artifact image is produced, which needs to be removed.

#### *1.6.5.2.3 Comparison across different OCT modalities*

The development of FD-OCT technologies has improved the characteristics of the technique in terms of speed and sensitivity, increasing the high potential of this method to registered images of the ocular globe. First, the absence of a reference depth scanning mirror in FD-OCT results in acquisition speeds hundreds or even thousands times larger than in TD-OCT, allowing more than one hundred thousand A-Scans/s.

The sensitivity of the different OCT modalities was analyzed by Choma et al. [2003], concluding that FD-OCT technologies are 20-30 dB more sensitive in terms of theoretical SNR gain than TD-OCT. However, the use of CMOS detectors -faster than other detector types, but with a higher readout noise- reduces the theoretical gain of SNR to around 10 dB in SD-OCT systems. Since SS-OCT uses PIN detectors, the increase in sensitivity is maintained.

The main drawback of the SD-OCT modality is the sensitivity drop-off, caused by the finite wavelength linewidth corresponding to each wavenumber. Overall, SS-OCT overcomes the main drawbacks of the SD-OCT, which are the sensitivity drop-off, and the resolution imposed by the finite size of the pixels of the camera, which removes the contribution of the higher frequencies. Its main drawback to date is the intrinsic instability of the light sources.

#### **1.6.5.3. State-of-the-art of the OCT**

Optical Coherence Tomography has resulted in an invaluable tool in medical imaging , particularly in ophthalmology (one OCT retinal image acquired every second somewhere in the world). There are two main benefits over other imaging modalities: its submicron axial resolution [Pozavay et al., 2002] and a light intensity level sufficiently low to be used in sensitive tissue [Swanson et al., 1993].

OCT was first developed for retinal imaging [Fercher et al., 1993; Swanson et al., 1993], where it can play an important role for the diagnosis and monitoring of a variety of macular diseases [Hee et al., 1995, 1996 and 1998] and glaucoma [Schuman et al., 1995].

The new technique was soon applied to the imaging of the anterior segment by Izatt et al. [1994], who developed a TD-OCT using a 1310 nm wavelength light. The introduction of the FD-OCT [Wojtkowski et al., 2003] extended the possibilities of the technique, by increasing its speed and improving the sensitivity [Choma et al., 2003] and signal to noise ratio [de Boer et al, 2003]. Experimentally, this allowed higher acquisition rates and lower energy exposure.

The visualization of the anterior segment with OCT has allowed numerous clinical applications including: pachymetric measurements of flap and stroma [Li et al., 2006], post-refractive surgery corneal evaluation [Avila et al., 2006; Salaroli et al., 2006], intracorneal rings surgery [Lai et al., 2006], keratoconus diagnosis [Li et al, 2008], tear meniscus evaluation [Savini et al., 2009], angle measurements for glaucoma diagnosis [Radhakrishnan et al, 2005], visualization of corneal scars [Khurana et al., 2007], and biometric measurements for IOL power calculations [Goldsmith et al., 2005; Tang et al., 2006].

However, the main limitation for the direct quantitative analysis of surfaces is the presence of two distortions that have to be corrected: the optical distortion and the fan distortion. Fan distortion arises from aberrations associated with the scanning system architecture, which typically consists of two-mirrors used to scan the beam laterally across the sample. This results in the system coordinates not being linear, and as consequence a flat surface imaged by the system appears curved. From the point of view of optical aberrations, the system can be considered to have an inherent astigmatism.

Therefore, in order to provide accurate topographies of the different surfaces of the eye, images must be corrected from the two types of distortion. Westphal et al. [2002] were the first to address the correction of both distortions in a 2-D OCT system, and later Podoloeanu et al., [2004] showed the first corrections of cross-sectional images of an intraocular lens, an intralipid drop, and the anterior chamber angle in a living human eye, also in 2-D. Westphal et al. [2002] already recognized that their proposed methods, based on the Fermat's principle, would improve if applying the optical correction in 3-D, instead of 2-D.

Several studies attempted to retrieve quantitative parameters of the ocular optical components, especially of the cornea [Gora et al., 2009; Zhao et al., 2010; Karnowski et al., 2011] but did not include explicit mention to fan distortion correction. Zhao et al. [2010] scanned the cornea meridionally, reporting only the corneal power. Gora et al. [Gora et al., 2009] presented a preliminary quantitative corneal analysis based on a swept source OCT using a meridian rastering protocol for collecting data. Karnowski et al. [2011] presented a corneal topography in a keratoconic subject in comparison with corneal topographies obtained from clinical instruments.

Ortiz et al. [2009] proposed a method to correct for fan distortion and the optical distortion [Ortiz et al., 2010] of 3-D images of the anterior segment obtained with OCT. Provided with automatic quantification algorithms and with fan and optical distortion correction, OCT has allowed 3-D quantification of the surface topography of the cornea [Ortiz et al., 2011; Karnowski et al., 2011], and lens [Ortiz et al., 2012], as well as 3-D optical biometry [Ortiz et al., 2013] and the assessment of implanted intracorneal ring segments [Pérez-Merino et al., 2013].

OCT provided with distortion correction algorithms allows the 3-D quantification of the anterior chamber segment. However, OCT imaging of the crystalline lens imposes some challenges: (1) Motion artifacts can limit the repeatability of the measurements, making it necessary to reduce acquisition time [Ortiz et al., 2011]; and (2) OCT has a limited axial range [Grulkowski et al., 2009], compromised by the resolution of the spectrometer (in spectrometer based OCT systems) or a limited instantaneous linewidth of tunable light source (in swept source OCT systems [Furukawa et al., 2010]), which may be insufficient to image the entire anterior segment of the eye. Several strategies have been proposed to overcome these limitations: doubling of the axial range by complex conjugate images removal [Grulkowski et al., 2009], dual channel OCT systems that combine two sOCT systems focused at different planes [Zhou et al., 2009; Dai et al., 2012; Shao et al., 2013], merging of images obtained focusing at different planes [Ortiz et al., 2012], optical switch to focus at different planes [Ruggeri et al., 2012], ultralong scan depth OCT [Du et al., 2012], and increased coherence length of swept sources [Grulkowski et al., 2012, Satoh et al., 2013]. However, none of them have provided a 3-D study of the lens accommodating for different demands.

Finally, the high speed acquisition of Fourier OCT techniques opens the possibility for tracking the crystalline lens dynamical changes, as the reported characteristic frequency of the fluctuations of accommodation falls within the bandwidth of state-of-the art OCT technology. However, to our knowledge no work has attempted to apply OCT to quantify the dynamics of the lens during accommodation.

## 1.7. Open questions addressed in this thesis

Aberrations have been shown to play a role on many accommodation-related mechanisms, from the onset of myopia to the determination of the direction of best focus. However, their role in many of this mechanism still needs to be clarified.

Different approaches can be followed to investigate the role of optical aberrations on the accommodative response, from studying the accommodative response in the presence of aberrations, to analyzing the changes in the geometry of the accommodating crystalline lens. A better understanding between lens geometry, aberrations and accommodative response will lead to a better comprehension of presbyopia and will also have an impact on the development of intraocular lenses and contact lenses for its correction.

Adaptive Optics is an ideal technique to manipulate high order aberrations and study their impact on accommodation. On the other hand, Optical Coherence Tomography (OCT) is a non-invasive high resolution technique which, properly calibrated, would allow an accurate quantification of the eye's structures, in particular the crystalline lens.

In this thesis the two techniques are used in order to specifically address the following open questions:

### **Accommodation accuracy**

High order aberrations have been shown to increase the depth of focus [Marcos et al., 1999b], which suggests that they might reduce the accuracy of accommodation. However, few studies have attempted to explore the influence of aberrations on accommodation. Collins et al., [1997] added  $-3$  D to  $+3$  D of spherical aberration through the use of aspheric surface rigid contact lenses, finding that negative spherical aberration caused an increase of the accommodative response and positive spherical aberration a decrease of it. Besides, López-Gil et al. [2007] studied the accommodative response in subjects wearing contact lenses that induced low and high values of third order aberrations and found a decrease in gain when around  $1\ \mu\text{m}$  (for a 5 mm pupil) of coma or trefoil were induced.

In this thesis, we will systematically explore how the presence of high order aberrations affects the accommodative response.

### **Fluctuations of accommodation**

#### *Active or passive mechanism*

Fluctuations of accommodation have been suggested to be an active method to maintain accommodation response and to play a role in obtaining directional cues for the dynamic accommodative response [Kotulak and Schor, 1986a, Gray et al., 1993a]. However, other authors have suggested that fluctuations of accommodation could be a passive consequence of the reduction in zonular tension with increasing accommodative response, which would allow increased freedom of movement of the crystalline lens [Miege and Denieul, 1988].

In this thesis we will modify the depth of focus by correcting/introducing high order aberrations on the stimulus: if the fluctuations of accommodations remain constant across aberrated condition, their passive nature will be suggested. If they decrease when

aberrations are corrected and increase when aberrations are induced, this will support the theory of being an active mechanism to maintain accommodation response.

#### *Fluctuation across accommodative response*

On the other hand, there is controversy on the dependency of fluctuations of accommodation with the accommodative response: Kotulak and Schor [1986b] reported an increase of the fluctuations of accommodation to steady target, while two other studies found a maximum for intermediate values of accommodation response [Miege and Denieul, 1988; Plainis et al., 2005].

This thesis will provide insights on the fluctuations of accommodation with the accommodative demands by aberrometry-based dynamic measurements of the accommodative response under manipulated aberrations, and by direct quantitative dynamic imaging of the crystalline lens.

### **Anterior chamber imaging during dynamic and static accommodation**

Quantitative imaging the anterior segment of the eye is relevant both for better understanding the optical properties of its components and for evaluating ophthalmic corrections.

Optical Coherence Tomography has become a promising tool to image the anterior segment of the eye, due to its high-resolution, high-speed and non-contact nature [Huang, 1991], overcoming other imaging techniques (MRI, ultrasounds and Scheimpflug photography).

However, OCT imaging of the crystalline lens imposes some challenges, including a limited axial range, which may be insufficient to image the entire anterior segment of the eye. Several strategies have been proposed to overcome these limitations: doubling of the axial range by complex conjugate images removal [Grulkowski et al., 2009], dual channel OCT systems that combine two sOCT systems focused at different planes [Zhou et al., 2009; Dai et al., 2012; Shao et al., 2013], merging of images obtained focusing at different planes [Ortiz et al., 2011], optical switch to focus at different planes [Ruggeri et al., 2012], ultralong scan depth OCT [Du et al., 2012], and increased coherence length of swept sources [Grulkowski et al., 2012; Satoh et al., 2013]. Some of these techniques have been successfully used to quantify the 3-D geometry of the anterior segment of the eye [Ortiz et al., 2012; Grulkowski et al., 2012].

In this thesis, we will extend the axial range by merging two sets of OCT images of the cornea and the lens. Provided with automatic quantification algorithms and with fan and optical distortion correction [Ortiz et al., 2009 & 2010], Fourier Domain OCT will allow us to quantitatively characterize three-dimensionally the crystalline lens geometry as a function of accommodation.

## **1.8. Goals**

The main goals of this thesis are:

- To investigate the effect of AO-correcting high order aberrations on the accommodative response accuracy.
- To investigate the effect of optically inducing high order aberrations on the accommodative response accuracy.

- To explore the effect of directly blurring the accommodation stimulus on the dynamic accommodation response.
- To show the capability of the OCT technique for imaging the anterior segment in 3-D for different accommodation states.
- To show the capability of the OCT technique for dynamically imaging the anterior segment for different accommodation states.
- To determine the influence of high order aberrations on the fluctuations of the accommodative response.

## 1.9. Hypothesis

These are the hypotheses of this thesis

- Accommodation accuracy increases when high order aberrations are corrected, and decreases when high order aberrations are induced.
- Fluctuations of accommodation increase when high order aberrations are corrected, and decrease if high order aberrations are induced
- Fluctuations of accommodation increase with accommodative response
- The radii of curvature of the anterior and posterior lens surfaces increase with accommodation effort, as well as the lens thickness and the position of the posterior surface of the lens. On the other hand, the anterior chamber depth decreases with accommodation.
- Fluctuations of accommodation are mainly associated to the dynamics of the anterior and posterior radii of curvature, rather than to a change in the axial position of the lens.

## 1.10. Structure of the thesis

The thesis has been organized in the following 6 chapters:

The current Chapter 1 is an introductory chapter that presents an extensive background on Visual Optics (with a special emphasis on the Accommodation mechanism), state of the art, and motivation of this thesis.

Chapter 2 describes the three different systems that have been used in this thesis: (1) a custom Hartmann-Shack-based Adaptive Optics setup developed in the Instituto de Óptica (Madrid, Spain); (2) an Infrared Recording Retinoscope at the SUNY College of Optometry (New York, USA) used during a short stay at Professor Philip Kruger's Lab; and (3) a Fourier Domain Optical Coherence Tomography system developed in collaboration with Nicholaus Copernicus University (Torun, Poland). Calibration, validation and software developed for controlling the systems are also described in this chapter.

In Chapter 3 we investigate the results of AO correction and induction of high order aberrations on the accommodative accuracy and on the fluctuations of accommodation. Accommodation is stimulated with a Badal system from 0 to 6 diopters under different aberrated conditions (including AO-correction, natural aberrations and induction of some high order aberrations terms) and the accommodative response measured with a Hartmann-Shack wavefront sensor. Measurements were taken during 5 seconds for every accommodation condition to estimate the fluctuations of the accommodative response.

Chapter 4 addresses the question of whether the retinal blur associated to the presence of high order aberrations affects the accommodative response. The accommodation target is mathematically convolved with the point spread function of certain aberrations, and the resulting images are projected to test the impact of the isolated retinal blur on accommodation, removing therefore the possibility of interaction between accommodation-related defocus and high order aberrations. Dynamic accommodation is here assessed by measuring the accommodative response to sinusoidal variations in accommodative demand.

Chapter 5 addresses imaging the accommodating crystalline lens as a function of accommodation using FD-OCT. Accommodation demand ranging from 0 to 6 diopters is induced, and fully corrected three-dimensional images of the anterior segment are obtained for the different conditions to characterize the lens geometry. Besides, dynamic 2-D images of the lens to study are acquired to the dynamics of the lens geometry with accommodation. To image the full anterior segment of the eye, two different images are obtained and merged using the iris or the limbus as landmark for registration.

Finally, Chapter 6 enumerates the conclusions of the thesis and identifies the new open questions arising from this work that can be addressed in future work.

## 2. METHODS

The current chapter describes the different systems used in this thesis:

1) A custom-built Adaptive Optics system developed with two different purposes: (1) to perform psychophysical experiments aiming at investigating the impact of aberrations on vision and neural adaptation to aberrations, and (2) to study the influence of high order aberrations on accommodation, one of the goals of this thesis.

The author of this thesis designed, implemented and calibrated the AO system in collaboration with Lucie Sawides, Carlos Dorransoro and Susana Marcos. He fully developed the software that controlled the AO system in synchronization with the Badal System for the accommodation experiments.

A description of the experimental system was first presented by Lucie Sawides at the “II Reunión Red Temática Española de Óptica Visual” (March 2007), in Murcia, Spain and at the 6th Workshop, Adaptive Optics for industry and medicine (June 2007) in Galway, Ireland, by Enrique Gamba.

2) An Infrared Recording Retinoscope, used during a short stay in Philip Kruger’s lab at the State University of New York. This system allows the projection of stimulus vergence changing measurements, following a sinusoidal- time dependence.

The author of this thesis used this system to study the effect of high-order-aberrations retinal blur on the accommodative response.

3) A custom-built anterior segment Spectral Domain OCT system capable of providing quantitative images of the anterior segment of the eye. The system was developed in collaboration with Michalina Gora, Ireneusz Grulkowski and Maciej Wojtowski from Nicholas Copernicus University (Torun, Poland) and Sergio Ortiz, Pablo Pérez-Merino and Susana Marcos at the Visual Optics and Biophotonics Lab.

The author implemented an additional arm into the original sOCT system to stimulate static accommodation by means of a Badal system.

## 2.1. Adaptive Optics system

One of the main goals of this thesis is to investigate the effect of high order aberration on the accuracy and dynamics of accommodation. Adaptive Optics is a technique capable of manipulating and measuring optical aberrations dynamically, appearing to be ideal for our purpose. In this thesis, a custom-built AO system provided with a Badal optometer for stimulating accommodation was developed.

### 2.1.1. Description of the AO system

The full Adaptive Optics system is depicted on Figure 2.1. It consists of different modules including: illumination, the Badal optometer, the Hartmann-Shack wavefront sensor (HSWS), the deformable mirror, the stimulus presentation channel (on a minidisplay) and a camera for pupil monitorization. A picture of the system highlighting its main components is shown in Figure 2.2.

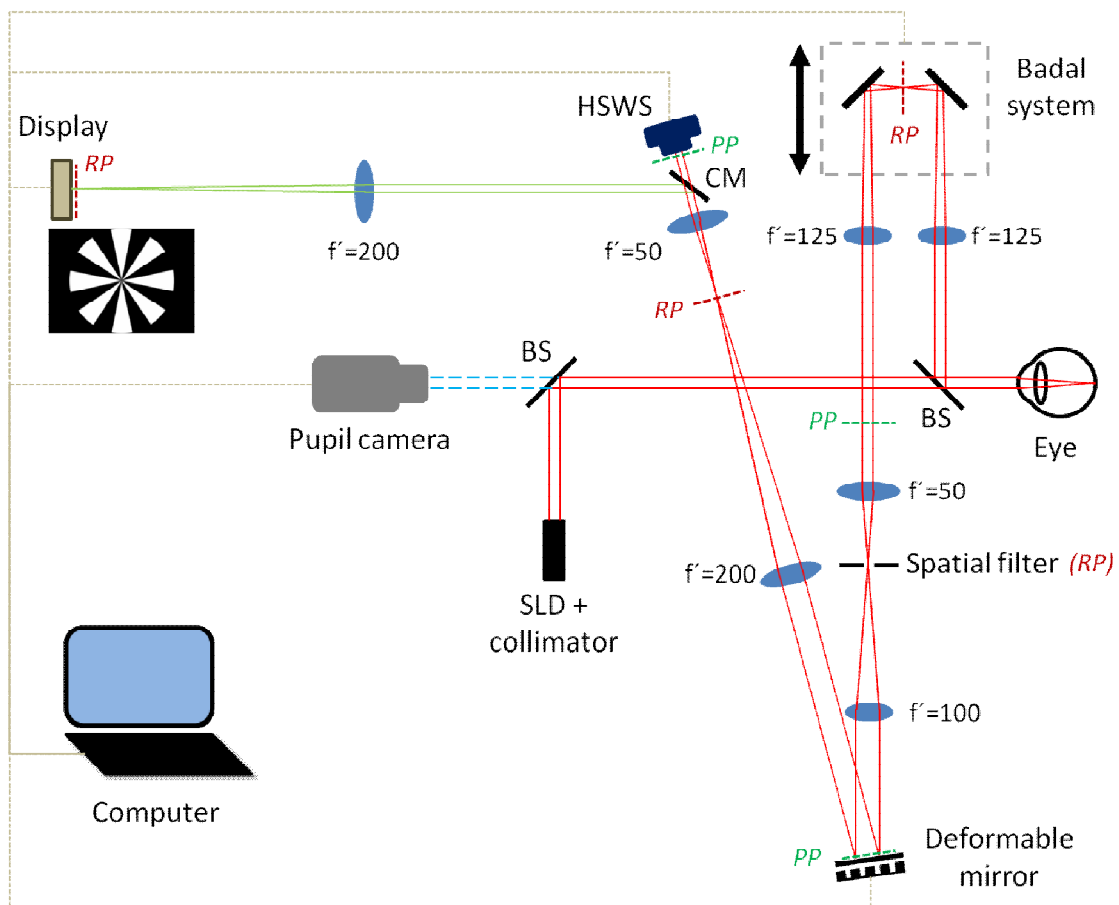


Figure 2.1. AO set up. The IR-beam from the SLD enters the eye and the backscattered light passes through the Badal system, is reflected on the deformable mirror and reaches the wavefront sensor. The subject's view is fixated by the stimulus display and his/her eye is continuously monitored with a pupil camera. Pupil planes (PP) are indicated in green and retinal planes (RP), in red.

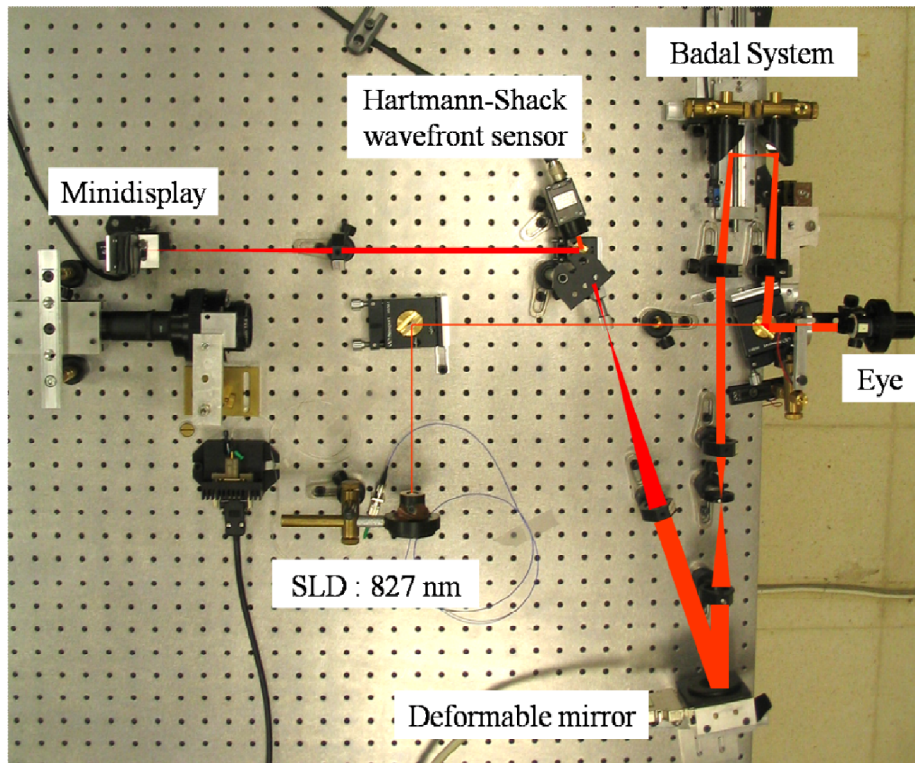


Figure 2.2. Picture of the AO system

### 2.1.1.1. Illumination

A collimated beam from a Superluminescent Diode (SLD) emitting at 827 nm (Superlum, Ireland) impacts the cornea with a 1-mm diameter. The beam is decentered by 1-mm off the pupil center to minimize corneal reflections in the Hartmann-Shack images. Figure 2.1 also shows an iris in a retinal plane which serves as a spatial filter to remove the remaining spurious reflection of the SLD beam coming from the cornea, which could affect the wavefront measurements.

The intensity of the light is controlled with a SLD module driving current set. A powermeter is used in order to obtain the correspondence between the SLD current and the irradiance at the pupil plane. This calibration curve is shown in Figure 2.3.

Maximum permissible exposure (MPE) from ANSI standards [Delori et al., 2007] calculated for our conditions of wavelength, beam diameter and exposure time (45 sec), is  $11.77 \mu\text{W}$ . Figure 2.3 shows corneal irradiance as a function of the SLD current. For safety reasons, current limit is set to 90 mA, corresponding to a maximum corneal irradiance of  $6.95 \mu\text{W}$ , below the MPE.

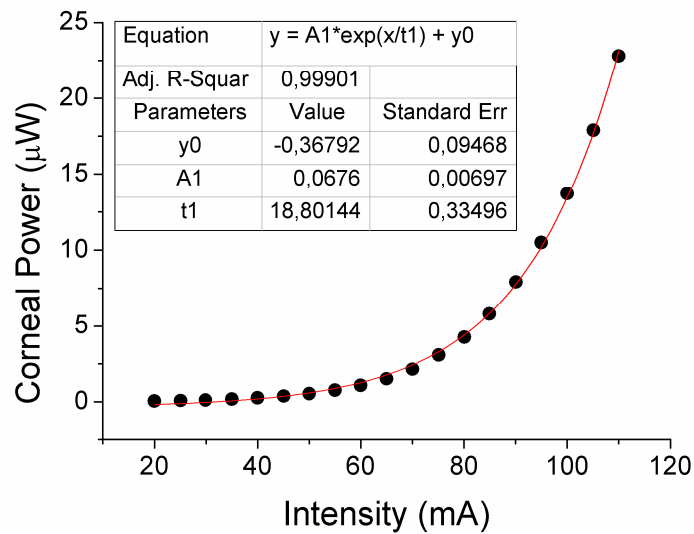


Figure. 2.3. Optical power on the corneal plane as a function of the intensity on the control module. Black circles are the experimental points and red line is the fitting to an exponential growth function. The parameters of the fitting are presented in the panel.

### 2.1.1.2. The Hartmann-Shack wavefront sensor

The ocular aberrations are measured with Haso32 Hartmann-Shack wavefront sensor (Imagine eyes, France). Haso32 is composed of a matrix of 32x32 microlenses and a CDD camera at the focal of the lenslet array. According to its specifications, this Hartmann-Shack sensor has a tilt dynamic range of  $\pm 3^\circ$ ; a tilt sensitivity of  $5 \mu\text{rad}$ ; a wavefront measurement accuracy below  $\lambda/100$ ; and a defocus dynamic range from  $\pm 0.015 \text{ m}$  to  $\pm \infty$ .

Besides, the effective diameter of the sensor is 3.65 mm. In our system, the microlens array of Hartmann-Shack wavefront sensor is conjugated to the subject's pupil with a x0.5 magnification factor. With this configuration, our system can measure aberrations on pupils of up to 7.15 mm of diameter.

### 2.1.1.3. The deformable mirror

The phase modulator of our AO system is an electromagnetic deformable mirror (MIRAO52, Imagine Eyes, France) with a high reflectivity ( $>98\%$  for 830 nm wavelength). The performance of this device was first described by Fernandez et al. [2006]. This mirror is composed of 52 actuators, with a separation of 2 mm. The maximum possible travel of the mirror surface (its stroke) is  $50 \mu\text{m}$ . The mirror has an effective diameter of 15mm (blue line in Figure 2.4), but a smaller diameter is recommended for a better reproduction of the high order aberrations (red line in Figure 2.4).

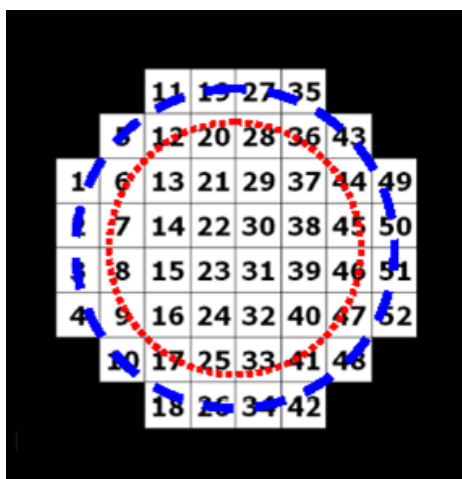


Figure 2.4. Actuator distribution of the Mirao52d under the membrane. Blue line indicates the effective pupil (15mm) and red line, the recommended pupil to reproduce high frequencies (11.89mm)

The angle in the deformable mirror between the incident and reflected beam is set to 15 degrees (see Fig- 2.1). A pair of relay lenses of focal lengths of 50 mm and 100 mm is used to conjugate the subject's pupil with the deformable mirror (x2 magnification), which guarantees that manipulation of aberrations can be performed on pupils below 7 mm of diameter.

#### 2.1.1.4. The Badal optometer

Correction of the spherical error of the patient and stimulation of accommodation is achieved with a Badal optometer, which change the vergence of the stimulus, but not its size. It consists of two fixed lenses ( $f=125$  mm) and a pair of mirrors with an angle of 90 deg between them and each at 45 deg from the optical axis. The two mirrors are mounted on a motorized linear stage (VXM1, Velmex) with an advance per step of 5  $\mu$ m. One of the advantages of this configuration is the prevention from stimulus magnification changes as the vergence is changed.

The displacement of the Badal system inducing a 1 D change was theoretically estimated under the paraxial approximation, according to the nominal focal distance of the two lenses. As a result, a displacement of 7.8 mm of the stage is equivalent to 1 D change of vergence. This mathematical estimation was experimentally validated in two ways:

First, the eye was replaced by a CCD camera placed at the focal length of a converging lens ( $f=35$ mm). Then, different accommodation states were simulated by inserting a set of positive trial lenses on a pupil plane. An image of the stimulus was acquired when the change of vergence induced by the trial lenses was compensated by the Badal system according to the theoretical calculations. The stimulus was also imaged when the Badal optometer was placed 1 mm (0.13D) before and after the expected position, to visually check if the stimulus was in focus (see Figure 2.5).

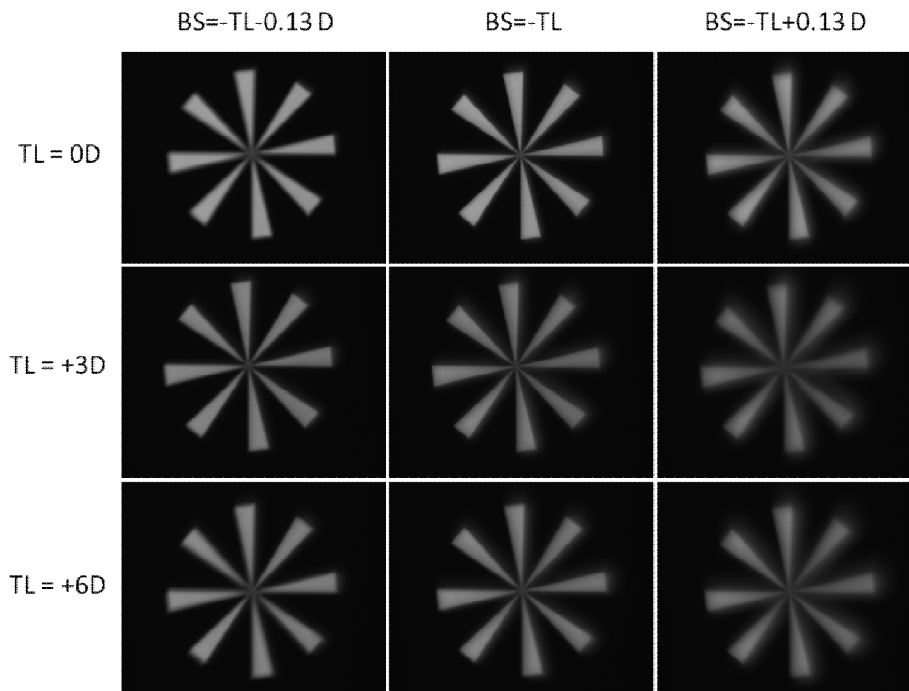


Figure 2.5. Images of the accommodation stimulus when different positive trial lenses were placed (in rows) and the induced changes of vergence were (theoretically) full-compensated with the Badal system (central column) and slightly over-compensated by 0.13D (left column) or under-compensated by 0.13D (right column). When the Badal system compensated for the trial lenses, the central area of the stimulus was sharper. This set of images also show that the Badal system preserves the size of the stimulus.

Besides, linearity of the Badal system was tested by performing a calibration with the Hartmann-Shack wavefront sensor. An artificial eye consisting of a 35 mm focal length achromatic doublet and a rotating diffuser as an artificial retina was used (referred to as Artificial Eye Doublet in the rest of the chapter). Defocus induced by the Badal optometer was measured with the Hartmann-Shack wavefront sensor from -8 D to 7 D (see Figure 2.6).

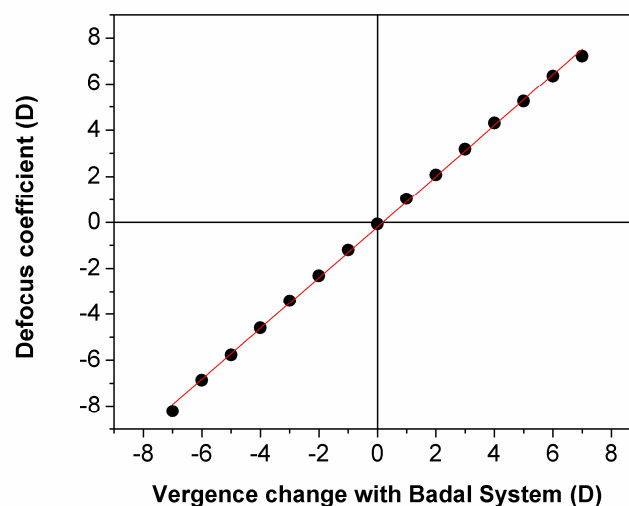
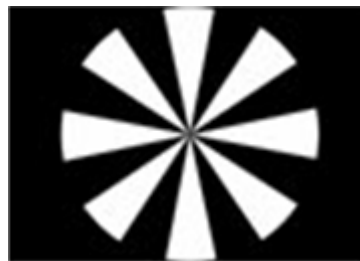


Figure 2.6. Badal system calibration: the defocus term measured with the Hartmann-Shack wavefront sensor is linear with the change in vergence introduced by the Badal optometer.

When performing measurements with real eyes, the Badal system is first used to compensate the residual refractive error of the subject. This subjective zero position is set by the subject by moving in 0.125 D steps the Badal stage, looking for the furthest point at which the subject can see the stimulus with sharp borders, not blurred because of defocus.

#### **2.1.1.5. Stimulus presentation**

A cold mirror placed in front of the wavefront sensor allows the insertion of a stimulus on a 12 x 9 mm (800 x 600 pixels) SVGA OLED minidisplay (LiteEye 400). The stimulus is a black and white Maltese cross with eight arms (see Figure 2.7), subtending 2.58 degrees on the retina. The luminance of the minidisplay was calibrated using a ColorCal luminance-meter (Cambridge Research Systems), resulting in 100 cd/m<sup>2</sup> and <0.5 cd/m<sup>2</sup> for white and black levels, respectively (contrast >0.99). Taking into account the light losses in the system, the effective luminance of the stimulus at the pupil plane is 50 cd/m<sup>2</sup>.



*Figure 2.7. Maltese cross used as stimulus for accommodation*

The choice of a Maltese cross stimulus is supported by numerous studies of accommodation in the literature [Mathews and Kruger, 1994]. This stimulus contains a wide range of spatial frequencies, providing at the same time a clear fixation position to minimize eye movements during the experiment.

#### **2.1.1.6. Eye alignment and stabilization**

A pupil monitoring channel, consisting of a CCD camera (TELI, Toshiba), is inserted in the system by means of a plate beam splitter. Subjects were stabilized with a bite bar and aligned to the system by means of an x-y-z stage and using the line of sight as a reference. During alignment, a ring of infrared diodes ( $\lambda=900$  nm) provides frontal illumination of the eye.

### **2.1.2. AO-correction procedure**

Correcting or inducing aberrations with a continuous mirror first requires to calculate the so-called command matrix. This command matrix indicates the voltage that should be applied to each actuator to generate certain patterns of aberrations (modes). Once the matrix is known, the particular correction or induction of aberrations needs to be applied.

#### **2.1.2.1. Command matrix construction**

The command matrix is characteristic of the optical system and it is computed before the experimental session by using the Artificial Eye Doublet and setting the current of the light source to 63mA to maximize the signal on the Hartmann-Shack wavefront sensor, without saturating it.

Experimentally, a  $\pm 0.2V$  is applied to each actuator, and its effect on the membrane is measured with the HSWS and saved in the so-called Influence matrix that records all the individual actuator's influence functions. Then, the interaction matrix is constructed using the full pupil diameter (7.2mm diameter).

Then, the command matrix is computed by pseudo-inverting the Interaction Matrix. A modal reconstruction algorithm projects measurements onto a polynomial perpendicular base of forty-eight modes, which are then translated to the Zernike polynomial base (up to 7<sup>th</sup> order) that are commonly used on visual optics.

The command matrix was calculated before every experimental session to ensure an accurate performance of the AO-system.

### 2.1.2.2. AO-correction

Once the Command Matrix is determined, the AO systems can correct or induced aberrations both in closed-loop or open-loop configurations.

#### 2.1.2.2.1 Closed-Loop operation

An AO system works in closed-loop mode when it is continuously monitoring and manipulating the wavefront. A closed-loop correction consists of an iterative process: first, the wavefront is measured; then, the voltages that must be applied to the actuators in order to change the shape of the mirror are automatically calculated; and the process starts again by performing a new measurement of the wavefront that checks if the target wavefront has been we have reached. Ideally, once the Command Matrix is known the target wavefront could be obtained in a single step. In practice, the iterative AO-correction would become unstable. For that reason, a gain factor is applied to the change in value sent to the actuators. Experimentally, we set a gain of 0.3 that allow us to reach the target state after 15 iterations.

Figure 2.8 shows the wave aberrations before and after the AO correction when the Doublet Artificial eye was placed in the system. RMS decreased from  $0.341 \mu\text{m}$  for a 6.5 mm pupil (excluding tilt and defocus) to less that  $0.01 \mu\text{m}$ , before becoming stable.

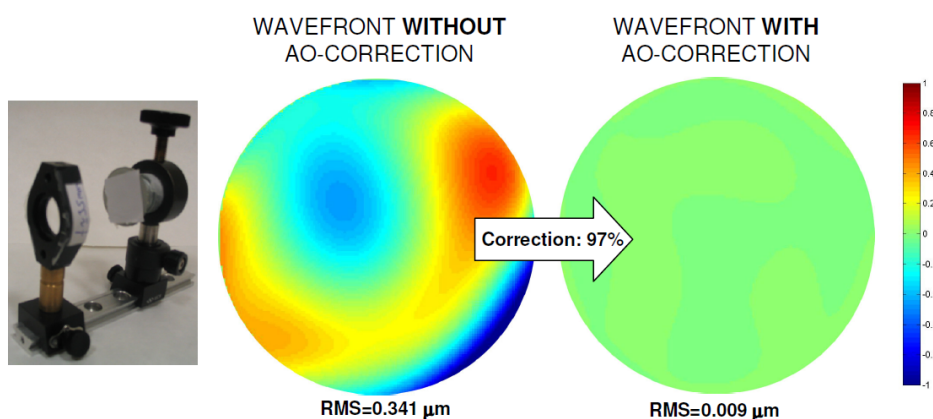


Figure 2.8. Wavefront reaching the HSWS when the Doublet artificial eye was placed in the system before and after AO-closed-loop correction. In this case a 97% of correction was achieved.

Once the target mirror is achieved, the AO-correction procedure keeps on, checking if the wavefront is still the desired one and ordering the mirror to react if the measurement varies from the desired state.

#### *2.1.2.2.2. Open-loop operation*

An AO system works in open-loop mode when the phase modulator state does not change during the experiment. To make the AO system work in open-loop configuration for inducing or correcting a certain amount of aberrations, it is first compulsory that a closed-loop operation has been made in order to obtain the state of the mirror that corrects or induces the aberrations. Once this state of the mirror (the voltages of each of the actuators) is obtained and saved to the computer, measurements in open-loop can be performed by the acquiring the wavefront with the HSWS while the mirror is set to the desired fixed state.

Since the open-loop correction is performed via a static mirror, dynamic changes in the wavefront shape during the measurement (due, for example, to eye movements) are not compensated. Therefore, closed-loop mode achieves a higher aberrations correction than open-loop mode.

However, in most of the experiments presented in this thesis the open-loop operation is used. The main reason is that closed-loop operation would also compensate for aberrations that play a role on the accommodation process, such as spherical aberration.

### **2.1.3. Setting up of the system**

#### **2.1.3.1. Optical alignment**

Alignment of the system was performed by using a visible laser to ensure proper placement of the different optical elements. During the alignment procedure the location of the different of pupil and retinal conjugated planes was carefully controlled.

#### **2.1.3.2. Evaluation of the mirror flatness**

An Artificial Eye Doublet was used to measure the aberrations of the system and determine the state of the mirror that removes the system aberrations. After closed-loop, mirror flatness was typically under  $0.02\ \mu\text{m}$  (see Figure 2.8). This state of the mirror that compensates the system aberrations is going to be referred as the “flat mirror” state and was recalculated periodically. When measurements were performed without either correcting or inducing high order aberrations, the mirror was set to this flat state.

#### **2.1.3.3. Mirror stability**

The performance of the Mirao 52d electromagnetic deformable mirror was extensively checked by Fernandez et al. [2006]. Figure 2.9 shows the HSWS measurement every half an hour during three hours for the same deformable mirror condition (generating  $0,5\ \mu\text{m}$  of spherical aberration), checked with the Artificial Eye Doublet. Fluctuations of the total RMS was less than 0.3% over a three-hour measurement, while the RMS of the individual aberration terms (up to 4<sup>th</sup> order) fluctuated less than 7%.

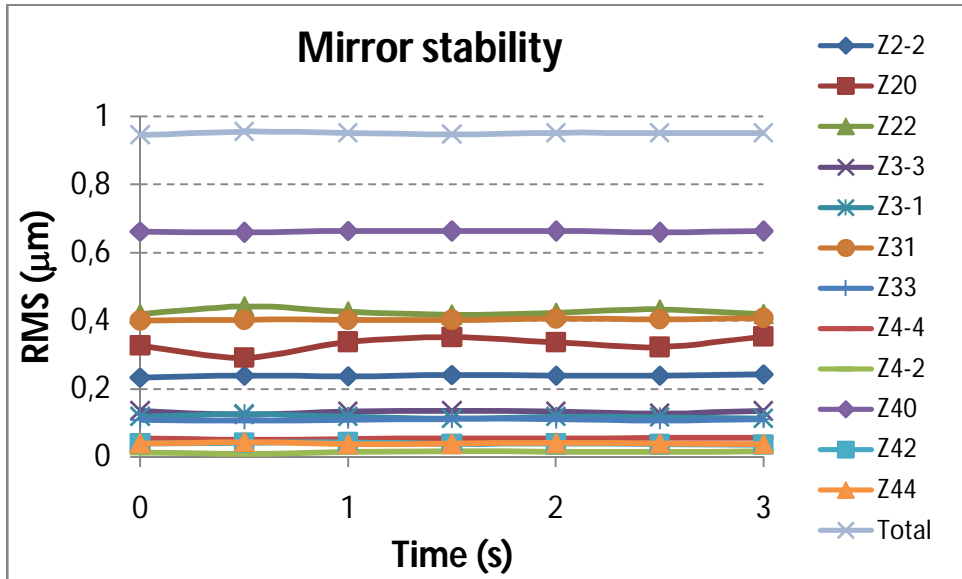


Figure 2.9. Mirror stability during three hours. Coefficients of the Zernike terms up to 4<sup>th</sup> order and total RMS (up to 7<sup>th</sup> order are plotted).

#### 2.1.3.4. Validation of the wavefront sensor

The performance of the AO system was validated using a second artificial eye with known aberrations (provided by Alcon, Spain). The experimental results obtained with our AO set up was compared with the nominal values of astigmatism, defocus, coma and spherical aberration of the artificial eye, as well as the value of the RMS of high order aberrations (HOA). Figure 2.10 shows that there was a good correspondence between the nominal and the experimental aberrations of the Alcon artificial eye.

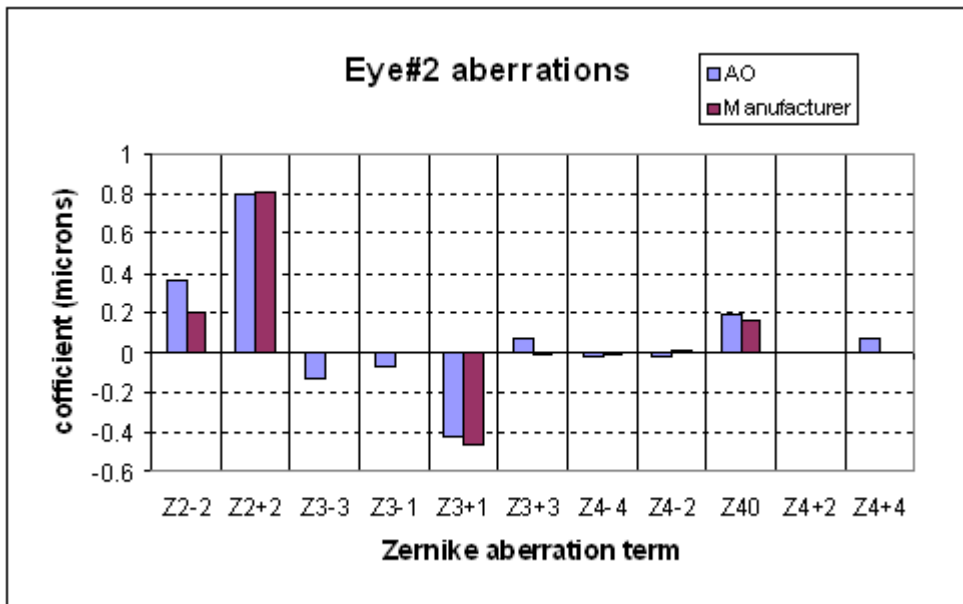


Figure 2.10. Comparison between the nominal aberrations of the artificial eye (provided by the manufacturer) and the experimental measurements with the AO system (6.5mm pupil diameter).

AO-correction of the aberrations of the Alcon artificial eye was also performed, resulting in a decrease of more than 96% of the initial aberrations, from 1.350 to 0.046  $\mu\text{m}$ , after eight iterations.

### 2.1.3.5. Badal system performance

The calibration of the Badal system and its linearity has already been shown in section 2.1.1.2. Further analysis of its performance was done by studying the change of the different Zernike terms measured with the HSWS. Figure 2.11 shows the results for the main polynomials. In particular, it can be seen that the spherical aberration (pink diamonds) does not change significantly when moving the Badal system: that is relevant since spherical aberration contributes to the estimated accommodative response.

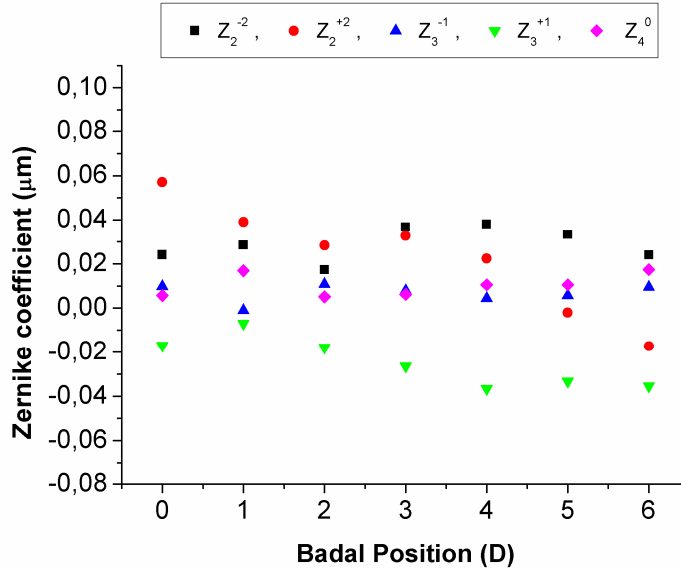


Figure 2.11. Change in the coefficients of the most relevant Zernike terms with Badal displacement. Except for  $Z_2^{+2}$  astigmatism, no significant tendency was found.

### 2.1.4. Automatic control interface

Custom-developed software is used to synchronize the wave aberrations acquisition with the movement of the Badal platform during the experimental session. The program is written in VisualC++.net, with the use of the DLL libraries for the motorized stage, the deformable mirror and the wavefront sensor and the Software Developer Kit provided by Imagine Eyes for the control of the Haso 32d and the Mirao. Figure 2.12 shows the interface of the custom-developed software

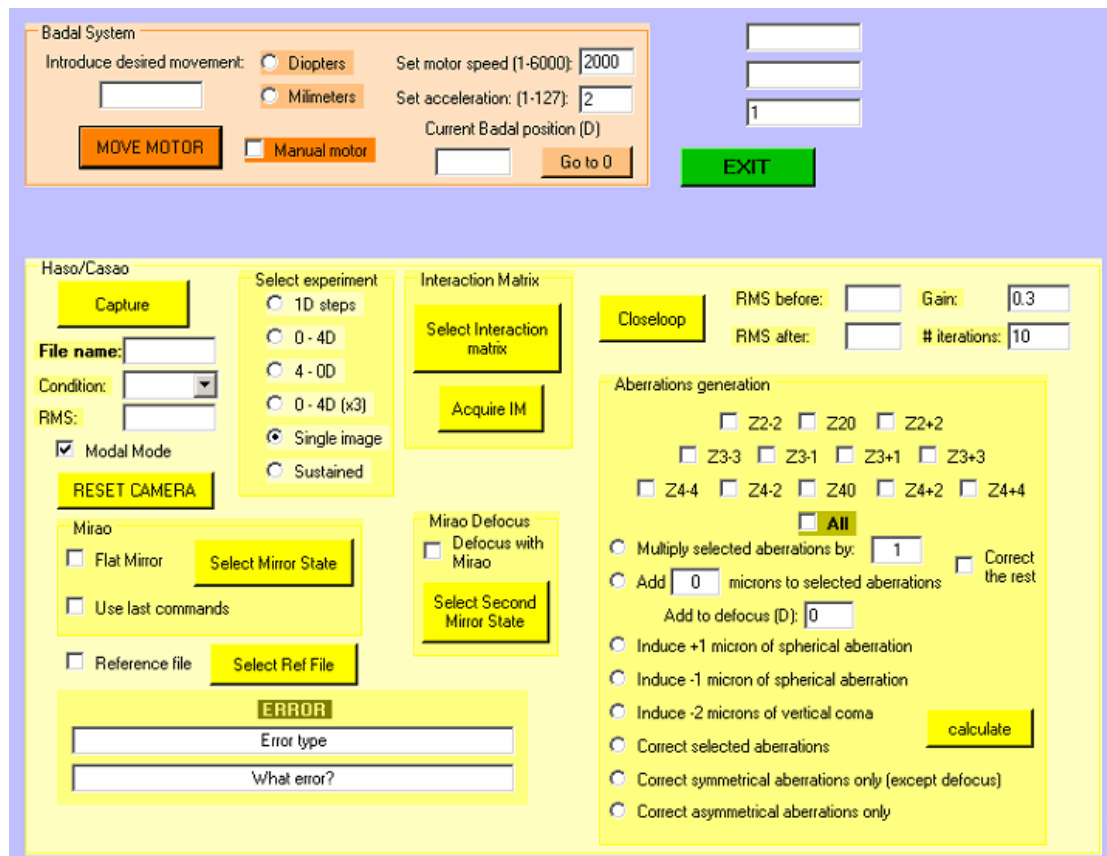


Figure 2.12. Interface of the custom developed software for synchronizing the Badal movement with the AO elements (HSWS and deformable mirror).

#### 2.1.4.1. Badal System module:

This module offers several options of moving the Badal system: (a) the experimenter can introduce the desired refractive change, either in mm of stage displacement or in diopters; (b) if the “manual motor” box is checked, the subject can move the Badal stage while viewing a stimulus through the system using the keyboard (up and down arrows) searching for his/her best spherical correction. The module also displays the current Badal position by double-clicking the corresponding textbox and includes the possibility of moving the stage directly to the zero position, not allowing exiting the program unless the Badal is set to zero. The speed of the motor can be modified, although a value of 10 mm/s is always used.

#### 2.1.4.2. Haso/Casao module:

This module allows multiple functions regarding the use of the HSWS and the deformable mirror.

- Acquisition and saving of wave aberrations

By clicking the “Capture” button, wave aberrations are measured with the HSWS. Depending on the selection in the “Select experiment” panel, a different set of measurements are performed, from a single measurement to a continuous data acquisition during which the Badal stage is moved. HSWS results are saved in a text file with the name of the subject, the date and time of every measurement and the aberrated condition (chosen among a list of possibilities).

By clicking the “Select Mirror state” button in the Mirao box, an explorer window is opened, allowing setting the deformable mirror in any state previously calculated. Shortcuts to the last state and to the flat mirror state (which corrects the system residual aberrations) are also available in this box.

- Interaction Matrix box

Interaction matrix is calculated by clicking the “Acquire IM” button. Once the interaction matrix is calculated, it is loaded in our software by clicking the “Select Interaction matrix” button. Then, our software calculates the Command matrix that will be used for AO-correction/induction.

- AO-correction

Once the interaction matrix is loaded, the software allows the correction of aberration in a closed-loop. The gain and the number of iteration can be chosen, but the default values are 0.3 and 10, respectively. RMS of the initial and the final wavefront are displayed in the corresponding textboxes. The mirror state is saved in the proper folder with a file name including the day and time of its creation.

- Generation of aberrations

Alternatively, command matrix can be used to generate an aberration pattern using the “aberration generation” panel. By selection either the desired aberration term to be induced and its amount, or one of the predefined options in the list, a closed-loop operation is performed in order to achieved the target state of the mirror.

### 2.1.4.3. Pupil monitoring

A software program written in VisualBasic.net is used to monitor the subject’s pupil during the alignment. Figure 2.13 shows the user’s interface of this program. Other features appearing in the interface, such as Badal system control or pupillometry box, are added for other studies.

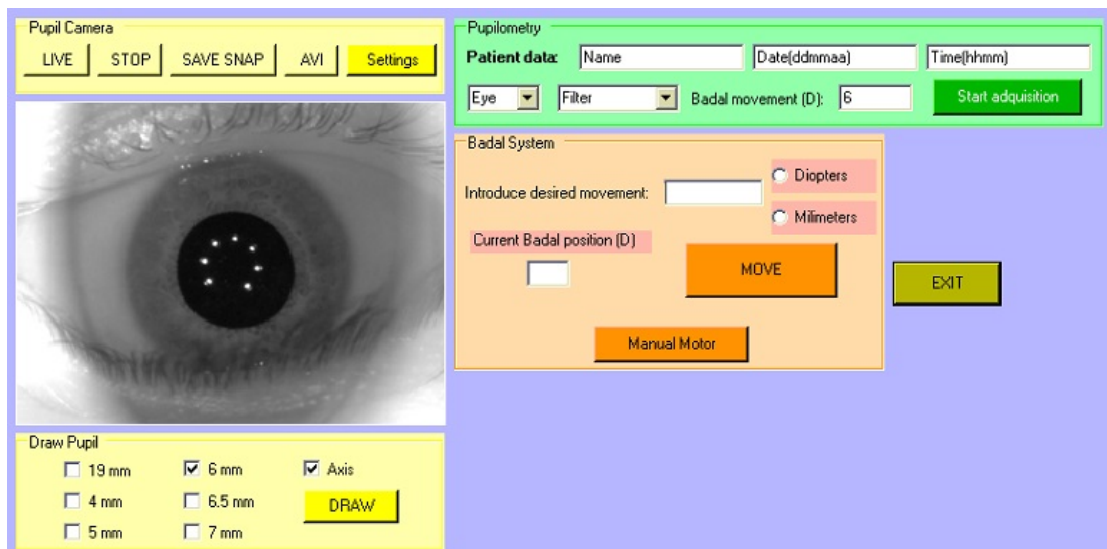


Figure 2.13. Interface of the custom developed software to control simultaneously pupil (yellow box) and Badal platform (orange box) position. Green box was added later for other purposes.

## 2.2. Infrared recording retinoscope

To study the accommodative response to a blurred stimulus an infrared recording retinoscope is used. The retinoscope is implemented in a system that allows dynamic stimulation of accommodation by means of a Badal: by moving the two lenses of the Badal system a sinusoidal accommodative demand is introduced. The accommodative response is expected to track the demand with a lower amplitude and a phase delay, both dependent on the subject and other factors. A Fast Fourier Transform of the accommodative response must to be performed in order to obtain its amplitude for the frequency of the stimulus.

### 2.2.1. Apparatus

Figure 2.14 shows a diagram of the experimental set-up [Kruger, 1979]. The stimulus is presented on the micro-mirror display of a modified high luminance video projector (Sharp NoteVision). An interference filter ( $\lambda=552\text{nm}$ , BW 10nm) is used to minimize any polychromatic cue for accommodation. Vergence (Zernike defocus) is changed with a Badal system, while dynamic accommodation is continuously monitored (100 Hz) with a high-speed infrared optometer. The output voltage of the optometer is linear to the accommodative response over a 6 D range [Kruger, 1979]. After analog-to-digital conversion, data are recorded to the computer using Asyst Scientific software (Metrabyte Corporation). Measurements of accommodation are recorded along the vertical meridian of the eye from a fixed 3 mm diameter area at the center of the subject's natural pupil. The subject's pupil is monitored by a video-camera (30 frames/s), and the image of the pupil viewed on a video display allowing the experimenter to adjust the position of the subject's eye continuously during the experiment.

A pupil diaphragm conjugate to the natural pupil's plane is set to 3-mm in order to reduce the effect of the subject's own aberrations.

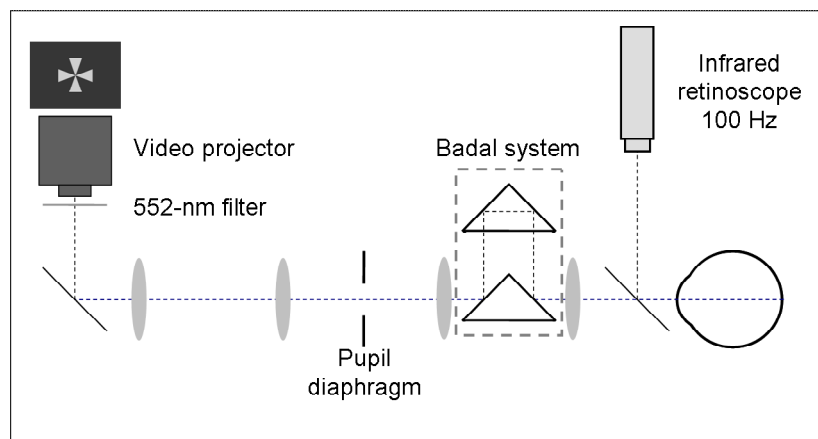


Figure 2.14. Experimental setup: The target is presented on the micro-mirror display of a video projector and its vergence (Zernike defocus) modified by means of a Badal optometer. Dynamic accommodation was recorded at 100 Hz with an infrared retinoscope.

## 2.3. Spectral-Domain OCT system

A custom SD-OCT system is used in this thesis to study the changes of lens geometry with the accommodative effort. The system was developed in collaboration with Nicolaus Copernicus University (Torun, Poland) [Grulkowski et al, 2009]. A schematic diagram of the system is shown in Figure 2.15.

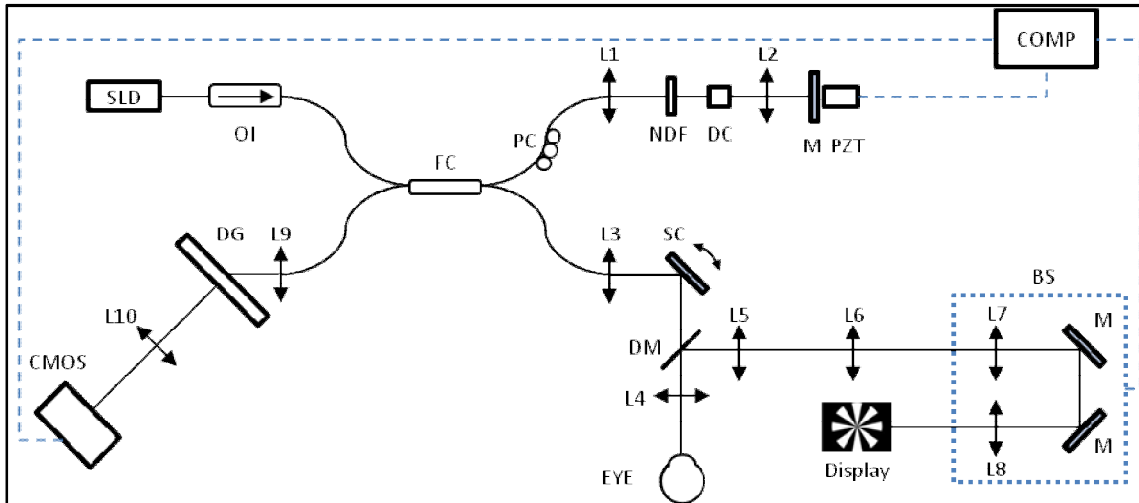


Figure 2.15. Experimental sOCT set-up: the system is based on a Michelson interferometer. See Figures 2.16 to 2.20 for a description of the different elements. The CMOS detector, the piezoelectric actuator, the motorized translational stage of the Badal system and the display are driven by a computer (COMP).

### 2.3.1. Configuration of the system

The set-up is based on a fiber-optics Michelson interferometer configuration with an 80:20 fiber coupler that divides the system in the following parts:

- The **illumination channel**, consisting of a superluminescent diode SLD ( $\lambda_0=840$  nm,  $\Delta\lambda=50$  nm; Superlum, Ireland) as a light source that is followed by an optical isolator (OI) joined by a fiber mate to a Fiber coupler (FC) in order to avoid that backreflected light from the reference and sample arms returning to the SLD. The light coming from the illumination channel enters the FC and is split by the fiber coupler into the reference and sample arms.

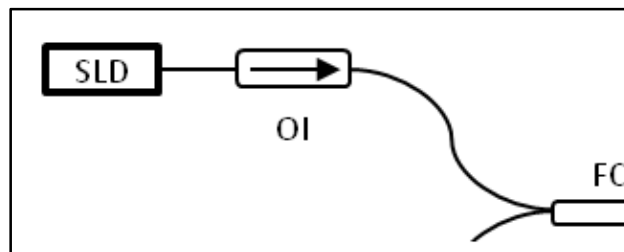


Figure 2.16. Illumination channel of the sOCT. SLD-superluminescent diode, OI-optical isolator, FC-80:20 Fiber coupler

- The **reference arm** is formed by a polarization controller (PC) to optimize detection performance, a converging lens to produce a collimated beam, a neutral density filter (NDF) to control the power of light in the reference arm, a converging lens that focuses the light on the mirror (M) and a piezotranslator (PZT) that will allow to remove the complex conjugate ambiguity.

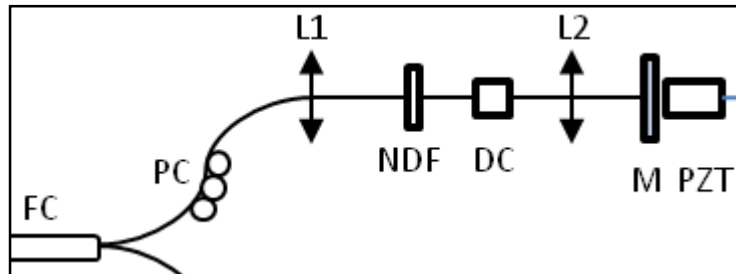


Figure 2.17. Reference arm of the system. FC- 80:20 Fiber coupler, PC-polarization controller, NDF- Neutral density filter, DC-dispersion compensator, PZT piezoelectric actuator

- The **sample arm** consists of a converging lens that collimates the light onto a XY galvanometric optical scanner to produce the horizontal and vertical rastering of the sample, and finally a 75 mm focal lens to collimate the chief rays of the beams and to focus the irradiance on the sample.

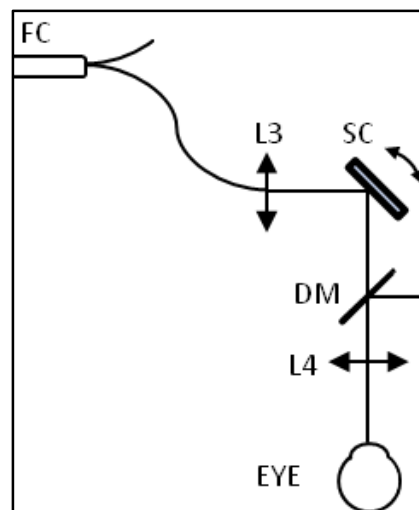


Figure 2.18. Sample arm. SC-scanning mirrors, DM-Dichroic mirror

Furthermore, the original system is modified to add an **accommodation channel** via the dichroic mirror DM. The accommodative stimulus, an eight-pointed black and white star, is projected on a minidisplay (Lite Eye) and its vergence can be changed thanks to a Badal system mounted on a motorized translation stage (Velmex). A pair of relay lenses extends the path to allow the insertion of the stimulus on the sOCT system (more information of this channel in the next section).

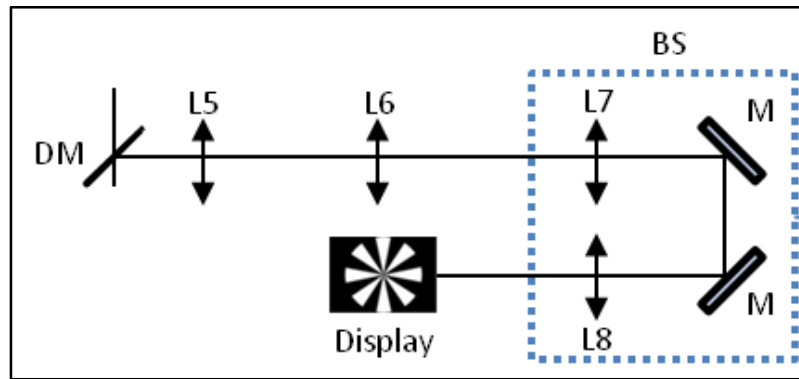


Figure 2.19. Accommodation channel. DM-Dichroic mirror, BS-Badal system. The two mirrors of the Badal system are mounted on a translational stage that can move back and forth with respect to L7 and L8 to change the stimulus vergence.

- In the **detection channel**, the light backreflected by the reference and sample arm is recombined by the fiber coupler. This channel consists of a converging lens to collimate the light, a volume diffraction grating to spatially separate the spectrum and an objective converging lens that images the fringes on a 12-bit line-scan CMOS camera with 4096 pixels (Basler sprint spL4096-140k; Basler AG, Germany).

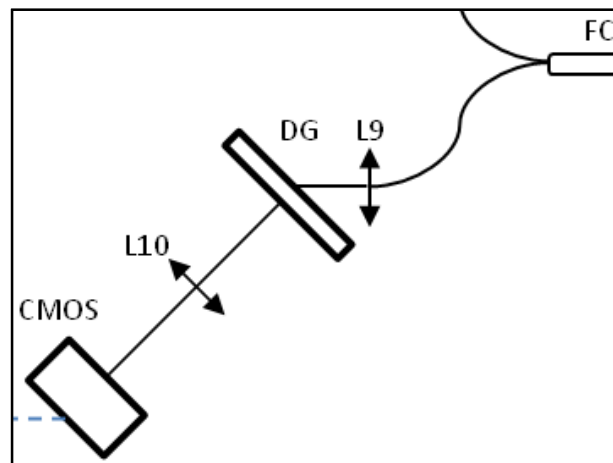


Figure 2.20. DG diffraction grating, CMOS linescan camera

The effective acquisition speed of this system is up to 150000 A-Scans/s, although the typical speed used for the experiments in this thesis was around 25000 A-Scans/s, since it showed as a good compromise between speed and optical quality of the image. The axial range of the instrument is 7 mm, and the theoretical axial resolution 3.4  $\mu\text{m}$  in air. The signal to noise rate (SNR) of the instrument was estimated to be 97 dB.

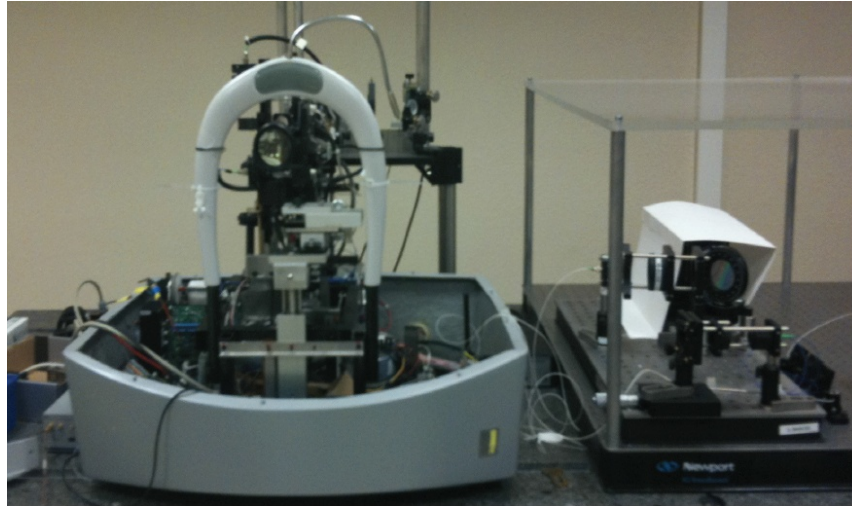


Figure 2.21 Actual implementation of the device. In the left side of the picture, the commercial system (sOCT Copernicus by Octopol, Poland; now Canon, Japan) in which our device is based can be seen. The accommodation channel is placed behind. In the right side of the picture, some optics for the calibration of the reference and detection arms can be seen in the front part, and the actual detection channel in the back: CMOS camera is hidden and a white card, with the holographic detection grating in front of it.

## 2.3.2. Control of the system

No synchronization was performed between the acquisition of the images and the accommodative stimulus presentation: the two of them were independently controlled.

### 2.3.2.1. sOCT system

The calibration and acquisition of the system involves three packages of routines:

- *Calibration software*, which allows the optimization of the optical elements and the estimation of the theoretical resolution and the SNR of the system. A full calibration of the system was performed regularly.
- *Measurement software*, for the acquisition of the images with different values of integration time, number of A-scans per B-scan (points in the horizontal dimension) and total number of B-scans (points in the vertical dimension), and vertical and horizontal measurement ranges.
- *Post-processing software*, to obtain the 3-D images (in a set of B-scans) from the raw data file. The images resulting from this post-processing software need to be further processed to obtain the quantitative parameters.

Ortiz et al., [2012] evaluated the sOCT accuracy for calculating the radii of curvature of the crystalline lens on a physical model eye. The results obtained with fully corrected OCT images were compared with the nominal values of the model eye surfaces. Discrepancies were below 3% for all surfaces, and repeatability was typically better 2%.

### 2.3.2.2. Accommodation channel

The Badal optometer in the sOCT system is similar to that of the AO system (see section 2.1.1.4): it consists of two fixed lenses ( $f=100$  mm) and two mirrors mounted on a motorized stage (Velmex). The displacement of the mirrors in order to induce a 1 D change was theoretically estimated under the paraxial approximation, obtaining a value of 5.0 mm. This mathematical estimation was validated by imaging a millimetric

reticule placed on the minidisplay plane with a CCD camera (Teli). Vergence was changed with the Badal system from -6D to 6D (in 1-D steps) and compensated with trial lenses placed on a pupil plane. In all conditions, the image remained in focus.

When performing measurements with real eyes, the Badal system was first used to compensate the residual refractive error of the subject. This subjective zero position was decided by the subject by moving in 0.125 D steps the Badal stage, looking for the point at which he/she first could see the stimulus with sharp borders, not blurred because of defocus.

A VisualBasic.Net software program was written to control the Badal system, with analogous options to the Badal system module in the AO-software in section 2.1.5. The program allowed the experimenter to induce any amount of diopters (typically 1D), or if the “manual motor” box was checked, the subject could move the Badal stage while viewing a stimulus through the system using the keyboard (up and down arrows) searching for his/her best spherical correction.

### **3. INFLUENCE OF HIGH ORDER ABERRATIONS ON ACCOMMODATION PERFORMANCE**

The full development of a study to investigate the impact of high order aberration on the accommodation process using the AO system previously described is shown in this chapter.

The author designed the study and the experimental protocols in collaboration with Susana Marcos and collected and processed the data.

The results of the study were totally or partially presented by the author in the following conferences:

- “Development, calibration and performance of an electromagnetic mirror based Adaptive Optics system for visual optics” (Oral communication), at the VI International Workshop on Adaptive Optics for Industry and Medicine (Galway, Ireland, 2007);
- “Accommodation Dynamics with Adaptive-Optics-Corrected Ocular Aberrations” (Poster), at ARVO 2008 Annual Meeting (Fort Lauderdale, Florida, USA, 2008);
- “Influence of high order aberrations on accommodation” (Oral communication), at IX Reunión Nacional de Óptica (Ourense, Spain, 2009);
- “Influence of aberrations on the accommodative response” (Invited talk), at the 13th International Myopia Conference (Tübingen, Germany, 2010)

The results here presented were published in a peer review publication:

Gambra, E., Sawides, L., Dorronsoro C., & Marcos, S. (2009). Accommodative lag and fluctuations when optical aberrations are manipulated. *Journal of Vision* 9(6), 1-15.

This chapter addresses the influence of ocular aberrations in the accommodative response, in particular the accommodative lag and fluctuations of accommodation, to accommodative demands ranging from 0 to 6 D. The custom Hartmann-Shack/Adaptive Optics set-up described in Chapter 2 is used to measure dynamically wave aberrations (from which the accommodative response is estimated) under different states of correction/induction of aberrations using an electromagnetic adaptive-optics deformable mirror. Conditions include the correction of ocular aberrations of the unaccommodated state and induction of positive and negative spherical aberration or coma (in amounts consistent to those found in post- refractive surgery or keratoconus patients). Dynamic changes of ocular aberrations and pupil size in the different conditions will be also assessed.

Adaptive optics is an ideal tool to simulate the effect of a potential customized correction and clinical conditions or procedures that induce aberrations on the accommodative response. The results obtained from these simulations may have implications in the understanding of the role of ocular aberrations in the accommodative lag, allowing testing the hypothesis that the presence of aberrations may reduce the accuracy of the accommodative response, particularly at high accommodative demands. The results will provide also further insights into the nature of the fluctuations of accommodation.

## **3.1. Methods**

### **3.1.1. AO set-up**

The adaptive-optics set up has been extensively described in Chapter 2. The primary components of the system are a Hartmann-Shack wavefront sensor (HASO 32 OEM, Imagine Eyes) and an electromagnetic deformable mirror (MIRAO, Imagine Eyes). Illumination arises from a Super Luminescent Diode emitting at 827 nm. The system counts with a Badal optometer mounted on a motorized stage (VXM-1, Velmex) which is used both for compensating for spherical refractive error, and for inducing accommodative demands. A cold mirror behind the wavefront sensor allows inserting the accommodation stimulus, a black and white Maltese cross with eight arms in the deformable mirror path. A pupil monitoring channel, consisting of a CCD camera (TELI, Toshiba), is inserted in the system by means of a plate beam-splitter. Subjects are stabilized by means of a bite bar and aligned to the system (using an x-y-z stage) using the line of sight as a reference.

Residual aberrations of the system were calculated by using an artificial eye composed of an achromatic lens and a diffuser acting as a retina. A closed-loop correction was performed to assess the mirror state that compensated for these residual aberrations and used to correct the aberrations of the optical system.

A custom-built software programmed in VisualC++.Net 2005 (Microsoft) was specifically developed to control the Hartmann-Shack, the deformable mirror (by means of a Software Development Kit from Imagine Eyes) and the motorized Badal system. This software allowed us to move the motor both manually and automatically, capture Hartmann-Shack images, and drive the deformable mirror, correcting or inducing different pattern of aberrations. Besides, software programmed in VisualBasic.Net 2005 (Microsoft) was used to continuously monitor the pupil.

### 3.1.2. Experimental protocol

Ocular aberrations were measured dynamically at a rate of 12.8 Hz for different accommodative stimuli, ranging from 0 to 6 D. The stimulus followed a staircase function (Figure 3.1) in 1-D steps, and was produced by means of the motorized Badal optometer. Each step lasted 5 seconds. Around 65 Hartmann-Shack images were captured in each step. Between steps, the Badal optometer moved during 0.78 sec with a speed of 10 mm/sec (1.28 D/sec). The entire sequence lasted 40 seconds and was typically repeated 5 times for statistical purposes.

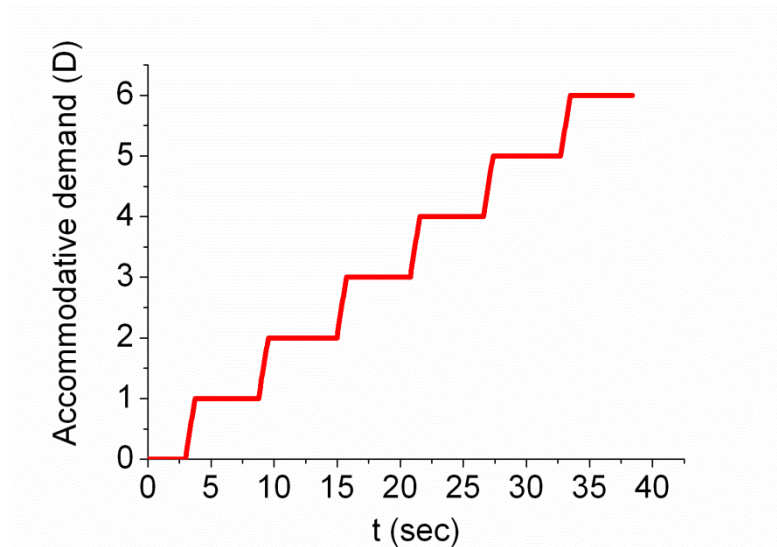


Figure 3.1. Staircase function followed by the accommodation test. Accommodation demand is increased at 1-D increments. Each accommodative step lasted 5 seconds, and the total duration of the test was 40 seconds.

The experiment was performed under different states of the deformable mirror. Five different conditions were studied:

- 1) The subject viewed the target under his/her **natural aberrations** (*Nat*). In this case the mirror only compensated for the residual aberrations of the system.
- 2) The subject viewed the target under **corrected aberrations** (*Corr*). In this case the mirror state compensated for the subject's aberrations in the unaccommodated state. Best AO-correction was found in a closed-loop mode immediately before the measurement.
- 3) The subject viewed the target with **1  $\mu\text{m}$  of positive spherical aberration** induced by the mirror (for 6-mm pupil), and added to his/her natural aberrations (*PSph*).
- 4) The subject viewed the target with **1  $\mu\text{m}$  of negative spherical aberration** induced by the mirror (for 6-mm pupil), and added to his/her natural aberrations (*NSph*).
- 5) The subject viewed the target with **-2  $\mu\text{m}$  of vertical coma** (for 6-mm pupil), added to his/her natural aberrations (*Coma*). The residual aberrations of the system were corrected in all cases.

The induced aberrations and their amounts were not arbitrary chosen: spherical aberration is a symmetric aberration that changes systematically during accommodation, and previous studies have reported induction of similar amounts of aberration after myopic [Marcos et al., 2001] or hyperopic [Llorente et al., 2004b] LASIK. On the other

hand, similar amounts of coma have been reported in keratoconic eyes [Barbero et al., 2002]. Mirror states inducing aberrations were actually achieved for a 7-mm pupil, but aiming at the desired amount of aberrations for a 6-mm pupil. The absolute values of induced aberrations change across experiment due to pupillary miosis. The aberrations imposed on the mirror affected the quality of the image of the accommodative stimulus and the aberrations measured by the Hartmann-Shack system, allowing possible interactions between defocus and high order aberrations.

Subjects were aligned to the system by centering the pupil to the optical axis of the system (using the pupil's camera) while fixating at the Maltese cross. Best refractive correction was subjectively achieved by each subject by moving the Badal optometer in 0.125-D steps, and it was independently obtained for each of the five experimental conditions. Objective refraction was measured immediately before the experiment using a commercial auto-refractometer (Humphrey, Zeiss), and the correction was initially set more hyperopic in the Badal system to avoid the subject accommodating while searching the best focus. Subjects were familiarized with the set up and procedure by performing some preliminary experimental sequences. All the conditions were measured consecutively in the same session. Each condition was repeated five consecutive times.

AO closed-loop correction was performed using our custom-developed software. Final and initial RMS wavefront error values were compared and a correction of at least 80% (astigmatism plus high order aberrations) was required to deem the mirror state appropriate for measurements.

As pupil size decreased with accommodation, we made sure that AO-correction/induction of aberrations was achieved for the largest pupil size (unaccommodated state). Therefore, correction/induction should not be affected by pupil change (if constriction happens concentrically). The Hartmann-Shack images were used to calculate the pupil size during the experiment, with a precision of 0.11 mm.

### **3.1.3. Subjects**

Five young subjects (age:  $25.3 \pm 2.4$ ) with low amounts of spherical error ( $0.35 \pm 0.72$ D) and astigmatism ( $< 0.5$ D) participated in this study. Two of them were trained subjects and the other three were naïve. All of them were capable of accommodating 6 D, as assessed with IR dynamic retinoscopy (PowerRef II, Plusoptix) prior to the experiment. LR was unable to perform the experiment under coma condition. Due to an error, JP performed the coma condition with a horizontal coma instead of the pretended vertical. Subjects signed a consent form approved by the Institutional Review Boards after they had been informed on the nature of the study and possible consequences. All protocols met the tenets of the Declaration of Helsinki.

### **3.1.4. Data analysis**

#### **3.1.4.1. Aberrations**

Wave aberrations were fitted to 7th order polynomials (with criteria following the OSA standards) using a least-mean square procedure. Sequences of Zernike polynomials, along with the corresponding pupil diameter and the pupil center coordinates were analyzed. Typical 40-second sequences of data contained 482 wave aberrations measurements, and were processed using routines written in Matlab (version 7.3; The Mathworks Inc.). Measurements affected by blinks were automatically removed by the

software (as no signal was detected in the Hartmann-Shack and or the pupil size was dramatically affected by the blink), while data captured immediately before and after were supervised and excluded if necessary. We used as a criterion that pupil size and centration should not change significantly from the data previous to the blink. Removed data were replaced by a linear interpolation between the previous and next valid data points. Each accommodative step contained on average  $51 \pm 12$  (between 18 and 65) useful measurements. Zernike coefficients were fitted to individual measurements (to assess dynamic changes in aberrations and accommodative response). Accommodative response was calculated for each measurement and then averaged to estimate its mean value at each accommodative demand. Similarly, pupil diameter at each accommodative demand was obtained as the average of individual measurements. The results of five repeated sequences were eventually averaged to achieve the final data for each condition and accommodative demand.

Unless otherwise noted, results are presented for the natural pupil (which varied dynamically). In some cases, Zernike coefficients were resized to the same pupil size (generally a 4-mm pupil). Besides, the spherical aberration coefficient is sometimes reported in terms of diopters by considering its contribution to the accommodative response according to the following expression:

$$SE(D) = \frac{12\sqrt{5} \cdot C_4^0}{R^2}, \quad \text{Equation 3.1}$$

### 3.1.4.2. Accommodative response

We estimated the accommodative response from wave aberrations, using a definition for spherical equivalent error, based on the paraxial curvature matching of the wavefront aberration map [Thibos et al., 2004]. Therefore, the residual refractive error (M) for each accommodative demand was:

$$M = \frac{-4\sqrt{3} \cdot C_2^0 + 12\sqrt{5} \cdot C_4^0 - 24\sqrt{7} \cdot C_6^0}{R^2}, \quad \text{Equation 3.2}$$

For comparative purposes, we also used as a definition of spherical error the defocus that optimizes the volume under the MTF. This definition (or an alternative that uses Strehl ratio) has been shown to provide the best prediction of subjective refractive error in previous works [Guirao and Williams, 2003; Marcos et al., 2008], and takes into account interactive effects between different Zernike terms as well as diffraction. We used the absolute volume under the MTF, rather than normalized (Strehl ratio) to allow comparisons across accommodation states (with different pupil sizes). The volume under the MTF was truncated at 100 c/deg, as higher frequencies are not relevant to the visual system [Marcos et al., 1999a].

The accommodative response was estimated as the corresponding accommodative demand minus the residual refractive error. Residual refractive error was assumed to be zero at 1.5 D of accommodative demand [He et al., 2000; Plainis et al., 2005] which has been found to be the average accommodative resting state [Leibowitz and Owens, 1975,

1978; Maddock et al., 1981; Smith, 1983; Wolfe and Connell, 1987]. Therefore, the estimated accommodative responses are shifted so that the average response at 1.5 D of accommodative demand is 1.5 D. The refractive correction for the unaccommodated state agreed well with previously measured refraction (autorefractometer) and the residual defocus computed from the Zernike term was consistent with the longitudinal chromatic aberration between the visible wavelength of the target and IR light of the test source [Llorente et al., 2003]. For each accommodative demand, the average accommodative response was calculated by averaging the estimated individual response during each period of 5 seconds. The average accommodative response for each trial was then averaged across the five trials. The accommodative lag is defined as the difference between accommodative demand and accommodative response. Thus, lag is directly the residual refractive error.

### **3.1.4.3. Fluctuations of accommodation**

The fluctuations of the accommodative response were estimated as the standard deviation of the latter during sustained accommodation. These were computed for each accommodative demand (5-second periods) and AO-aberration correction/induction conditions.

Alternatively, we obtained the frequency spectra for each of the 5-second sequences (for the different accommodative demands and AO-correction condition), using Fourier analysis. The area under the frequency spectra was numerically calculated for low (0–0.6 Hz) and high (0.9–2.5 Hz) frequency regions, and compared across conditions.

### **3.1.4.4. Control experiments**

In Chapter 2, we had presented calibrations of the system, including accuracy of wave aberration measurements on artificial eyes with known high order aberrations and capabilities and stability of the AO-system. We also showed the linearity of the Badal system by simulating an accommodation experiment on an artificial eye (in similar steps as for the experiments in real eye) and compensating the induced defocus with trial lenses. Pupil size measured with the Hartmann-Shack was independent of the Badal position. Most Zernike coefficients varied less than 0.02  $\mu\text{m}$  (for 4-mm pupils) with simulated accommodation, although some specific terms -mainly  $C_2^{-2}$ - changed systematically. These calibrations were considered to discount the effects of the instrument on the eye's measurements.

For this study, we also performed a series of control experiments aimed at testing accuracy of induced aberrations (particularly, as we were inducing large amounts of spherical aberration and coma). These tests showed that the error of generated values of spherical aberration and coma was always below 1%. This accuracy is in accordance with expected performance of the deformable mirror [Fernández et al., 2006].

## **3.2. Results**

### **3.2.1. Aberrations correction and induction**

Figure 3.2 shows examples of wave aberration maps in the unaccommodated state for the five experimental conditions (natural, corrected, induced positive and negative spherical aberration and induced coma) for all subjects. Each map has been plotted for the corresponding natural pupil diameter (between 4.7 and 6.8 mm). Figure 3.3 shows

the amount of spherical aberration, 3rd order RMS and total higher order RMS in each of the wave aberration maps in Figure 3, for the natural pupil. Table 3.1 shows the average amount of high order RMS in the natural and AO-corrected condition (across all measurements of the unaccommodated state), and a 4-mm pupil.

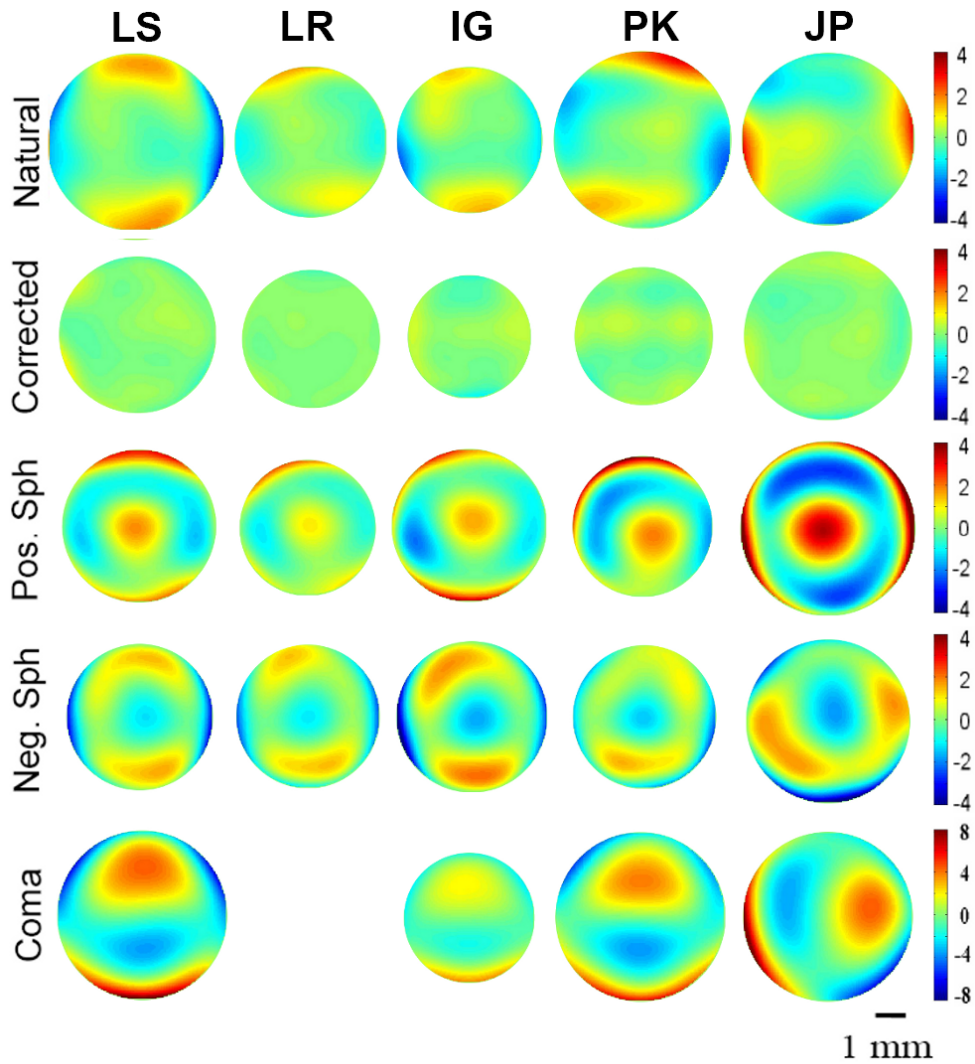


Figure 3.2. Examples of wave aberration maps - 3<sup>rd</sup> order and higher - for each subject and condition, in the unaccommodated state and for their corresponding natural pupils. LR was unable to perform the coma condition, while JP performed it with horizontal coma due to an error

Subject	RMS ( $\mu\text{m}$ )	
	Natural	AO-Corrected
LS	0.138	0.075
LR	0.107	0.050
IG	0.202	0.097
PK	0.169	0.151
JP	0.120	0.058
<b>Average</b>	<b>0.147</b>	<b>0.086</b>

Table 3.1. Natural and AO-corrected RMS wavefront error (for high order aberrations). Pupil diameter = 4mm.

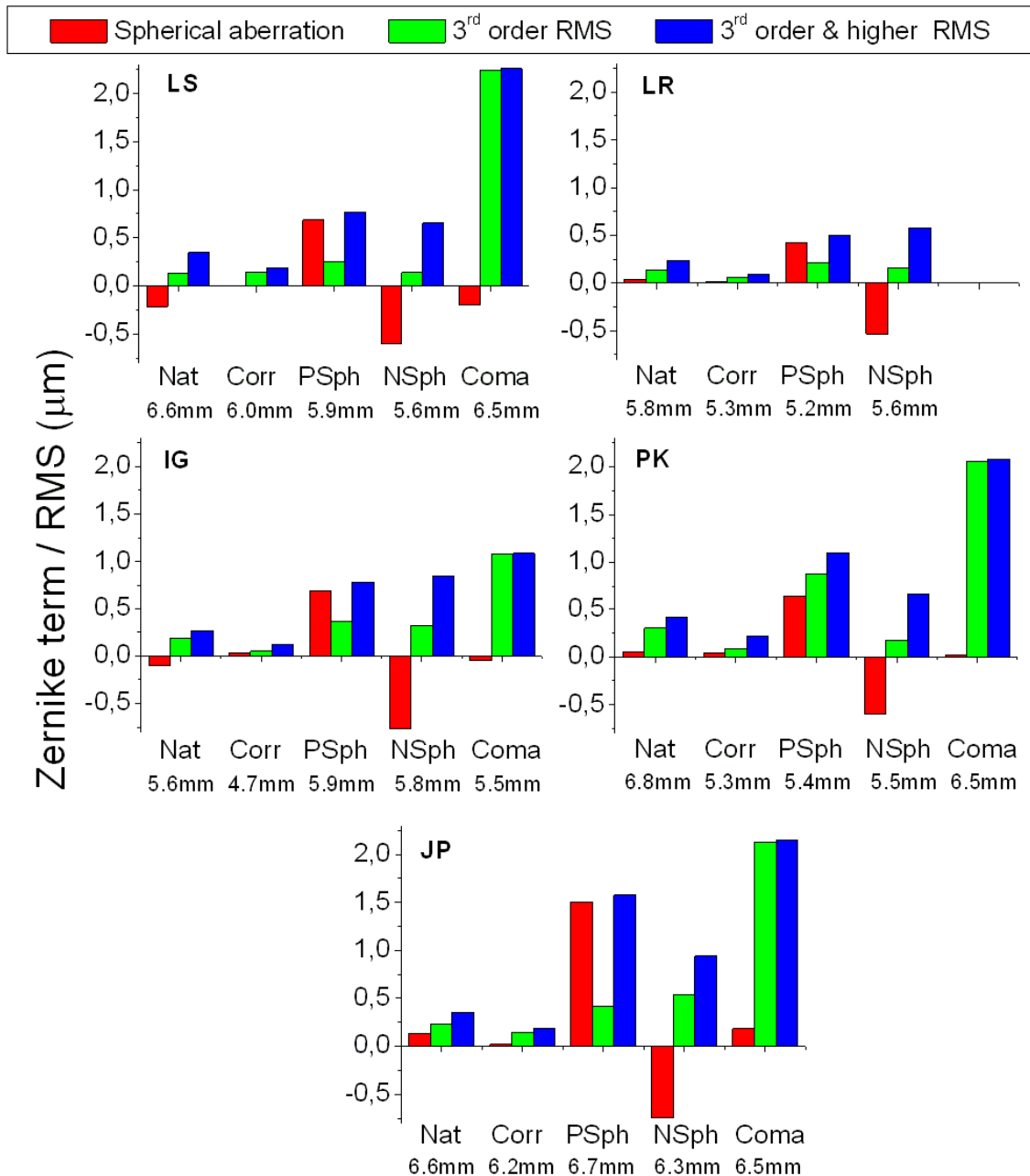


Figure 3.3. Contribution of different Zernike terms to the wave aberration maps in Figure 3: Spherical aberration  $C_4^0$  (red), 3<sup>rd</sup> order RMS (green) and total high order RMS (blue). Pupil diameters are indicated under each condition: Natural (Nat), AO-corrected (Corr), induced positive spherical aberration (PSph), negative spherical aberration (NSph) and Coma (Coma).

### 3.2.2. Changes in pupil with accommodation and aberration condition

Changes in pupil diameter with accommodation play a role in the relative change of aberrations with accommodation and the accommodative response. Figure 3.4A shows the pupil diameter change with accommodative response for the different experimental conditions (averaged across subjects). There is a systematic decrease of pupil diameter with accommodation, as expected [Schaeffel et al., 1993; Kasthurirangan and Glasser, 2005]. The rate of change in pupil diameter differs across subjects. Also, several subjects showed different pupil diameter change rates across conditions. Figure 3.4B-C shows examples for two subjects. LS showed differences in pupil diameter across

conditions, while for LR the pupil diameter was nearly independent of the aberration condition.

Linear regressions to the data of Figure 3.4A show a highly linear pupil diameter change with accommodation. The average slope of the change ranged from  $-0.23$  mm/D (for induced negative spherical aberration) to  $-0.6$  mm/D (for induced positive spherical aberration). On average, the pupil diameter was significantly smaller than in the rest of conditions when the aberrations were corrected, and (for the highest accommodative demands) also when positive spherical aberration was induced (ANOVA, Bonferroni T2, with SPSS 15.0 for Windows).

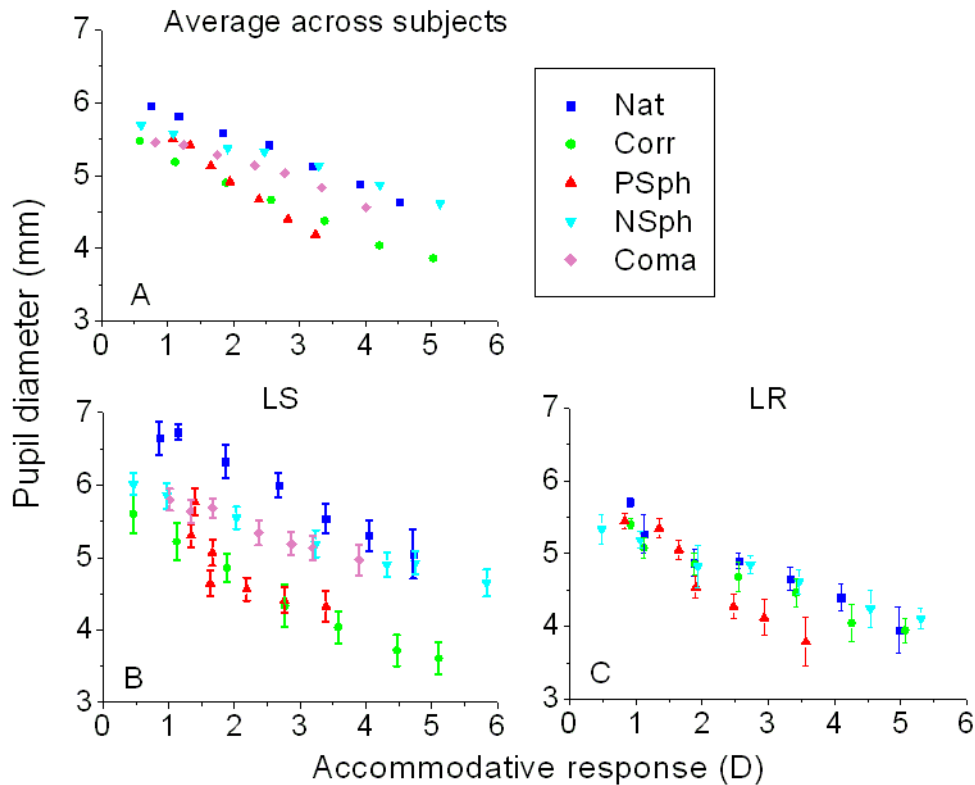


Figure 3.4. A: Change of the pupil diameter vs. accommodative response, for all tested conditions. A: Averaged data across subjects; B: Individual data (averaged across repeated measurements) for subject LS; C: Individual data (averaged across repeated measurements) for subject LR. These two subjects show very different condition-dependent pupil diameters.

### 3.2.3. Change of aberrations with accommodation

Figure 3.5 shows an example (subject LR) of the change of aberrations (astigmatism  $Z_2^{+2}$  and  $Z_2^{-2}$ ; coma  $Z_3^{+1}$  and  $Z_3^{-1}$  and spherical aberration) with accommodative response, with natural aberrations (A), AO-correction (B), induced positive (C) and induced negative (D) spherical aberration. Results are shown for natural pupil diameters.

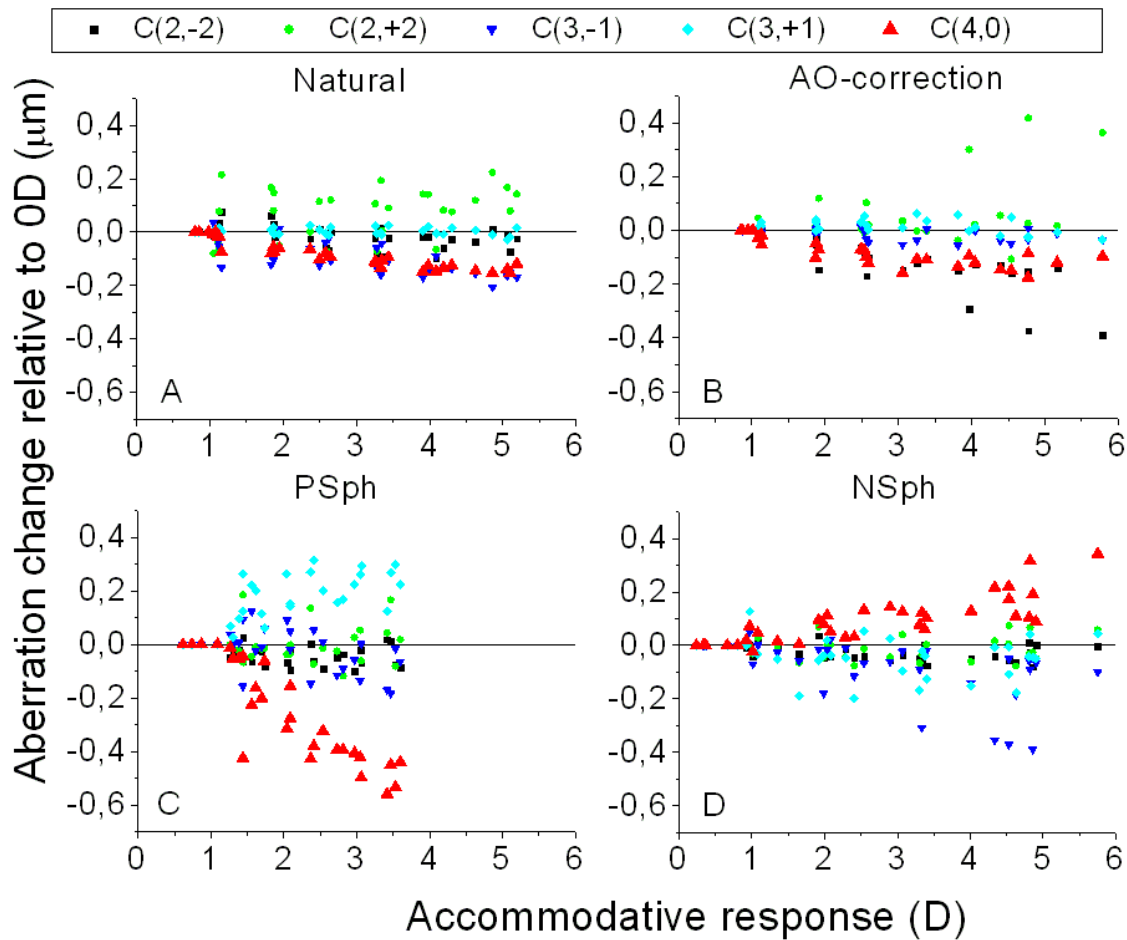


Figure 3.5. Change of different individual Zernike terms ( $C_2^{-2}$ ,  $C_2^{+2}$ ,  $C_3^{-1}$ ,  $C_3^{+1}$  and  $C_4^0$ ) with accommodative response for different conditions (A: natural; B: AO-corrected; C induced positive spherical aberration; and D: induced negative spherical aberration). Data are for subject LR with natural pupil.

Table 3.2 shows the slopes from regression lines to data from all subjects. As expected, the term that varied the most was the spherical aberration, which shifts toward more negative values with accommodation. Interestingly, the condition under test influenced significantly the rate of variation of spherical aberration with accommodation. In all subjects, the measured spherical aberration (corresponding to the eye plus the mirror) changed more rapidly toward negative values when positive spherical aberration was induced by the deformable mirror, whereas the slope of this change was greatly reduced when negative spherical aberration was induced. The tendency was the same (not shown) when spherical aberration was plotted against the accommodative demand (which was independent of the actual change in spherical aberration). It is expected that for the same accommodative response, the accommodation-related physical changes of the crystalline lens -and therefore the relative change of the ocular spherical aberration- are similar, regardless the experimental condition (or overall degradation) of the target.

Condition	Subject	slope ( $\mu\text{m/D}$ )		
		C(2,-2)	C(3,1)	C(4,0)
Nat	LS	-0.027*	-0.011	0.023
	LR	-0.013*	-0.002	-0.034*
	IG	0.012*	-0.007*	-0.012
	PK	-0.063*	0.018*	-0.028*
	JP	0.008	-0.056*	-0.013*
	Avg	-0.017	-0.012	-0.013*
Corr	LS	4x10 <sup>-5</sup>	6x10 <sup>-5</sup>	-0.021
	LR	-0.058*	-0.003	-0.028*
	IG	-0.012*	0.002	-0.030*
	PK	0.012*	0.003	-0.016*
	JP	0.004	-0.002	-0.014*
	Avg	-0.011	1x10 <sup>-5</sup>	-0.022*
PSph	LS	0.009	0.052*	-0.157*
	LR	-0.013	0.081*	-0.190*
	IG	0.014*	0.044*	-0.065*
	PK	-0.051	0.044	-0.117*
	JP	0.029*	-0.009	-0.505*
	Avg	-0.002	0.042*	-0.207*
NSph	LS	0.006	-0.044*	0.078*
	LR	-0.005	-0.010	0.045*
	IG	-0.001	-0.049*	0.039*
	PK	-0.041*	0.033	0.084*
	JP	0.005	-0.093*	0.042*
	Avg	-0.007*	-0.033*	0.058*
Coma	LS	-0.082*	-0.026*	-0.044*
	IG	-0.010	-0.002	-0.005
	PK	-0.079*	0.006	-0.033*
	JP	-0.205	0.205*	-0.127*
	Avg	-0.094*	0.046	-0.052*

Table 3.2. Slope of the regressions of  $C_2^{-2}$ ,  $C_4^0$  and  $C_3^{-1}$  (in microns) vs. accommodative response for each subject and condition. \*There is a significant dependence with accommodative response (Z-test).

We explored the causes for the relative differences in the rate of change of spherical aberration across conditions shown in Figure 3.5. Figure 3.6 shows the isolated ocular contribution to the measured change of spherical aberration with ocular accommodative effort for natural and positive and negative spherical aberration induced conditions. The ocular contribution to the accommodative response (ocular effort) has been calculated

by resizing all wavefronts to a 4-mm pupil, what eliminates the influence of pupil constriction on spherical aberration change. Besides, Zernike coefficients of the resized pupils have been used to assess ocular accommodative effort, using Equation 3.2. Figure 3.6 shows average data across four subjects (PK was not included as his pupil was smaller than 4-mm for the highest accommodative demands).

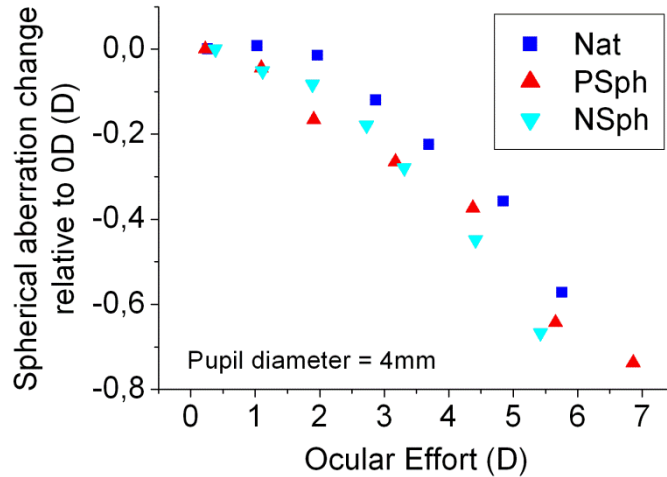


Figure 3.6. Ocular contribution to the change of spherical aberration term versus ocular effort (defined as the ocular contribution to the accommodative response, discounting the mirror contribution) and is obtained from Zernike coefficients of 4-mm resized pupil using equation 2. Data are average across LS, LR, IG and JP subjects and for 4-mm resized pupils.

The rate of change for the three conditions (natural and induced positive/negative spherical aberration) is much more similar (Figure 3.6), as expected, and primarily driven by the structure-related changes in spherical aberration of the crystalline lens with accommodation.

The different change rates of spherical aberration shown in Figure 3.5 are therefore mainly indicative of a pupil-dependent contribution of the induced/corrected spherical aberration, which varies across accommodative responses and conditions. When positive spherical aberration is induced, its effective positive contribution relatively decreases as the pupil decreases with accommodation. The result is a change of measured spherical aberration shifted to more negative values, i.e. the effect is added to the effect of the crystalline lens. On the other hand, if negative spherical aberration is induced, its effective negative contribution relatively decreases as the pupil decreases with accommodation counteracting the change in spherical aberration of the crystalline lens, and the slope becoming closer to zero.

We also evaluated the dynamic change of other aberrations (astigmatism and 3rd order Zernike terms) as a function of the accommodative response for the conditions under test (see Figure 3.5 for graphical example on subject LR, and Table 3.2 for regression line fits to data from all subjects). We did not find a general tendency across subjects, neither in the natural or aberration corrected/induced conditions. Although the change in certain Zernike terms with accommodation is significant in some individual subjects, it usually does not occur in all measured conditions (less frequently in the natural conditions), and slope for the change is generally small.

### 3.2.4. Influence of aberrations on the accommodative response

Figure 3.7 shows examples of the accommodative response for subject LS under the five conditions under test (natural aberrations, corrected aberrations, induced positive spherical aberration, induced negative spherical aberration and induced coma). The data are for a single measurement, and are representative of typical responses in this group of subjects. One of the subjects (LR) was unable to perform the task under induced coma. The accommodative response (and from it, the accommodative lag) was estimated from the residual spherical error (Equation 3.2).

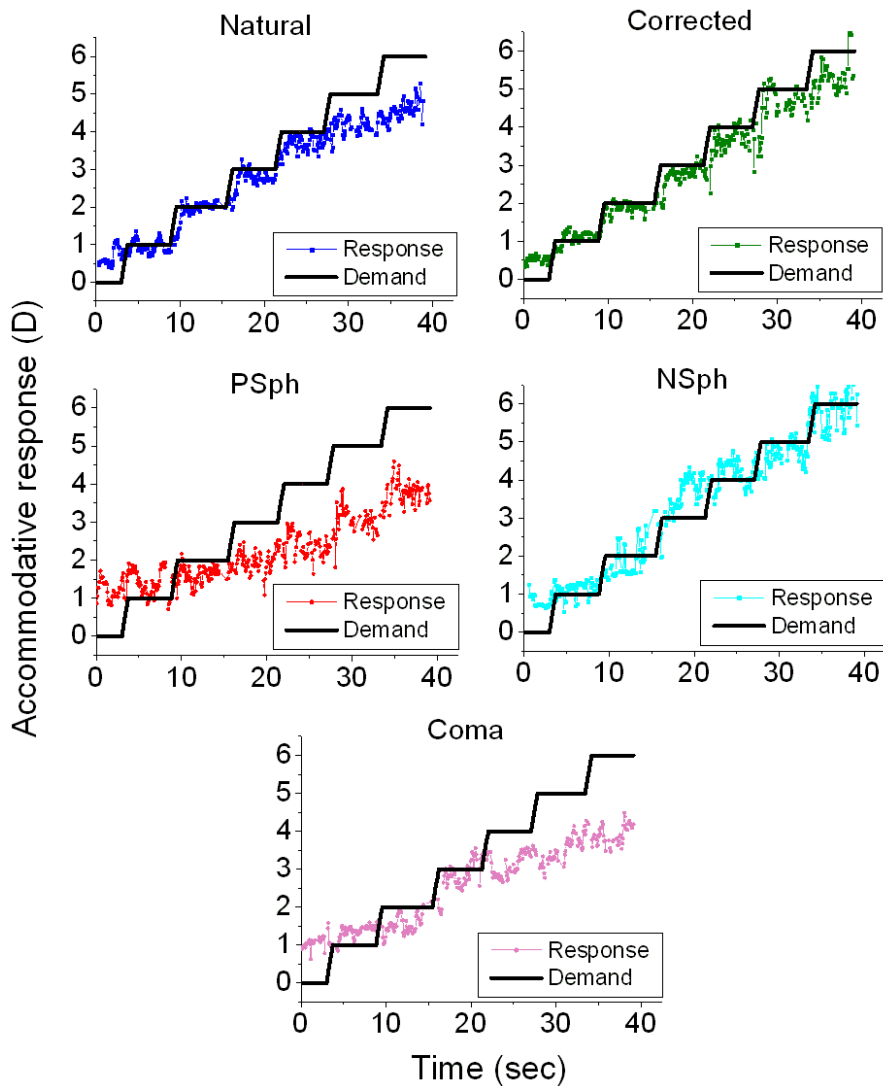


Figure 3.7. Examples of accommodative responses for subject LS for the different aberration conditions. Data are for a typical measurement run.

Figure 3.8A-E shows the accommodative lag, averaged across measurements (5 runs) and 5-second steps as a function of the accommodative demand. Data are for all five subjects and conditions. Most subjects showed a better accommodative response (lower lag) with corrected than with their natural conditions (4 out of 5 subjects). The induction of negative spherical aberration resulted also in a better accommodative response for the same 4 subjects. On the other hand, the accommodative response is poorer in all the cases when positive spherical aberration and vertical coma were induced. Only one subject (IG) showed best accommodative response under natural aberrations.

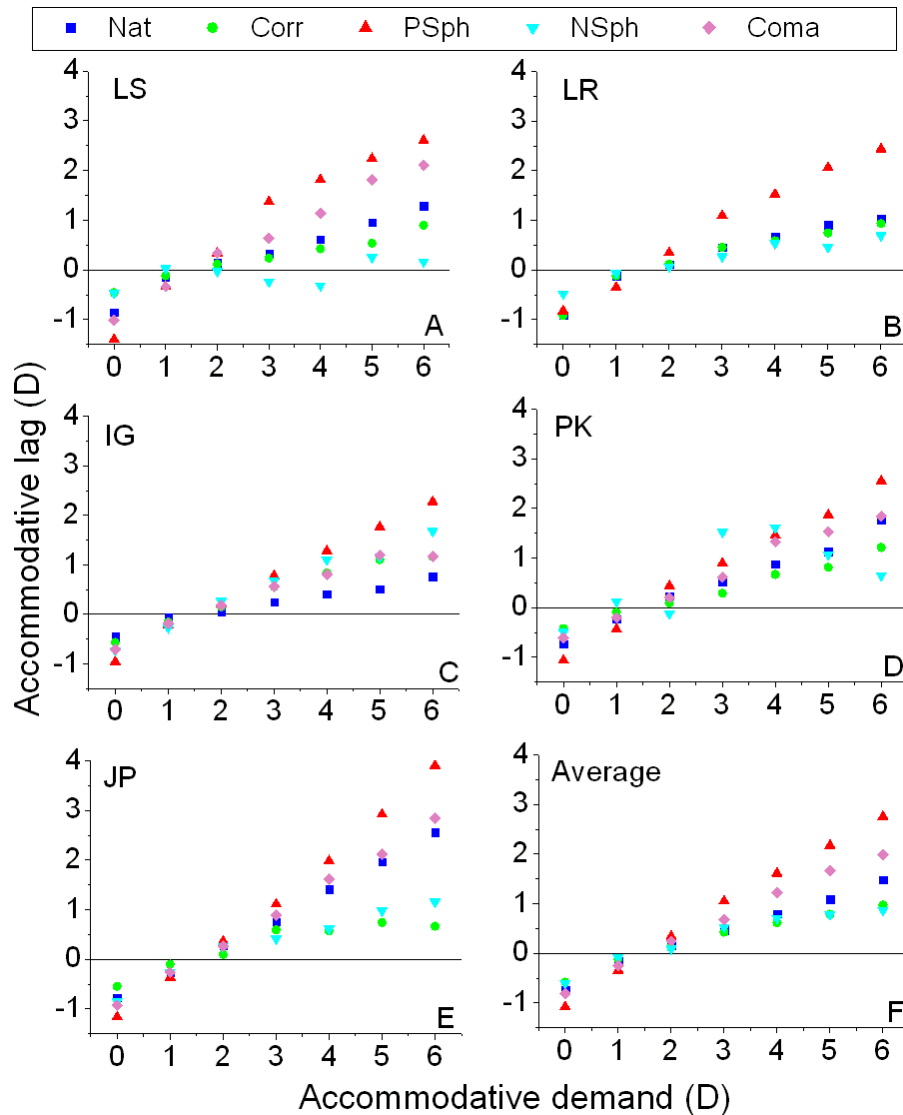


Figure 3.8. Accommodative lag for all subjects (A-E) and averaged across subjects (F) for all conditions, Positive lag means under-accommodation (lag) while negative lag means over-accommodation (lead). Each point has been calculated by averaging responses in each accommodative demand, and from five repeated measurements.

Figure 3.8F shows the accommodative lag averaged across subjects. On average, lag with AO-corrected aberrations and with induced negative spherical aberration were significantly different from lag with coma ( $p < 0.05$ ) for high accommodative demands. Differences between lag for induced positive spherical aberration and all other conditions (except coma) were statistically significant (ANOVA, Bonferroni T2, with SPSS 15.0 for Windows). These general tendencies were followed by three of the individual subjects (LS, LR and JP). The other two showed significant differences for a few accommodative demands and conditions.

Alternatively, residual error (and accommodative lag) was computed from the defocus that optimized the volume under the MTF. Figure 3.9 shows through-focus optical quality (in terms of volume under the MTF) for the different accommodative demands and four conditions (A: natural; B: AO-corrected; C: induced positive spherical aberration; D: induced negative spherical aberration), for subject LR. The MTFs were estimated from a series of Zernike coefficients (averaged for each accommodative

demand). According to this definition, the accommodative response is computed from the peaks of the through-focus functions, and the accommodative lag from the shift of the peak of the 6-D through-focus function from 0 D. Correcting the aberrations of the unaccommodated state produces an increase in the peak values and a narrowing of the through-focus functions. Inducing positive spherical aberration produces an enhancement of the through-focus functions for the highest accommodative demands as well as an increase in the accommodative lag. Inducing negative spherical aberration broadens the curves for all accommodative demands and reduces the accommodative lag (which, for this particular subject and condition results in a negative value). We have compared the accommodative response and accommodative lag obtained from the volume under the MTF through-focus function and from other spherical error definitions. We found a better agreement between the volume under the MTF and the paraxial curvature metric, considering up to 6<sup>th</sup> order spherical aberration in the equation (standard deviation of the difference in accommodative lag across metrics: SD = 0.27 D). However, when the spherical error was estimated considering the Zernike defocus term only, the accommodative response was properly described for natural and AO-corrected conditions, but failed for the conditions in which spherical aberration was induced (SD = 0.50 D). Considering only defocus and 4th spherical aberration in the definition of residual spherical error tended to over-estimate the accommodative response (SD = 0.86 D) with respect to the paraxial definition that includes terms up to the 6<sup>th</sup> order.

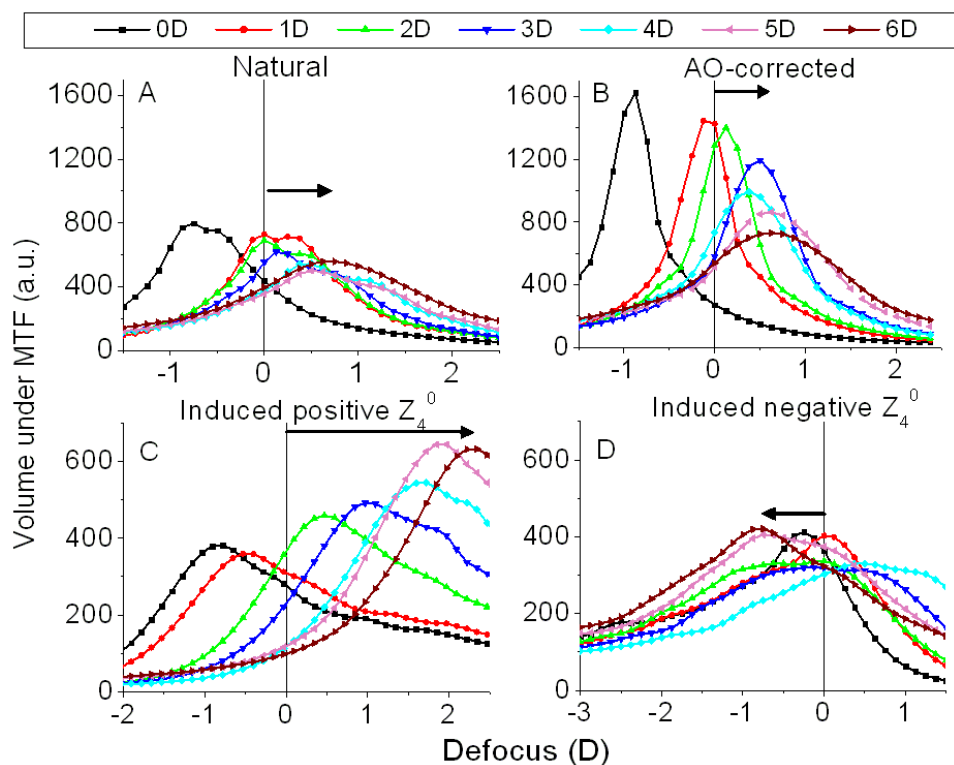


Figure 3.9. Through-focus volume under the MTF (as an optical quality metric), for the different accommodative demands and different conditions (A: natural aberrations; B: AO-corrected aberrations of the unaccommodated state; C: induced positive spherical aberration; D: induced negative spherical aberration), for subject LR. The defocus shift that produces a maximum in the through-focus function represents the accommodative lead (for the lower accommodative demands) and the accommodative lag (for the higher accommodative demands). The arrow represents the accommodative lag for a 6-D stimulus. The amplitude and width of the through focus functions, as well as the accommodative lag, change across conditions.

### 3.2.5. Influence of demand and aberrations on the fluctuations of accommodation

Figure 3.10 shows the fluctuations of accommodation (standard deviation of the accommodative response) as a function of accommodative demand, for all conditions tested, and averaged across subjects. We found that fluctuations increased systematically with accommodation in all conditions (with slopes ranging from 0.033 when positive spherical aberration was induced to 0.077 when coma was induced). For a given accommodative demand, fluctuations tend to be lowest under natural and corrected aberrations, and highest under induced spherical aberration (particularly negative) and induced coma. Fluctuations were significantly higher ( $p < 0.05$ ) than for natural aberrations when negative spherical aberration was induced (ANOVA, Bonferroni T2, with SPSS 15.0 for Windows). The induced positive spherical aberration condition also produced significantly higher fluctuations for the lowest accommodative demands.

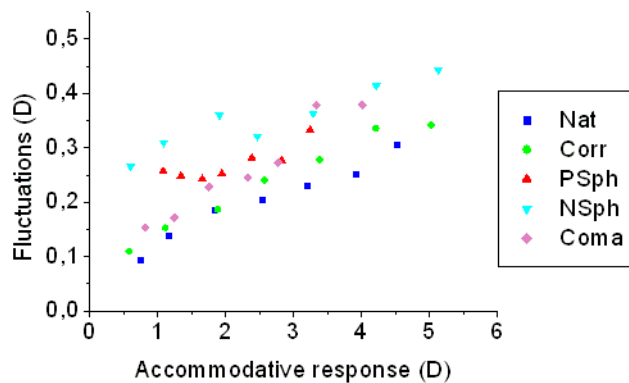


Figure 3.10. Fluctuations of accommodation (estimated as the standard deviation of the accommodative response) averaged across subjects and conditions.

Alternatively, the area under frequency spectra (up to a frequency of 2.5Hz) was also used to define the fluctuations of accommodation. We found a good correlation (slope= $0.78 \pm 0.03$ ,  $R=0.94$ ,  $p < 0.0001$ ) between the fluctuations estimated from the frequency spectra and the standard deviation of the accommodative response. Restricting the area to low frequency range (0–0.6Hz), primarily associated to the fluctuations of the accommodation plant, does not increase the correlation between definitions, while restricting the area to a higher frequency range (0.9–2.5Hz), typically related to cardiac pulse slightly worsened the correlation (slope= $0.34 \pm 0.02$ ,  $R=0.88$ ,  $p < 0.0001$ ).

### 3.3. Discussion

Our results show that the presence or absence of high order aberrations (controlled with adaptive optics) alters the accommodative response and the fluctuations of accommodation. We did not find that correcting high order aberrations had a negative impact on the accommodative response. Moreover, the precision of the accommodation response increases if aberrations are corrected and worsens if some aberrations such as coma (which broadens the depth of focus) are induced. We can conclude from this study that the presence of larger amounts of high order aberrations produces an increase in

accommodative lag. This result is interesting in the understanding of the causes for the accommodative lag in young subjects. It also suggests that the increased accommodative lag found in myopes [Mutti et al., 2006] may be linked to larger amounts of high order aberrations in myopes [Paquin et al., 2002; He et al., 2002, Marcos et al., 2000], and therefore be a consequence rather than a preceding factor in myopia development [Mutti et al., 2006]. Although not all studies have found higher amounts of aberrations in myopes compared to emmetropes or hyperopes [Carkeet et al., 2002; Cheng et al., 2003], there is evidence that this is the case for high myopes. Whether increased amounts of aberrations may trigger myopia development has also been a matter of debate [Collins et al., 1995b; Thorn et al., 2003]. Studies on animal models [García de la Cera et al., 2007] suggest that increased aberrations may be rather a result of the structural properties of myopic eyes, rather than a cause of myopia.

The presence of spherical aberration also influences the accuracy of the accommodative response, with the effect being highly dependent on the sign of the induced spherical aberration. In agreement with a previous observation by Collins et al., [1997] we found that adding negative spherical aberration produced a decrease in the accommodative lag, despite the increase of high order aberrations (and decrease of optical image quality of the unaccommodated state). On the other hand, adding positive spherical aberration produced an increase in the accommodative lag (less accurate accommodative response). These results indicate that the accommodative response may be affected in patients that had undergone corneal refractive procedures that increase high order aberrations, as standard myopic LASIK induces significant amounts of positive spherical aberration [Marcos et al., 2001], and hyperopic LASIK of negative spherical aberration [Llorente et al., 2004b]. The influence of spherical aberration on the accommodative response also reinforces the importance of considering not only defocus but higher order aberrations for the estimation of the accommodative response, as had been emphasized by Plainis et al. [2005], similarly as in the calculation of refractive errors [Thibos et al., 2004, Guirao & Williams, 2003]. To our knowledge, few studies have explored the influence of other high order aberrations on accommodation. López-Gil et al. [2007] found a decrease of dynamic accommodation gain in subjects wearing contact lenses that induced coma and trefoil, which is consistent with the reduced accommodative response that found in the presence of coma.

The change of pupil size diameter with accommodation is also important to account for the relative contribution of the induced/corrected aberrations and the relative change of high order aberrations with accommodation to the accommodative response. We found that in our subjects, pupil size decreased with accommodative response at a rate of  $-0.35$  mm/D (natural condition), within the range of previous studies, i.e. Plainis et al. [2005] ( $-0.18$  mm/D) and Alpern et al. [1961] ( $-0.45$  mm/D). Surprisingly, the pupil diameter varied significantly across conditions in several subjects, and the differences were observed at all accommodative demands. On average across subjects, the pupil was significantly smaller when aberrations were AO-corrected, and largest in the natural condition. Certain subjects (i.e. LS) differed as much as 1.66 mm between conditions, for the same accommodative demand, although for other subjects (i.e. LR) the differences across conditions were not significantly different. The rate of variation in pupil diameter with accommodation also varied across conditions. Pupil size did not vary with the condition tested when artificial eyes were used. We are uncertain on the reasons for this difference which is very significant in some subjects, as the changes in retinal illuminance between the corrected/uncorrected aberrations conditions are expected to be small. An alternative hypothesis is that the presence of unfamiliar

distortion (or correction) in the image has an impact on pupil size. In any case, these differences contribute to the improved accommodative lag under corrected aberrations.

The accommodation-related changes of aberrations with accommodative demand that we found are in good agreement with previous studies. We did not find that correcting/inducing aberrations altered the relative change of aberrations (except for spherical aberration) with accommodation. The reported differences in the change of spherical aberration when the amount of spherical aberration of the unaccommodated state is altered are mainly a consequence of the relative contribution of the aberration induced by the mirror as the pupil decreases with accommodative response. When the ocular (primarily crystalline lens) contribution to the change in spherical aberration is isolated, the change of spherical aberration with accommodation is much more similar across conditions (see Figure 3.6). It should be noted, however, that the actual changes reported in Figure 3.5 (showing drastic differences in the change of spherical aberration under positive or negative spherical aberration) should be truly representative of the accommodation related changes of spherical aberration after standard LASIK, where significant amounts of aberration are induced on the cornea.

Under natural conditions, spherical aberration shifted to more negative values with accommodation response at a rate of  $-0.013 \mu\text{m}/\text{D}$  (averaged across subjects). This rate of change is lower than that reported in earlier studies using a fixed pupil diameter ( $-0.043 \mu\text{m}/\text{D}$  of Cheng et al. [2004] for an artificial pupil of 5-mm; around  $-0.083 \mu\text{m}/\text{D}$  of He et al. [2000] for an effective 6.5-mm pupil, and  $-0.048 \mu\text{m}/\text{D}$  of Plainis et al. [2005] for natural pupils). The differences arise primarily from the change pupil diameter with accommodation in our experiments, which were performed under natural viewing conditions. A comparison of the change of spherical aberration expressed in diopters (equation 1) to minimize the impact of the pupil diameter change gives similar rate of change ( $-0.153 \text{ D}/\text{D}$  in the current study,  $-0.184 \text{ D}/\text{D}$  in Cheng et al. [2004], around  $-0.230 \text{ D}/\text{D}$  in He et al. [2000] and  $-0.170 \text{ D}/\text{D}$  in Plainis et al. [2005]).

Other aberration terms (astigmatism;  $C_2^{-2}$ ,  $C_2^2$ ) or coma, ( $C_3^{-1}$ , and  $C_3^1$ ) did not change systematically with accommodation across subjects, and their averaged slopes were similar to those reported in previous studies [Cheng et al., 2004; He et al., 2000; Plainis et al., 2005].

Fluctuations of accommodation systematically increased with accommodative response. For natural condition, we have obtained that fluctuations varied from 0.09 D to 0.31 D – in the 0–6D-stimulus range– with a slope of 0.049 D/D. This is consistent with previous studies: Plainis et al. (2005) found that fluctuations increased with accommodation from 0.07 D to 0.22 D for an accommodative demand of 8 D; and Kotulak and Schor [1986b] found a slope of 0.047 D/D (plotting fluctuations vs. mean response). However, we did not find a maximum for intermediate demands –as reported by Mieke and Denieul [1988] and Plainis et al. [2005]– either for averaged or for individual data. Furthermore, although differences did not always reach statistical significance, in general fluctuations were greater when spherical aberration and coma were induced and smaller for natural and AO-corrected aberrations. This finding indicates that retinal image quality plays an active role in the fluctuations of the accommodative response, likely due to the increased depth-of-focus when aberrations are increased [Marcos et al., 1999b; Cheng et al., 2003].

Calculation of the accommodative response with all the Zernike coefficients in Equation 3.2 has been shown to be more accurate when compared with an alternative metric

based on the volume under the MTF. Similar results have been found by Aldaba et al. [2012].

### **3.4. Open question**

In this chapter we have explored the role of high order aberrations on the accommodation accuracy. Using Adaptive Optics, we have seen that the presence of high order aberrations is detrimental for the accommodation accuracy, except when a negative value of spherical aberration was induced. This reduction of the accommodative response can be either due to a higher tolerance to HOA-blur, or to the interaction between HOA and accommodation-related defocus. The next chapter will address this question by investigating how blur induced by HOA on simulated targets influences dynamic accommodation.

## **4. DYNAMIC ACCOMMODATION WITH SIMULATED TARGETS BLURRED WITH HIGH ORDER ABERRATIONS**

This chapter presents a study that investigates the impact of high order aberration on the accommodation process using stimuli blurred with HOA. The experimental part of this work was performed during a 2-months stay at the College of Optometry of the State University of New York, under the supervision of Professor Philip B. Kruger.

The author designed the study and the experimental protocols in collaboration with Susana Marcos and Philip B. Kruger, collected and processed the data.

Results were presented by the author in the following conferences:

- “Dynamic accommodation with high order aberrations blurred simulated targets” (Oral communication), at ARVO 2009 Annual Meeting (Fort Lauderdale, Florida, USA, 2009);
- “Influence of high order aberrations on accommodation” (Oral communication), at IX Reunión Nacional de Óptica (Ourense, Spain, 2009);
- “Influence of aberrations on the accommodative response” (Invited talk), at the 13th International Myopia Conference (Tübingen, Germany, 2010)

These results have been published in a peer review publication:

Gambra, E., Wang, Y., Yuan, J., Kruger, P. B., & Marcos, S. (2010). Dynamic accommodation with simulated targets blurred with high order aberrations. *Vision research*, 50(19), 1922-1927.

In the previous chapter, a custom-developed Adaptive Optics system was used to measure the accommodative response (to accommodative demands increasing from 0 to 6D following a staircase function) in young subjects to corrected or induced aberrations. We found that the absence of high order aberrations made the accommodative response more accurate (less accommodative lag to higher accommodative demands), while inducing HOA such as  $-2\mu\text{m}$  of vertical coma for 6-mm pupil decreased the accommodative response (i.e. increased the accommodative lag).

The interactions of the accommodation-induced spherical aberration [He et al., 2000] and change of pupil diameter [Kasthurirangan and Glasser, 2005] produce differences in the response to positive (increased lag) or negative (decreased lag) spherical aberration induced by the deformable mirror, as also reported by Theagarayan et al. [2009] using contact lenses to induce spherical aberration. The observed changes in the accommodative response when aberrations are induced (or corrected) may result from changes in the wavefront vergence, due to optical interaction between the induced aberrations and the subject's own aberrations.

Alternatively, the decreased response with induced aberrations (and more accurate response with corrected aberrations) may result from the higher tolerance to blur in the presence of HOA [Marcos et al., 1999b].

While the use Adaptive Optics or contact lenses inducing aberrations does not allow us to distinguish between the two alternatives, we can eliminate the interaction between aberrations by imposing blur directly on the stimulus and investigate to which extent blur induced by HOA on these simulated targets influences dynamic accommodation.

## **4.1. Methods**

### **4.1.1. Dynamic accommodation system**

The set up used in this study has been previously described in Section 2.2. In summary, the vergence of the stimuli presented on a micro-mirror display is dynamically changed by means of a motorized Badal system, while accommodation is continuously monitored (100 Hz) with a high-speed infrared. Besides a pupil diaphragm conjugate to the natural pupil's plane is set to 3-mm in order to reduce the effect of the subject's own aberrations without increasing the depth of focus [Campbell and Gubisch, 1966].

### **4.1.2. Accommodative targets**

The accommodative target was a quasi monochromatic ( $\lambda = 552 \text{ nm}$ , BW 10 nm) Maltese cross of  $20 \text{ cd/m}^2$  subtending  $1^\circ$ . The Maltese cross was blurred with different types -defocus, vertical coma, vertical trefoil and spherical aberration- and amounts (0.3  $\mu\text{m}$  and 1  $\mu\text{m}$ , for a 3-mm pupil) of aberrations by convolving the original target with the Point Spread Function (PSF) corresponding to every aberrated condition (see Figure 4.1). The blurred stimuli were calculated using a custom routine written in Matlab (Mathworks, Natick, MA).

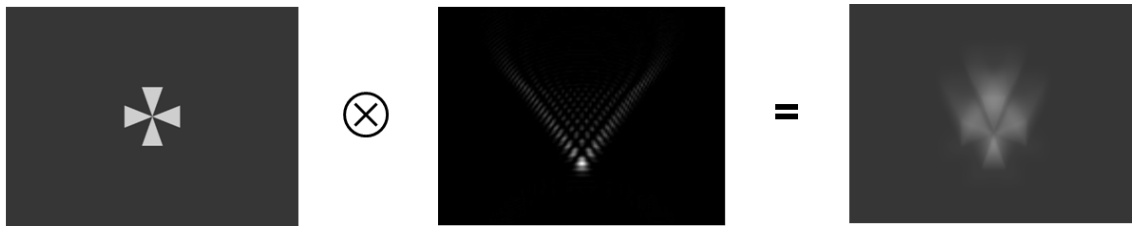


Figure 4.1. The original stimulus is convolved with the PSF corresponding to +1 mm of vertical coma for a 3-mm pupil to obtain the aberrated target

Figure 4.2 shows the nine different conditions that were tested. The video projector was calibrated and the stimulus grayscale was modified in order to take into account the gamma correction of the video projector in the displayed image. The contrast of the original image was reduced to 0.9 in order to work in the linear range of the gamma correction curve.

The nine conditions were randomly repeated six times for every subject.

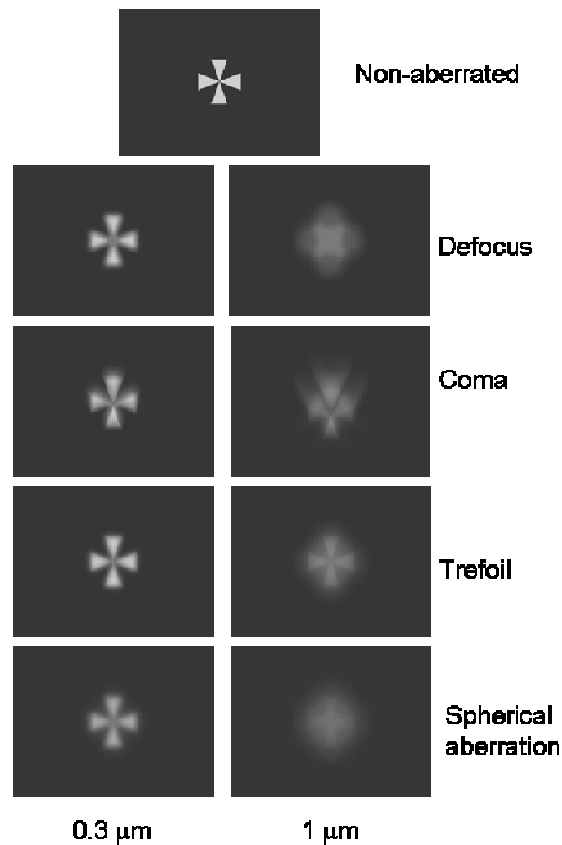


Figure 4.2. Images of the nine targets used in this study. The non-aberrated Maltese cross is convolved with the PSF corresponding to 0.3 μm and 1 μm of defocus, vertical coma, vertical trefoil and spherical aberration (for a pupil of 3 mm).

### 4.1.3. Experimental protocols

During every experimental trial, the subject was positioned in front of the apparatus on a chin and forehead rest, which kept the subject still. The left eye of each subject was tested and the right eye was patched. The stimulus vergence varied sinusoidally from 1D to 3D with a frequency of 0.195 Hz during trials lasting 40.96 s. To minimize the subject's fatigue, the 54 trials were run in four experimental sessions of 1 hour of

duration on different days. If the subject had not followed the stimulus in some of the trials properly, these trials were repeated at the end of the session.

#### **4.1.4. Subjects**

Five young subjects (age:  $26.0 \pm 4.4$ ) participated in the study. The protocols were approved by Institutional Review Boards (IRB) and met the tenets of the Declaration of Helsinki. One subject was an investigator and the rest were unaware of the purpose of the study, although one of them was an experienced subject in accommodation studies. All subjects were visually normal and achieved at least a 20/20 visual acuity. Refractive errors (mean sphere:  $-0.3 \pm 2.0$ , ranging from +1.75 to -3.5D; mean cylinder:  $-0.50 \pm 0.35$ ) were corrected by means of trial lenses or subject's own contact lenses for subject S5 (sphere: -3.5D). Their high order aberrations (3rd order and higher) were measured with a COAS aberrometer (Wavefront Sciences, Albuquerque, New Mexico), resulting in an averaged value of  $0.15 \pm 0.06 \mu\text{m}$ , ( $0.26 \mu\text{m}$  for subject S2 and the rest ranging from 0.11 to  $0.14 \mu\text{m}$ ) for a 3-mm pupil.

Another six subjects were discarded because they did not follow the stimulus properly or their accommodative gain was lower than 0.2 for the non-blurred condition.

#### **4.1.5. Data processing**

Data were collected and analyzed using custom software. Blinks were removed manually from each accommodation trial before analysis and replaced with a linear interpolation between the pre- and post-blink values. Trials with more than 14.65% blinks were discarded [Kruger et al., 2004]. Temporal responses were processed using a fast Fourier transform to extract dynamic gain and temporal phase lag at the stimulus frequency (0.195 Hz). To reduce spectral leakage in the FFT, the mean and linear trend were subtracted from the data before analysis, and a Hamming window was applied. Gain is defined as the ratio between the amplitude of the response at 0.195 Hz and the amplitude of the stimulus (1D). Phase lag is defined as the phase difference between the accommodative stimulus sinusoid and the subject's response. Data from the six trials for each of the nine conditions were averaged for each condition.

An ANOVA Bonferroni T2 test (SPSS 15.0 for Windows) was performed to determine statistical differences in gain and phase lag across experimental conditions.

## 4.2. Results

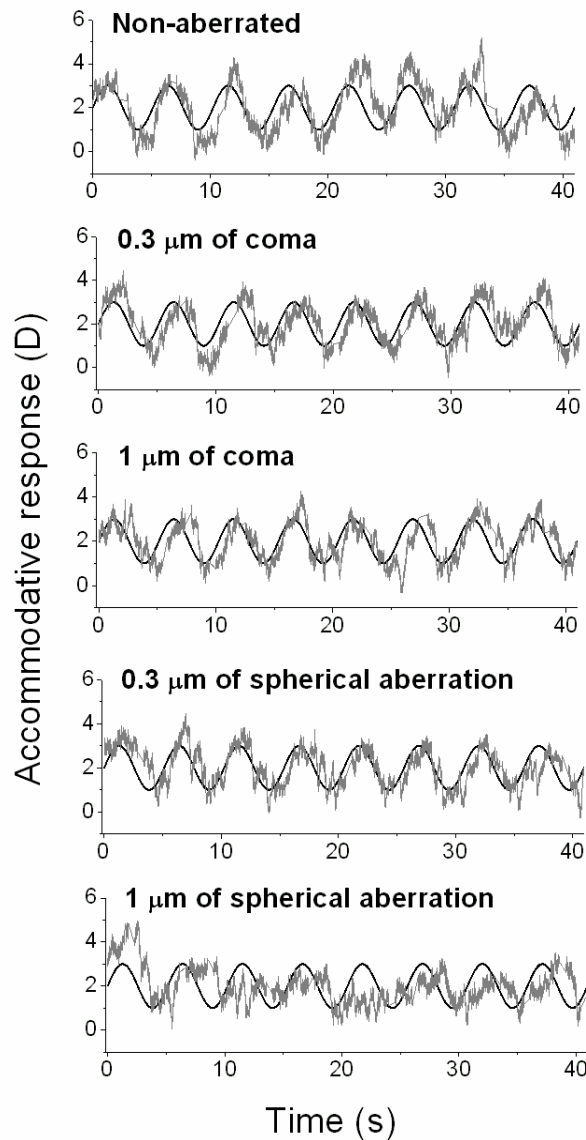


*Figure 4.3. Examples of dynamic accommodative responses of subject 1 to the non-aberrated stimulus and 0.3  $\mu\text{m}$  and 1  $\mu\text{m}$  of coma and spherical aberration. The accommodative demand is shown in black.*

Figure 4.3 shows some examples of the dynamic response of subject 1, an experienced subject with a very high gain, for the different experimental conditions: (a) the non-aberrated target, the original stimulus blurred with (b) 0.3  $\mu\text{m}$  and (c) 1  $\mu\text{m}$  of spherical aberration, and blurred with (d) 0.3  $\mu\text{m}$  and (e) 1  $\mu\text{m}$  of vertical coma. The gain decreased when the stimulus was blurred, especially for the higher amounts of aberrations and for spherical aberration. For the latter condition the subject experienced some problems in tracking the stimulus.

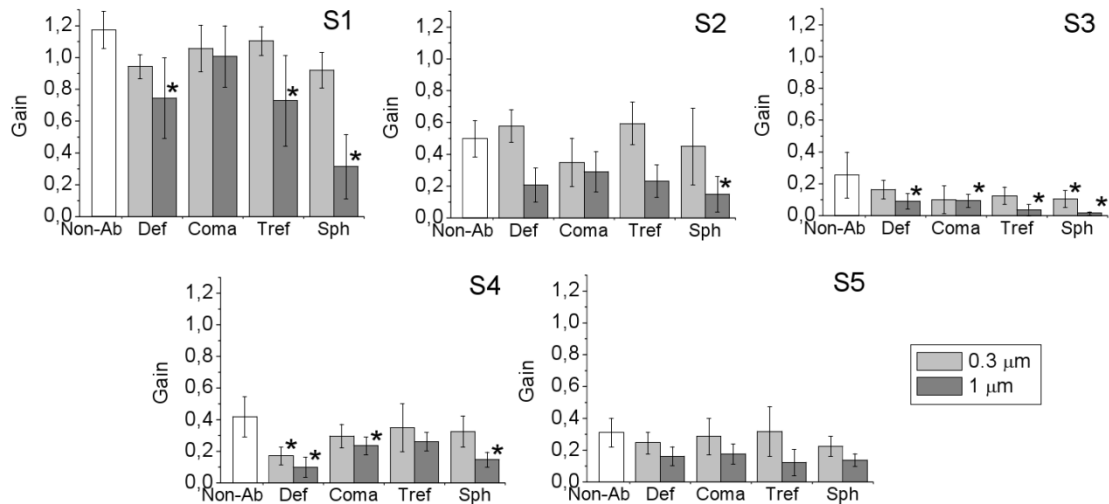


Figure 4.4. Mean absolute gain across conditions for every subject. Error bars are the standard deviation of the gain for every subject and condition. Gain is significantly different from the non-aberrated condition (ANOVA, Bonferroni T2).

Figure 4.4 shows the mean gain across conditions for every subject. As expected, the gain was lower when the stimulus was blurred with the higher amount of aberrations. The aberration type that most affected the dynamic response varied slightly across subjects, although trefoil tended to produce the lowest decrease in gain and defocus and spherical aberration the highest. Absolute gain also depends on the subject. We have defined the relative gain as the gain for each condition divided by the gain for the non-aberrated condition.

Relative gain averaged across subjects was lower when the stimulus was blurred with the higher amount of aberrations (see Figure 4.5A). Defocus, and especially spherical aberration, decreases the gain more than coma and trefoil. The drop in the gain is statistically significant ( $p < 0.002$ ) for all aberration types when  $1 \mu\text{m}$  was induced and only for spherical aberration when  $0.3 \mu\text{m}$  of spherical aberration was induced (ANOVA, Bonferroni T2). The mean phase lag increased in the presence of blur (Figure 4.5B), although the change was not statistically significant because of the large standard deviation of the mean values.

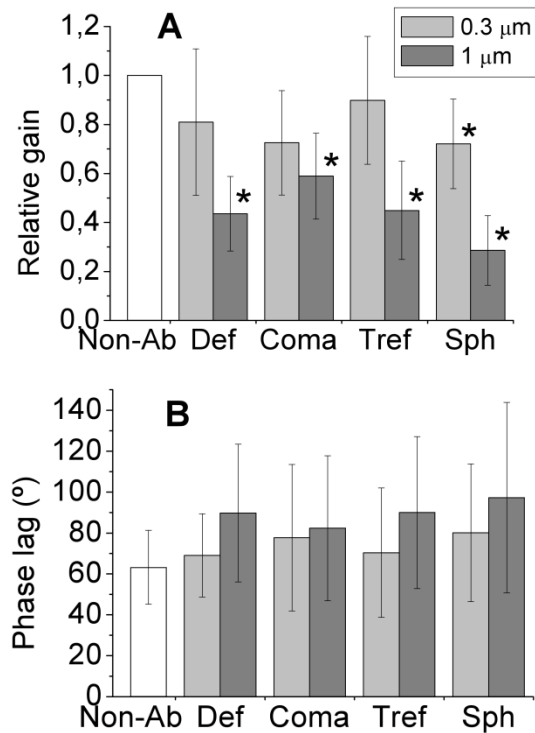


Figure 4.5. Relative gain (A) and phase lag (B) averaged across subjects. Error bars are the standard deviation of the mean values for the five subjects. Relative gain is significantly different from 1 (ANOVA, Bonferroni T2).

In most subjects, differences in the relative gain across conditions are quite consistent with the apparent degradation of the simulated targets (Figure 4.2), as it is well known that the same amount of aberration (expressed in Zernike weights) produces different amount of image blur, depending on the Zernike order and frequency [Applegate et al., 2003b]. To quantify these differences in blur across conditions, the modulation transfer functions corresponding to the aberration patterns used to simulate the blurred targets were calculated. The volume under the MTF (within a certain frequency range) was used as a retinal image quality metric. As Mathews and Kruger [1994] showed that frequencies around 3–5 c/deg are more important for accommodation, we have looked at the volume under the MTF in that frequency range, for all cases.

Figure 4.6A shows that there is a high correlation ( $p = 0.0004$ ) between relative gain and the volume under the MTF between 3 and 5 c/deg (normalized to the non-aberrated value). Temporal phase lag is also highly correlated ( $p < 0.0002$ ) with the volume under the MTF between 3 and 5 c/deg (Figure 4.6B). The correlation between relative gain and the volume under the MTF (cut-off at 100 c/deg) did not reach statistical significance ( $p = 0.076$ ).

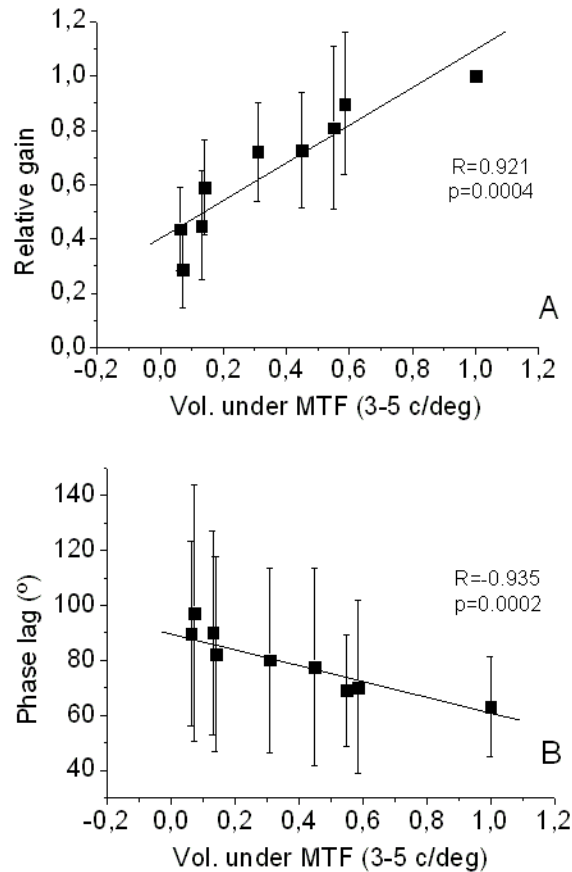


Figure 4.6. Correlation between the relative gain (A) and the phase lag (B) averaged across subjects and the volume under the MTF between 3 and 5 c/deg.

### 4.3. Discussion

We have shown that the blur induced by HOA impairs dynamic accommodation, proportionally to the amount of blur, due to the contrast degradation produced in the target. As the blur is imposed directly on the target (and not on the eye) the effects of potential interactions of the imposed aberrations with the natural aberrations of the eye are discarded. The inaccuracy of the accommodative response with aberrated targets seems to result from improper contrast content in the image, and the higher tolerance to defocus with blurred targets. The results support the findings obtained in previous studies that manipulated directly the phase, either inducing aberrations with contact lenses [López-Gil et al., 2007; Theagarayan et al., 2009] or correcting or inducing aberrations with adaptive optics (see Chapter 3).

Although interactions between the imposed aberrations and the natural aberrations of the eye may play a role in the final accommodative response (as shown in previous Chapter) the results of the current study support the conclusion that a major effect of increased aberrations (or in general, degraded retinal image quality) is a decrease in accommodative gain.

Our results show high intersubject variability in the absolute gain (even for the non-aberrated condition), which could arise from different sources. First, although the effect of the subjects' own natural aberrations was minimized by the use of a 3-mm pupil,

there are some residual high order aberrations, which varied across subjects. However, we did not find a correlation between the absolute gain and the amount of natural aberrations of the subjects.

Some other potential sources include: the experience of the subjects (S1 is highly experienced and S2 is moderately experienced) which could explain the highest performance of S1 and the relative good performance of S2, despite his relatively high amount of HOA; cues arising from the presence of specific HOA; and also the absence of other accommodative cues (such as longitudinal chromatic aberration, Lee et al., [1999]) that could be more important for some subjects than for others.

We found that the deleterious effects of blur on the accommodative response are only significant for amounts of aberrations much higher than typical values. This suggests that the effects of high order aberrations on gain and phase of dynamic accommodation is small and only present in subjects with an abnormally high amount of aberrations – such as keratoconic patients [Barbero et al., 2002]. These results are consistent with those found by López-Gil et al. [2007], Stark et al. [2009] and Chen et al. [2006].

Nevertheless, although the effect may not to be important even in patients with increased spherical aberration after standard refractive surgery [Marcos et al., 2001], it was demonstrated in Chapter 3 that the presence positive spherical aberration could be detrimental for accommodation due to a pupil constriction effect.

In our study, we found the largest effects to be caused by symmetric aberrations (defocus and spherical aberrations), which for the same amount of aberration produced the largest amount of image blur. The impact of those aberrations when induced optically would highly depend on the sign of the aberration (i.e. vergence of the wavefront), as coupling of defocus and spherical aberration (which also changes with accommodation) will modulate the induced aberration. These data are of importance when prescribing the newest refraction/presbyopia correction alternatives that modify the natural aberration pattern of the eye (either inducing or correcting aberrations).

#### **4.4. Open question**

In chapters 3 and 4 we explored the role of optical aberrations on accommodation. The two main contributors to the overall aberrations in the eye are the anterior surface of the cornea and the crystalline lens. The aberrations of the cornea can be assessed from the topographic maps of the front cornea, while the internal aberrations of the eye are usually evaluated by subtracting the corneal aberrations from the total aberrations of the eye. However, quantitative imaging of the ocular surfaces *in vivo* (dynamically or in 3D) opens the possibility to investigate the contribution of every individual optical surface to the total aberrations, in general, and the fluctuations of accommodation and the accommodative response, in particular.

The investigation of the contribution of the different surfaces to the total HOA requires the use of a high resolution imaging technique, which allows characterizing the geometry of the different optical elements of the eye. In the next chapter, the application of a promising technique, OCT, to imaging the accommodating crystalline lens is presented.

## **5. STATIC AND DYNAMIC CRYSTALLINE LENS ACCOMMODATION EVALUATED USING QUANTITATIVE 3-D OCT**

In this chapter the accommodating human lens is imaged with a Fourier Domain OCT system developed in collaboration with Nicholas Copernicus University Torún, Poland).

The author designed the study and the experimental protocols in collaboration with Susana Marcos and Sergio Ortiz, developed the accommodation module, collected the data in collaboration with Pablo Pérez-Merino and processed the data in collaboration with Sergio Ortiz and Pablo Pérez-Merino. The algorithms for denoising, segmentation, distortion correction and fitting of the optical surfaces from the OCT raw data were developed by Sergio Ortiz. The algorithms for merging the images were developed by Enrique Gamba.

This study was presented by the author in the following conferences:

- “Quantitative 3D-imaging of the in vivo crystalline lens during accommodation” (Oral communication), at ARVO 2010 Annual Meeting (Fort Lauderdale, Florida, USA, 2010);
- “Quantitative 3D-imaging of the crystalline lens during accommodation using high speed OCT system” (Oral communication), at IONS-9 (Salamanca, Spain, 2011);

The results were published in a peer review publication:

Gamba, E., Ortiz, S., Pérez-Merino, P., Gora, M., Wojtkowski, M., & Marcos, S. (2013). Static and dynamic crystalline lens accommodation evaluated using quantitative 3-D OCT. *Biomedical optics express*, 4(9), 1595-1609.

The accurate measurement of lens geometry is crucial for the understanding of crystalline lens optical properties and of the physical changes of the lens with accommodation and aging, for the design and evaluation of accommodation-restoration solutions for presbyopia, and to increase the predictability of intraocular lens implantation procedures. Until recently, most knowledge of the optical properties of the lens *in vivo* came from indirect measurements (i.e. the optical aberrations of the lens being typically computed as the difference of corneal and ocular wave aberrations).

In Chapter 1 we presented several imaging methods that have been used to assess crystalline lens geometry *in vivo* (Purkinje-imaging based methods, Scheimpflug imaging, Magnetic Resonance Imaging, and ultrasound biometry). However, Optical Coherence Tomography (OCT) appears as a highly promising tool to image the anterior segment of the eye, due to its high-resolution, high-speed and non-contact nature [Huang et al., 1991; Gora et al., 2009; Dunne et al., 2007; Yadav et al., 2010; Shen et al., 2010]. Provided with automatic quantification algorithms and with fan and optical distortion correction [Ortiz et al., 2009 and 2010], OCT has allowed 3-D quantification of the cornea [Ortiz et al., 2011; Karnowski et al., 2011], and lens [Ortiz et al., 2012a], as well as 3-D optical biometry [Ortiz et al., 2013]. The high speed acquisition of Fourier OCT techniques opens the possibility for tracking the crystalline lens dynamical changes, as the reported characteristic frequency of the fluctuations of accommodation falls within the bandwidth of state-of-the art OCT technology.

However, OCT imaging of the crystalline lens imposes some challenges, including a limited axial range, compromised by the resolution of the spectrometer (in spectrometer based OCT systems) or a limited instantaneous linewidth of tunable light source (in swept source OCT systems, [Furukawa et al., 2010]), which may be insufficient to image the entire anterior segment of the eye.

In the current study we characterized the geometry of the crystalline lens (anterior and posterior lens radii of curvature) for different accommodative demands (0 to 6 D) from 3-D quantitative sOCT anterior segment. We also estimated the dynamic fluctuations of crystalline lens geometry under steady fixation for different accommodative stimuli, to isolate the crystalline lens contributions to the dynamics of accommodation.

## 5.1. Methods

### 5.1.1. OCT system

A custom-developed spectral OCT system developed in collaboration with Optical Biomedical Imaging Group at Nicolaus Copernicus University (Torun, Poland) was used to collect the images [33]. The setup is based on a fiber-optics Michelson interferometer configuration with a superluminescent diode ( $\lambda_0 = 840$  nm,  $\Delta\lambda = 50$  nm) as a light source, and a spectrometer (volume diffraction grating, and a 12-bit 4096-pixel linescan CMOS camera) as a detector. The distance between the centers of the scanning mirrors is 13.8 mm and the focal length of the collimating lens before the eye is 75 mm.

The effective acquisition speed is 25000 A-Scans/s, which optimized balance between speed and SNR. The axial range of the instrument is 7 mm in air (around 5.2 mm in tissue), resulting in a theoretical axial pixel resolution of 3.4  $\mu\text{m}$ . The axial resolution predicted by the bandwidth of the SLD source is 6.9  $\mu\text{m}$ .

The axial measurement range can be doubled by using a piezotranslator mounted in the reference mirror that allows implementation of a technique of complex conjugate images removal based on a joint Spectral and Time domain OCT [Grulkowski et al., 2009].

An additional beam splitter was placed in the sample arm in order to incorporate an accommodating channel to the sOCT system. In this channel, a Badal system mounted on a motorized stage (VXM-1, Velmex) was used both for compensating spherical refractive errors and for inducing accommodative demands. A 12 mm x 9 mm SVGA OLED minidisplay (LE400, LiteEye Systems) was used to present the fixation stimulus. The fixation stimulus consisted of a black and white Maltese cross with eight arms (see Figure 2.7). The target subtended 5.14 deg and had a luminance of 50 cd/m<sup>2</sup>.

### **5.1.2. Subjects**

Images were collected on the left eyes of 4 young subjects (mean age: 26.5±2.5). Their refractions ranged between 0 to -6 D sphere and 0 to 1 D cylinder, and were optically corrected during the experiment. Spherical error was corrected by means of the Badal optometer, and cylinder by cylindrical trial lenses placed in a pupil conjugate plane in the accommodation channel. All subjects were trained subjects capable of accommodating, as assessed with IR dynamic retinoscopy (PowerRef II, Plusoptix) prior to the experiment.

Subjects signed a consent form approved by the Institutional Review Boards after they had been informed on the nature and possible consequences of the study, in accordance to the tenets of the Declaration of Helsinki.

### **5.1.3. Imaging protocols**

All measurements were performed under natural viewing conditions and undilated pupils. The subjects were stabilized using a bite bar and front rest. Alignment of the subject was performed with respect to the anterior corneal specular reflection, while the subject fixated a reference Maltese cross target projected on the minidisplay.

The SLD power exposure was fixed at 800 μW. The position of the reference mirror was changed manually between two fixed positions (one for imaging the cornea and the other, for the lens) during the experimental session in order to achieve optimal imaging of the different structures. This is needed because, although axial range would be sufficient to image the entire anterior segment at once, the sensitivity drop of the sOCT prevents from obtaining good image quality along the entire axial range. Typical raw sOCT images of the ocular surfaces are shown in Figure 5.1.

#### **5.1.3.1. Three-dimensional imaging of the anterior segment**

The anterior segment of the eye was imaged while stimulating accommodation from 0 to 6 D in 1-D steps. A total of 15 sets of 3-D data were collected in each subject's left eye for each condition of static accommodation: 5 images of the cornea, 5 images of the anterior part of the lens and 5 images of the posterior part of the lens. In order to minimize the impact of motion artifacts, every set of 3-D images was collected in less than 1 s.

Measurements were collected on a 6 mm (horizontal) x 15 mm (vertical) zone, using 40 B-Scans composed of a collection of 600 A-Scans, providing a lateral resolution of 0.025 mm for the horizontal meridian and 0.15 mm for the vertical meridian. Note that

this “lateral resolution” refers to the scanning density, not to the resolution of the system (which is determined by the size of the scanning ray).

### 5.1.3.2. Dynamics of the central B-scan

B-scans of the central horizontal meridian were acquired dynamically at a frequency of 14 Hz. The axial measurement range was doubled by using the piezo-translator function, in order to image the anterior and posterior surfaces of the lens simultaneously. Images of the lens were obtained in one subject while stimulating accommodation from 0 to 6 D in 1-D steps. For each accommodative condition, one 3-D image of the cornea (from which the apex image was selected) and 5 sets of 70 images of the central section (15 mm lateral range) of the entire crystalline lens were acquired during 5 seconds. Every lens cross-sectional image (and every corneal B-scan) was composed by a collection of 1668 A-Scans, providing a lateral resolution of 9  $\mu\text{m}$ .

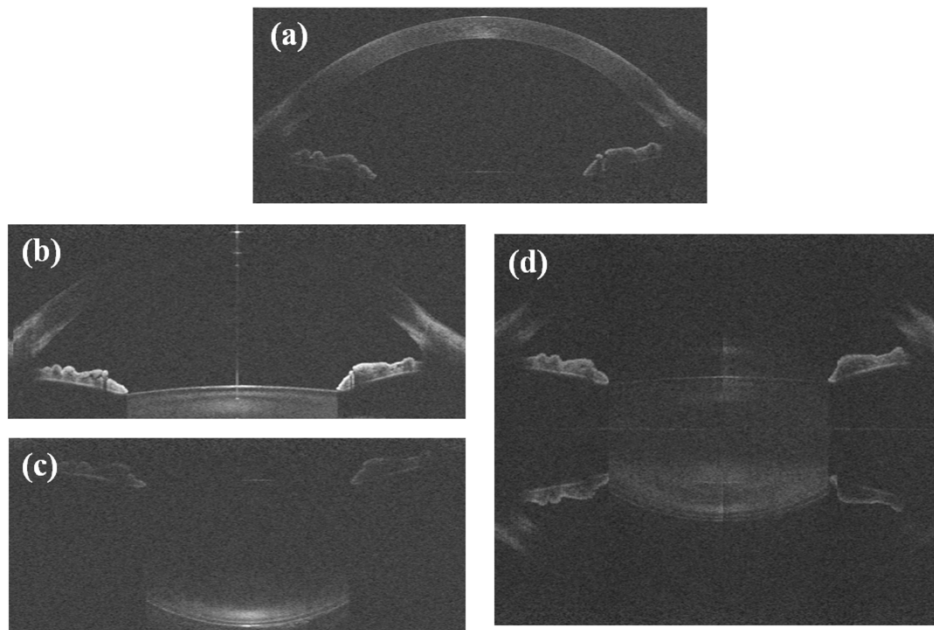


Figure 5.1. Typical raw sOCT images: (a) cornea; (b) anterior crystalline lens surface; (c) posterior crystalline lens surface, imaged separately in the 3-D protocol; (d) entire crystalline lens, imaged simultaneously using the complex conjugate images removal technique, in the dynamic 2-D image acquisition. After the unfolding procedure, a mirror image of some elements of the eye can still be seen.

### 5.1.4. 3-D image processing: denoising, segmentation, merging, distortion correction and surface fitting

The 3-D processing of the anterior chamber images obtained with the OCT system has been extensively described in previous works by Ortiz et al. [2012a, 2012b]. The image processing algorithm can be summarized in nine steps. A brief description of all of them is here exposed. This description has been elaborated from Ortiz et al., [2012b]. For this study, the merging step was different than described in Ortiz et al. [2012b] and was developed by the author of this thesis.

- 1) Denoising: A rotational kernel transform was performed for an edge-preserving denoising, using a mask of size 9 pixels [Ortiz et al., 2012a]. In addition, a wavelet low-pass filtering processing based on log-Gabor wavelet was used for 7 scales and 6 orientations.

- 2) Statistical thresholding: An adaptive algorithm based on a multimodal Gaussian fitting of the histogram intensity (in a non-linear least squares sense) was performed on the entire 3-D sets of data, which allowed identifying a noise class from the signal.
- 3) Volume clustering: The statistics of the noise and signal are overlapped. As a result, small randomly distributed volumes are mixed with the large volumes representing the objects of interest in 3-D (cornea, iris, lens surfaces, etc...). The number of pixels belonging to certain a volume was obtained by means of the connectivity of points. The volumes of interest were obtained by thresholding the number of elements according to the expected total number.
- 4) Multilayer segmentation: Automatic segmentation was based on Canny detection in each A-scan (1-D signals). In an initial step, a Gaussian filter was applied to reduce spurious peaks associated to noise detection in the CMOS line-camera. The first derivatives of the signal were then obtained, providing both local maxima and minima of the A-scan. The number of local maxima was further reduced by thresholding the signal and removing the peaks below a certain value. The maxima identified in the A-scans were connected in the 2-D cross-sections (B-scans) or in the 3-D data sets using the same neighborhood algorithm used for clustering, therefore allowing to segment layers.
- 5) Pupil center reference: The pupil center was used as a reference across measurements (i.e. cornea, anterior and posterior lens) and to define the optical zone (effective area within the pupil). In this study, the lateral pupil coordinates and the optical zone were obtained by fitting the outer edge of pupil in 2-D en face images (computed by adding all images of a 3-D data set) to an ellipse. Besides, the axial coordinate was obtained by nonlinear least-square fitting of the iris plane in 3-D (and evaluation of the plane at the estimated pupil lateral coordinates). In addition, the characteristic vector of the iris plane was obtained, which provided the tilt angle of this plane with respect to the OCT coordinate system.
- 6) Merging 3-D volumes: Pupil coordinates are assumed as a common reference for the images of the anterior segment collected at different depths. In a first step prior to merging, the corneal image was inverted, as for efficiency in the focus range shift, the cornea was acquired in the opposite side of the Fourier transform (in comparison with the crystalline lens acquisition). The corneal volume and the anterior crystalline lens volumes were merged using the limbus as a landmark for registration. Besides, the two crystalline lens volumes were merged using the pupil as landmark for registration.
- 7) Geometrical distances calculation and further denoising: The registration of the 3-D volumetric data sets involved shift and rotation by coordinates in optical distances, which requires re-sampling and interpolation. The optical distance can be then calculated by direct subtraction of the coordinates of the different surfaces (anterior-posterior cornea and anterior-posterior lens), while the geometrical distances were obtained by dividing the optical distance by the corresponding group refractive index at the illumination wavelength. The corneal refractive index was taken as 1.376, the aqueous humor refractive index as 1.336, and the crystalline lens refractive index was obtained from the age-dependent average refractive index expression derived by Uhlhorn et al. [2008] (1.4176-1.4186 for the subjects of our study). The sampled anterior segment elevation data from anterior and posterior surfaces of the cornea and the lens were denoised using a fitting Zernike modal expansion (55 terms, 10th order).

This iterative method allows further rejection of spurious points in the surface due to detection process.

- 8) Distortion corrections: In order to correct the interface layers for the effect of distortion in general (fan distortion and optical distortion), it is required to propagate the geometrical distances obtained from the previous point along the directional cosines of the ray, taking into account the refraction that occurs at each interface between two media of different refractive indices [de Castro et al., 2012].
- 9) Surface fitting by quadrics (biconicoid): The surfaces were fitted by quadrics in a 5-mm of diameter optical zone with respect to their apexes. The radii of curvature  $R_x$  and  $R_y$  were obtained by biconic fitting.

For the current study, the technique was also adapted to the correction of cross-sectional images of the lens. The B-scan of the cornea 3-D measurements in which the apex reflection was observed was selected and used for optical distortion correction of the 2-D lens images. Corneal cross-sections were merged with the lens cross-sectional images, using the pupil inner edges as a landmark. A ray-tracing analysis (here in 2-D) similar to that used in the corrections of 3-D data sets was implemented and applied to correct the anterior and posterior lens surface from the corneal and anterior lens refraction.

### **5.1.5. Data analysis**

#### **5.1.5.1. Lens phakometry**

The surfaces of the lens were fitted by quadrics, both in 3-D and in 2-D, in a 5-mm diameter optical zone centered at their apexes. In 3-D, the lens radii of curvature were obtained by fitting to a sphere of radius of curvature  $R$ . Dynamic 2-D lens horizontal sections were fitted by circumferences (defined by the radius of curvature  $R$ ).

#### **5.1.5.2. Pupillometry, Anterior Chamber Depth and Lens Thickness**

Pupil center and diameter were estimated in the 3-D images using the algorithm previously described. The anterior chamber depth (ACD) was estimated as the distance between the intersections of the vector defined by the centers of curvature of the posterior cornea and anterior lens with the corresponding surfaces. The lens thickness (LT) was estimated as the distance between the intersection of the vector that joins the centers of curvature of anterior and posterior lens with the corresponding surfaces. These definitions were applied for both the 3-D and 2-D sets of data.

#### **5.1.5.3. Accommodative response**

The accommodative response of the eye was estimated considering the variation of lens geometry (and position) with increasing accommodative demand, and computed for each data set obtained during the dynamic acquisition. A schematic eye model was used in order to estimate the change in refraction of the entire eye. Eye refraction was estimated under the paraxial approximation (see equations below), using the measured data of corneal radius of curvature, lens radii of curvature, ACD and LT. The accommodative response of the eye was obtained from the change in its total refraction with increasing accommodative demand, and compared with the isolated contribution of the crystalline lens (Equation 5.2).

$$P = P_C + P_L - \frac{ACD \cdot P_C \cdot P_L}{n_h} + \frac{(n_l - n_h) \cdot LT \cdot P_C}{n_h^2 R_p} \quad \text{Equation 5.1}$$

$$P_C = \frac{n_h - 1}{n_h R_C}$$

$$P_L = \frac{n_l - n_h}{n_h} \left( \frac{1}{R_a} - \frac{1}{R_p} \right) + \frac{(n_l - n_h)^2 LT}{n_l n_h R_a R_p} \quad \text{Equation 5.2}$$

where  $P$  is the power of the eye and  $P_C$  and  $P_L$  the power of the equivalent cornea and of the crystalline lens, respectively;  $n_l$  is the equivalent refractive index of the lens according to Dubbelman and Van der Heijde [2001], and  $n_h$  is the refractive index of aqueous and vitreous humors;  $R_c$ ,  $R_a$  and  $R_p$  are the radii of curvature of the equivalent cornea and of the anterior and posterior lens surfaces, respectively;  $ACD$  is the anterior chamber depth; and  $LT$  is lens thickness.

Images providing insufficient quality to allow correct surface segmentation (usually due to insufficient signal in the posterior lens surface) were removed. When performing a Fourier analysis in the 2-D data, these removed data were replaced by a linear interpolation between the calculated values for their closest neighbors. The rate of total number of data and removed data sets was less than 5.5%.

#### 5.1.5.4. Fluctuations of accommodation

The fluctuations of the accommodative response during sustained accommodation were calculated as the standard deviation of the estimated accommodative response. These were computed for each accommodative demand (5-second periods). The contribution of the noise inherent to the OCT system and image processing was estimated (from a series of images obtained under paralyzed accommodation with Tropicamide 1%) and taken into account (using error propagation) in the determination of the fluctuations associated solely to the accommodative response.

Alternatively, we obtained the frequency spectra of the accommodative responses for each of the 5-second sequences (for the different accommodative demands), using Fourier analysis. The area under the frequency spectra was numerically calculated for low (0–0.6 Hz) and high (0.9–2.5 Hz) frequency regions. The area under these curves, particularly in the low frequency range, has been related to the magnitude of the fluctuations of accommodation [Charman and Tucker, 1977].

The fluctuations of other biometric and phakometric magnitudes ( $ACD$ ,  $LT$ ) and of the radii of curvature of the lens were also estimated and compared with the fluctuations of the optical power. A sensitivity analysis was performed to assess the impact of each of these magnitudes on the fluctuations of the optical power of the lens, by recalculating these fluctuations while keeping constant (and equal to their mean value) the rest of the magnitudes.

Furthermore, the coefficient of correlation ( $r$ ) between the dynamic ACD and LT was calculated for every accommodative state in order to assess whether the changes in ACD were either due to changes in lens thickness or to translational lens movements. If  $r = -1$  the decrease in the ACD would be related to the increase in LT, while if  $r = 0$  the decrease in ACD would be related to a forward shift of the lens. Finally, correlations between the changes in LT and radii of curvature were performed to assess whether the fluctuations in LT were primarily due to fluctuations in lens radii of curvature.

## 5.2. Results

### 5.2.1. 3-D imaging of the segment

#### 5.2.1.1. Radii of curvature

Figure 5.2 shows the change of radii of curvature of the anterior and posterior surfaces with accommodative demand. Data are for the four individual subjects, and the average across subjects. As previously reported, the lens (particularly the lens anterior surface) becomes steeper with the accommodative demand.

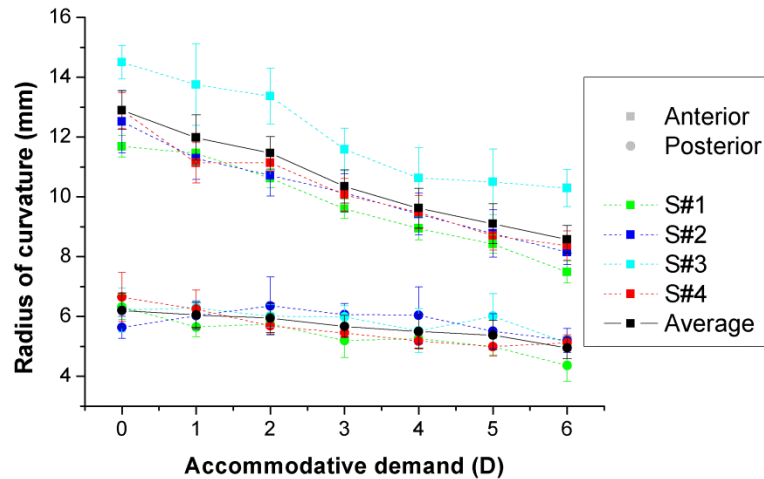


Figure 5.2. Radii of curvature of the anterior (squares) and posterior (circles) surfaces of the lens for the individual subjects (color symbols with dashed lines) and the average across subjects (black symbols with solid lines). Data for each subject are average of 5 repeated measurements. Error bars stand for standard deviation of repeated measurements. The radius of curvature of the posterior surface of the lens is negative, but has been depicted positive for illustration purposes.

#### 5.2.1.2. Accommodative response

The optical power of the lens was estimated for all subjects, using Equation 5.2. The optical power of the lens ranged from 16.1 to 18.8 D across subjects in the unaccommodated condition, and from 20.39 to 22.14 D in the condition of highest accommodative demand. The average lens optical power change rate was 0.82 D/D (of accommodative demand). Figure 5.3 shows the change in the total eye optical power estimated from biometric and geometrical data for all subjects, using Equation 5.1. The maximum amplitude of the accommodative response was on average 3.83 D, for an accommodative demand of 6 D. The average total optical power change rate was 0.62 D/D.

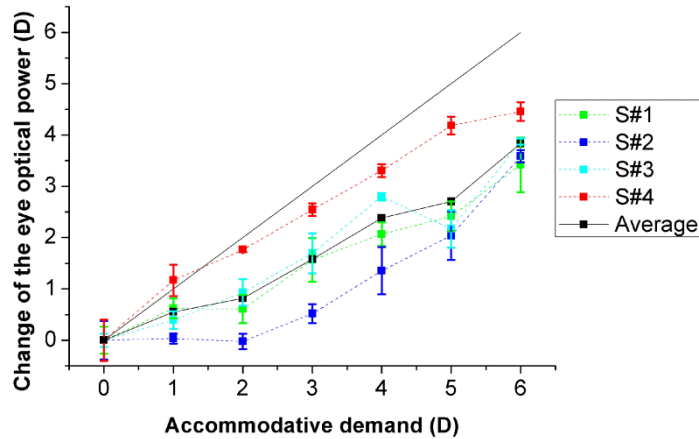


Figure 5.3. Change in the optical power of the eye with accommodative demand, with respect to the value obtained for the unaccommodated condition (0D). Data are average of 5 repeated measurements for each subject. Solid line corresponds to the ideal response. Error bars stand for half of the standard deviation of repeated measurements (for clarity).

### 5.2.2. Biometry and phakometry with dynamic central B-scan cross-sections

Figure 5.4 shows pupil diameter (a), anterior chamber depth (b), lens thickness (c), and lens radii of curvature (d) as a function of accommodative demand, estimated from cross-sectional OCT images, for subject #4. Each data point is the average of 58-70 measurements during sustained accommodation (recorded during 5 s at each accommodative level).

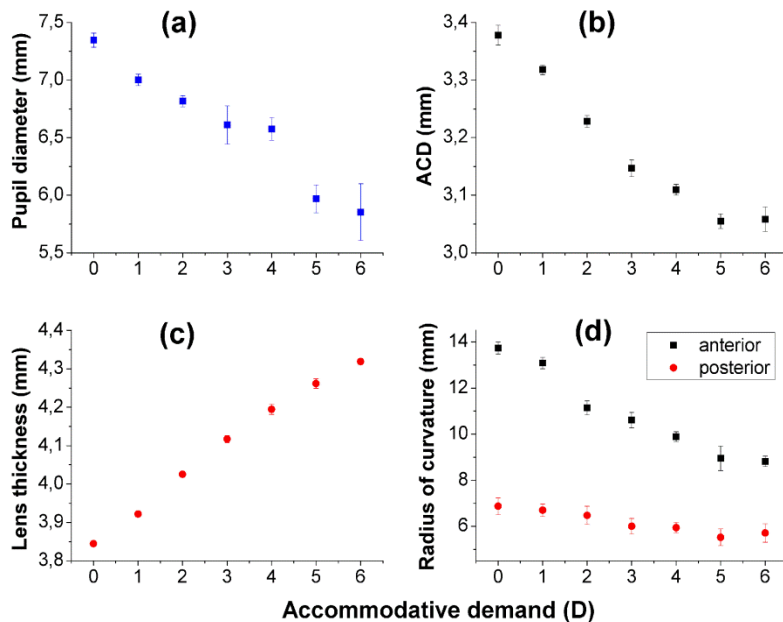


Figure 5.4. Anterior segment geometry as a function of accommodative demand: (a) Pupil diameter, (b) anterior chamber depth, (c) lens thickness, and (d) lens radii of curvature. Error bars stand for the standard deviation of data from 58-70 images acquired during 5 seconds of sustained accommodation (at each accommodative demand).

Pupil diameter decreased from 0 to 6 D of accommodative demand by 1.49 mm on average (Figure 5.4a), ACD by 0.320 mm on average (Figure 5.4b) and lens thickness

increased by 0.473 mm on average (Figure 5.4c). These results are consistent with a forward shift of the lens with accommodation (by around 0.083 mm from 0 to 6 D of accommodative demand).

The lens radii of curvature obtained from horizontal cross-sectional images (Figure 5.4d) are similar to the radii of curvature obtained in a different set of 3-D sets of data on the same eye: the anterior and posterior radius of curvature were, respectively, 4.5% and 8.1 % higher than the average radii of curvature from 3-D data (with this difference remaining similar across accommodative demands). The difference between the 3-D and 2-D comes from the fact that in 3-D radii of curvature from all meridians are added whereas in the 2-D they correspond to horizontal section only. This is consistent with a previous report in an un-accommodated eye [Ortiz et al., 2012], in which horizontal radii of curvature was higher than the vertical one for this particular subject.

Similarly as done with the 3-D data, the optical power of the lens was estimated from the 2-D phakometric data for the different accommodative demands. The change in the eye optical power with accommodation was 10% lower when obtained from 2-D cross-sections (0.67 D/D) than from 3-D data sets (0.75 D/D, for S#4), consistent with the slightly higher horizontal lens radii of curvature.

### 5.2.3. Dynamics of the central B-scan

Figure 5.5 shows the temporal variation of the eye optical power during the 5-second of sustained accommodation, for each accommodative demand, estimated from Equation 5.1 using the radii of curvature and biometric data obtained for each image of the sequence.

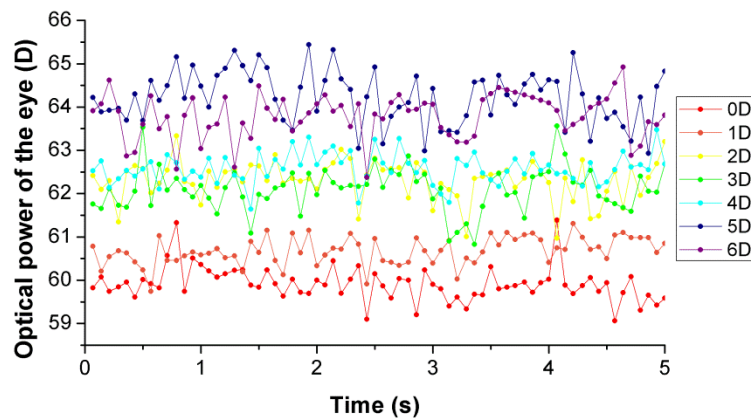


Figure 5.5. Optical power of the eye during 5 seconds of sustained accommodation, for different accommodative demands.

Figure 5.6(a) shows the fluctuations of the lens optical power (blue symbols) and eye optical power (green symbols), defined as the standard deviation of the estimated power, for each accommodative demand. The lens power fluctuations arise from variations in the lens radii of curvature and lens thickness. The entire eye power fluctuations also incorporate the variations in ACD (but not potential changes in corneal power or eye axial length), as well as the fluctuations of the optical power of the lens. The fluctuations of the eye optical power are on average 0.16 D lower than the fluctuations of the lens optical power. The fluctuations of accommodation increase significantly with accommodative demand, at a rate of 0.044 D/D of accommodative demand.

Figure 5.6(b) shows the area under the power spectrum density curve of the optical power of the eye, numerically calculated for low (0–0.6 Hz) and high (0.9–2.5 Hz) frequency bands. The correlation between the standard deviation of the optical power and the area under the power spectrum density was higher for the high frequency range ( $r=0.74$ ,  $p=0.056$ ) than for the low frequency range ( $r=0.69$ ,  $p=0.084$ ).

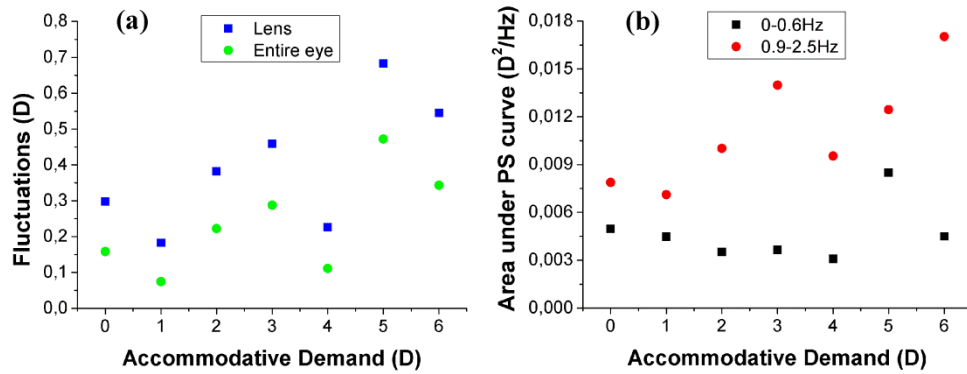


Figure 5.6. (a) Fluctuations of the optical power of the lens and of the entire eye calculated as the standard deviation of the power estimates during 5-seconds of sustained accommodation, as a function of the accommodative demand. (b) Area under the power spectrum density curve of the optical power of the eye in two different frequency bands (0-0.6 Hz and 0.9-2.5 Hz), as a function of accommodative demand.

Fluctuations of the optical power of the lens due only to ACD, LT and anterior and posterior radii of curvature (calculated from the experimental data, by allowing one magnitude to vary while keeping constant the other three) were estimated. The results of this sensitivity analysis are shown in Figure 5.7, where the contribution of the different parameters is shown for the different accommodative demands. Fluctuations in optical power are primarily dominated by changes in the radii of curvature of the lens, especially the posterior surface. The contribution of the fluctuations of the anterior radius of curvature to the overall fluctuations tends to increase with accommodative demand, while the contributions of ACD and LT are always very small and do not show a trend with accommodation.

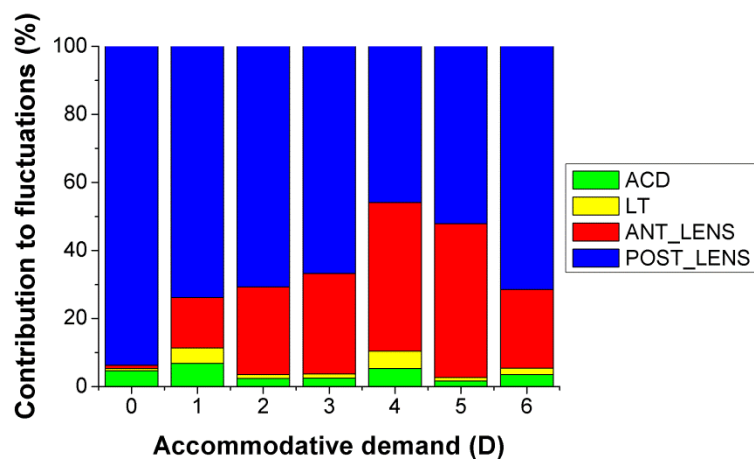


Figure 5.7. Relative contribution of the anterior chamber depth (ACD), lens thickness (LT) and anterior and posterior lens radii to the fluctuations of the optical power of the eye.

Fluctuations in ACD, lens thickness, radii of curvature of the lens surfaces were also estimated and Pearson's correlation coefficient ( $r$ ) between some of these magnitudes

was calculated for every accommodative demand. No significant correlation was found between the ACD and LT, except for 3 D of accommodative demand ( $r=-0.37$ ,  $p=0.002$ ). Besides, LT correlated significantly with anterior lens radius for 1 D ( $r=-0.35$ ,  $p=0.003$ ), 2 D ( $r=-0.3$ ,  $p=0.002$ ) and 3D ( $r=-0.32$ ,  $p=0.010$ ), and with posterior lens radius only for 0 D ( $r=-0.26$ ,  $p=0.038$ ).

On the other hand, mean values of ACD, lens thickness, and radii of curvature of the lens surfaces correlate across accommodation with the mean value of the optical power of the eye ( $r$  modulus ranging from 0.92 to 0.99), as expected from the results already shown in Figure 5.4.

### 5.3. Discussion

Ortiz et al. [2012a] used quantitative sOCT to obtain the first 3-D topography of the crystalline lens *in vivo*. In this study, we have extended that methodology to assess changes in the shape of the crystalline lens with accommodation, and provided, for the first time to our knowledge, phakometric measurements with accommodation derived from 3-D data. In addition, we have also shown the capability of the OCT technology, making use of its high acquisition rates, to assess the dynamics of accommodation.

Despite the relatively long axial range, the sensitivity drop in the sOCT system prevents from imaging simultaneously the entire anterior segment of the eye. We have overcome the problem by imaging separately the different surfaces and using the limbus and the iris as landmarks for registration of different images at different planes of focus. Swept source OCT imaging can be alternatively used to image the cornea and the lens simultaneously [Grulkowski et al., 2012; Satoh et al., 2013].

The measured lens radii of curvature, obtained from 3-D OCT images, are comparable to values in the literature. In the un-accommodated condition, we found average radii of  $12.90\pm 0.64$  mm for the anterior lens and  $6.20\pm 0.59$  mm for the posterior lens. In a previous report using similar methodology, Ortiz et al. [2012a] reported  $11.90\pm 1.34$  mm for anterior lens radius of curvature and  $6.86\pm 0.63$  mm for the posterior lens, in 3 subjects. Dubbelman et al. [2001] reported an age-dependent expression for the anterior and posterior lens radius of human lenses *in vivo* based on corrected Scheimpflug measurements, which predicts 11.25-11.59 mm and 5.85-5.92 mm for the anterior and posterior lens radii respectively for the age range of the subjects of our study. Rosales et al. [2006] measured the crystalline lens radii of curvature using both Purkinje and Scheimpflug imaging, and reported average values of 10.8 mm and 11.1 mm, and 6.7 mm and 6.1 mm from each technique, for anterior and posterior lens radius of curvature, respectively. Koretz et al. [2004] used both Scheimpflug and MRI in a comparative study, and obtained values of 11.90 mm and 5.58 mm for the anterior and posterior lens radii of curvature, respectively, with Scheimpflug photography, and 11.20 mm and 6.15 mm, respectively with MRI. Finally, in recent study using 2-D OCT, Shao et al. [2013] reported values of 11.87 mm and 5.68 mm for the anterior and posterior lens radii of curvature, respectively, in a single 26-year-old subject. The lens radii of curvature ranges of our study (11.7-14.5 mm and 5.6-6.6 mm, for anterior and posterior lens surfaces) match well those reported by Dubbelman et al. [2001] (9-14 mm and 4.7-7 mm, respectively).

In addition, we have measured the lens shape in 3-D, for increasing accommodative demand (0 to 6 D, 1-D steps). We found a decrease of 0.73 mm/D accommodative demand for the anterior lens radius of curvature, and 0.20 mm/D for the posterior lens

(see Figure 5.2). These rates can be compared with those obtained in the literature using Scheimpflug or Purkinje imaging. Differences may arise from differences in the accommodative demand range used for testing and the actual accommodative response. Dubbelman et al. [2005] using 2-D Scheimpflug photography for accommodative demands up to 8 D reported rates of  $0.61 \pm 0.15$  mm/D and  $0.13 \pm 0.06$  mm/D for the anterior and posterior lens radius, respectively. Rosales et al. [2006] reported 0.64 mm/D (Scheimpflug) and 0.57 mm/D, (Purkinje) for the anterior lens, and 0.23 mm/D (Scheimpflug) and 0.29 mm/D (Purkinje) for the posterior lens, for an 8-D accommodative demand range. Garner and Yap [1997] using Purkinje imaging reported rates of 0.62 mm/D and 0.17 mm/D for the anterior and posterior lens, respectively, for a 8-D accommodative range. Shao et al. [2013] using 2-D sOCT reported rates of 1.06 mm/D and 0.29 mm/D for the anterior and posterior lens, respectively for a 4-D accommodative demand range.

Assuming an equivalent refraction index for the crystalline lens (according to that reported by Dubbelman et al. [2001] in subjects of the same age range) we estimated the change of the optical power of the eye from physical changes in the lens and anterior segment biometry. We found that the change in the optical power of the eye with accommodation (0.62 D/D) is smaller than the change in the optical power of the crystalline lens (0.82 D/D). This difference can be explained considering Equation 5.1, which shows that the lens power has contributions of opposite sign to the eye optical power. Assuming that the accommodative response is equal to the estimated change of the optical power of the eye, we found an accommodative response amplitude of 3.83 D, which is similar to the accommodative response of 3.78 D reported in Chapter 3 in 5 young subjects, the 3.5 D reported by He et al. [2000], and the 4 D reported by Plainis et al. [2005], all of them using a Hartmann-Shack-based measurements of refraction, and for a similar accommodative-demand range of 6 D range. Besides, McClelland and Saunders [2003] measured the accommodative response to a 6 D stimulus in 40 subjects, and reported average values of  $4.57 \pm 0.69$  and  $4.43 \pm 0.73$  using dynamic retinoscopy and a Shin-Nippon autorefractor, respectively. The effective accommodation amplitude, discounting the effect of the accommodative lead at 0 D (between 0.5 and 1 D in most studies [He et al., 2000; Plainis et al., 2005]) is very similar to that obtained on anatomical bases in our study.

Besides phakometric changes, we also report biometric changes with accommodation, obtained from sOCT. The change in ACD and LT with accommodative demand ( $-0.057$  mm/D and  $0.081$  mm/D of accommodative demand, see Figure 5.4(b) and 5.4(c)) are within the ranges reported in the literature:  $-0.037$  mm/D (ACD) and  $0.045$  mm/D (LT), for a 27 year old subject, for an accommodative demand range of 8 D, using Scheimpflug imaging [Dubbelman et al., 2005];  $-0.062$  mm/D (ACD) and  $0.066$  mm/D (LT), in 15 subjects, with an accommodative demand of 5 D, using MRI [Kasthurirangan et al., 2011];  $-0.033$  mm/D (ACD) and  $0.034$  mm/D (LT) in one 37-old subject, for an accommodative demand range of 5.5 D using 2-D OCT [Kasthurirangan et al., 2011];  $-0.025$  mm/D (ACD) and  $0.06$  mm/D (LT) in a 26-old subject for an accommodative demand range of 4 D using 2-D OCT [Shao et al., 2013]; and  $-0.019$  mm/D (ACD) and  $0.058$  mm/D (LT) for an accommodative demand range of 4 D, using 2-D OCT [Ruggeri et al., 2012]. Due to the limited the axial range of the sOCT, we are not able to provide data of the changes in the axial length of the eye with accommodation, that have been provided by partial coherence interferometry [Drexler et al., 1998], combination of two OCT systems focused in different planes [Dai et al., 2012] or rapid switch between planes [Ruggeri et al., 2012].

Finally, several studies have evaluated the fluctuations of refractive error upon accommodation to steady targets, as a function of the accommodative demand. Potential noise in the system has been discounted. Also, from previous studies *in vitro*, the effects of error propagation throughout the different optical surfaces is small [Ortiz et al., 2009 and 2010]. As OCT allows imaging the different optical surfaces of the eye, this study has extended previous reports on microfluctuations using ultrasonography that could only measure axial distances [van der Heijde et al., 1996]. Some studies report a systematic increase of these fluctuations for increased accommodation [Kotulak and Schor, 1986; Chapter 3 of these thesis], and other studies report a maximum value for intermediate levels of accommodation [Plainis et al., 2005; Mieke and Denieul, 1988]. Our study has extended this work by assessing the isolated contributions of lens shape changes, and biometrical changes to the dynamics of accommodation. Estimations of the eye power from geometrical measurements reveal an increase of the fluctuations with accommodation, ranging from 0.07 D to 0.47 D between 0 and 6 D (0.044 D per D of accommodative demand). These fluctuations and its changes with accommodation are comparable to those reported in Chapter 3, from dynamic Hartmann-Shack-based measurements of refraction (from 0.09 D to 0.31 D for 0-6 D accommodative demand range, with a slope of 0.049 D/D) and Kotulak and Schor, who found a slope of 0.047 D/D using an infrared optometer [Kotulak and Schor, 1986]. A sensitivity analysis revealed that the fluctuations of accommodation were driven by dynamic changes in the lens surfaces, particularly in the posterior lens surface.

## 6. CONCLUSIONS

This thesis has investigated several aspects of the accommodation process: it addresses the influence of high order aberrations on the accommodation accuracy and fluctuations, as well as the quantitative changes in the crystalline lens geometry with accommodation.

### 6.1. Achievements

In this thesis, we have accomplished the following achievements:

- Development of a AO system for manipulating high order aberration and measuring accommodation response, with a motorized Badal optometer for stimulating accommodation.
- For the first time accommodation response has been systematically measured across a wide range of accommodative stimulus while manipulating aberrations to study their influence on accommodative lag.
- The effect on accommodation accuracy of optically-induced spherical aberration of different sign has been explored.
- The impact of blurring the accommodation stimulus with AO-aberrations on dynamic accommodation has been studied.
- For the first time 3-D quantitative images of the crystalline lens have been obtained across a wide range of accommodation demands.
- Also for the first time, different contributions of the crystalline lens to the fluctuations of accommodation have been explored.

### 6.2. Conclusions

1. The correction of high order aberrations results in better accommodation response, while the optical induction of high order aberrations worsens the accommodation performance (Chapter 3)
2. The presence of a high amount of positive spherical aberration is detrimental to the accommodation response: it not only blurs the stimulus, but the combined effect of the decreasing pupil size with the accommodation effort is deleterious for the accommodative accuracy. On the other hand, the presence of negative spherical aberration reduces the accommodative lag, even if it blurs the stimulus (Chapter 3).
3. To accurately estimate the accommodation effort from Zernike coefficients, it is necessary to consider defocus and both 4<sup>th</sup> and 6<sup>th</sup> order spherical aberration terms (Chapter 3).
4. Target blur induced by high order aberrations impairs dynamic accommodation, proportionally to the amount of blur. The effects are only significant for amounts of aberrations higher than typical values (Chapter 4).
5. The decrease in the gain of the dynamic accommodation is highly correlated with the value of the MTF at the relevant frequencies of accommodation (Chapter 4).
6. Decrease of accommodation response in the presence of high order aberrations is in part due to a higher tolerance to blur (Chapter 4).

7. Fluctuations of accommodation systematically increase with accommodative response between 0 and 6 diopters of accommodative demand. This result has been independently achieved in two different studies. The increase in fluctuations with accommodation was 0.049 diopters per diopter of accommodative effort in the AO study (Chapter 3) and 0.044 diopters per diopter of accommodative demand in the sOCT study (Chapter 5).
8. Fluctuations of accommodation tend to be higher in the presence of bigger amounts of high order aberrations, which can be associated to the larger depth of focus (Chapter 3).
9. As revealed by a sensitivity analysis, the fluctuations of accommodation are driven by dynamic changes in the lens surfaces, particularly in the radius of curvature of the posterior lens surface (Chapter 5).
10. High-speed, high resolution FD-OCT – provided with distortion correction algorithms – allows quantitative 3-D imaging and dynamic 2-D imaging of the crystalline lens during accommodation. The technique allows to evaluate changes in the radii of curvature and position of the lens surfaces (Chapter 5).
11. Using the 3-D OCT images, we found an average radii of 12.90±0.64 mm for the anterior lens and 6.20±0.59 mm for the posterior lens, for the unaccommodated condition in 4 subjects. For increasing accommodative demand (0 to 6 D, 1-D steps), we found a decrease of 0.73 mm/D accommodative demand for the anterior lens radius of curvature, and 0.20 mm/D for the posterior lens radius of curvature.
12. From the sOCT images, biometric changes with accommodation have been reported: a change with accommodative demand of -0.057 mm/D in the anterior chamber depth and 0.081 mm/D in the lens thickness have been found.

### 6.3. Future work

In this thesis, an Adaptive Optics system and a spectral domain OCT system have been used to explore different aspects of the accommodation mechanism. The independent or combined utilization of these two powerful techniques can provide further knowledge on accommodation. AO allows correction and induction of aberrations, therefore allowing simulation of different corrections, and testing visual perception, visual function and neural adaptation to those. Simulated optics include aspheric IOLs, multifocal corrections, and other's subjects aberrations.

Quantitative OCT is also an excellent tool for evaluation of the mechanism of action of premium IOLs, such as accommodating IOLs. Besides, pre-operative OCT-based 3D biometry will allow more accurate selection of IOLs, using ray tracing on custom eye models personalized to the patient's anatomy.

The quantitative capabilities of OCT can be further expanded to fully characterize the crystalline lens, beyond radii of curvature and axial distances. In particular, ongoing studies have allowed the measurement of the crystalline lens surface topography of the anterior and posterior lens, both *in vivo* and *ex vivo*. One ongoing study in the Visual Optics and Biophotonics laboratory investigates changes in the surface high order elevation maps with accommodation. Future work will also investigate the geometry of the lens as a function of aging and refractive errors.

Besides, recent work in the laboratory has demonstrated the use of OCT to reconstruct the Gradient Index distribution, and the change of GRIN with accommodation and aging.

## 7. RESUMEN EN ESPAÑOL

Esta tesis se centra en el estudio, por medio de varias técnicas *in vivo*, del proceso de acomodación del ojo humano, el cual permite enfocar en la retina objetos situados a distintas distancias. A pesar de que el mecanismo acomodativo ya fue ampliamente descrito por Helmholtz en 1855, existen todavía cuestiones por responder: un mejor conocimiento de la acomodación ayudará a desarrollar soluciones para algunos problemas visuales como, por ejemplo, la presbicia.

La presbicia es la pérdida gradual de la capacidad para enfocar objetos cercanos, debido a cambios fisiológicos del cristalino con la edad que empiezan a notarse a partir de los 45 años. Teniendo en cuenta que la esperanza de vida media en el mundo es actualmente de unos 70 años -unos diez años más en los países más desarrollados-, la presbicia es un gran problema de salud pública, al mismo tiempo que una gran oportunidad de negocio para las compañías oftálmicas. Actualmente se están investigando nuevas soluciones que buscan la restauración de la acomodación por medio de las denominadas lentes intraoculares acomodativas. Las primeras lentes ya se están comercializando, aunque la tecnología no se encuentra todavía en disposición de proporcionar resultados satisfactorios.

Por ello, es importante contar con técnicas fiables que permitan medir la respuesta acomodativa, la calidad óptica del ojo y las posibles interacciones entre ambas. Por un lado, nos permitirán conocer mejor el mecanismo de acomodación del ojo y servirnos de inspiración para esas nuevas soluciones que buscan restaurar la acomodación. Y por otro, servirán para evaluar de manera objetiva el funcionamiento de las nuevas lentes. Usando, por ejemplo, Óptica Adaptativa, una técnica que con la que se puede manipular y medir aberraciones ópticas de manera dinámica, seremos capaces de simular el efecto de potenciales diseños de lentes en la respuesta acomodativa. En esta tesis, se ha estudiado la influencia de las aberraciones de alto orden en la respuesta acomodativa haciendo uso tanto de Óptica Adaptativa como de imágenes degradadas computacionalmente.

Además, las técnicas de imagen que cuantifican la biometría y geometría del segmento anterior del ojo pueden proporcionar información de los cambios estructurales que sufre el cristalino durante la acomodación, relacionándolos con la respuesta acomodativa medida de manera objetiva gracias a otras técnicas. En esta tesis, hemos desarrollado un sistema de Tomografía de Coherencia Óptica (OCT) para visualizar en alta resolución y cuantificar la geometría del cristalino humano en función de la acomodación, tanto en tres dimensiones como de manera dinámica en una sección transversal.

## 7.1. Introducción

En la primera parte del capítulo de introducción (capítulo 1) se realiza una breve revisión del ojo humano, poniendo especial énfasis en sus elementos ópticos principales: la cornea y el cristalino. Éste último es el responsable directo de la acomodación: una lente biconvexa de potencia variable que posibilita enfocar en la retina objetos situados a diferentes distancias.

La calidad óptica del ojo humano juega un papel importante en la visión y es un aspecto muy relevante de esta tesis, ya que en ella se ha estudiado el impacto que tiene en el proceso acomodativo. Por ello se le dedica una amplia sección: desde los conceptos de aberraciones y de frente de onda (y su representación en la base de polinomios de Zernike), hasta las diversas métricas que se usan para evaluar la calidad de un sistema óptico, pasando por su medida con diferentes técnicas como, por ejemplo, el sensor de frente de onda Hartmann-Shack que será utilizado en esta tesis. También se describe el principio de funcionamiento y los componentes de un sistema de óptica adaptativa.

La sección central del capítulo describe el mecanismo de acomodación, analiza las diferentes técnicas existentes para su medida y detalla los cambios que ocurren con la acomodación, haciendo referencia a diversas fuentes. En primer lugar, los cambios del propio cristalino, tales como aumento de la curvatura de sus dos superficies y también de su espesor, así como otros cambios asociados a su estructura interna. Además, se indican otros cambios con la acomodación, algunos bien establecidos -como la disminución del diámetro pupilar- y otros todavía en discusión -como la evolución de las fluctuaciones de la respuesta acomodativa-. También se indican los datos existentes en la bibliografía científica sobre cambios de las distintas aberraciones con la acomodación, en particular la tendencia hacia valores más negativos de la aberración esférica, así como los escasos estudios que se han encontrado acerca de la relación entre aberraciones y retraso acomodativo.

Debido a que la causa de la pérdida de acomodación con la edad está en los cambios fisiológicos que sufre el cristalino al envejecer, una sección completa está dedicada a los mismos. En primer lugar, cambios puramente geométricos -como el aumento de su espesor o de la curvatura de sus superficies- o cambios en la distribución del índice de refracción que hacen que el cristalino sea menos potente con la edad a pesar de ser más curvo, en lo que se conoce como la *paradoja del cristalino*. Pero también otros cambios estructurales que hacen que el cristalino se endurezca y pierda transparencia con la edad. Dicho endurecimiento es el responsable de la pérdida de capacidad acomodativa o presbicia, mientras que la opacificación es la causante del problema visual denominado comúnmente cataratas, que termina por imposibilitar la visión y hace necesaria una intervención quirúrgica para sustituir el cristalino opaco por una lente intraocular transparente. Actualmente muchas compañías tratan de desarrollar lentes intraoculares acomodativas, que permitan restaurar dicha capacidad perdida con la edad. En esta sección se describen algunas de las propuestas actuales, su estado de desarrollo y algunos primeros resultados aún poco exitosos.

Por último, se hace un repaso de las principales técnicas que se utilizan para conocer la geometría del cristalino: ultrasonidos, métodos basados en imágenes de Purkinje, Resonancia Magnética, fotografía Scheimpflug y, más recientemente, Tomografía de Coherencia Óptica. Esta última ha sido utilizada en esta tesis para visualizar y cuantificar la geometría del cristalino durante la acomodación. Por ello, se describen con más detalle los principios de esta técnica interferométrica y las diferentes

modalidades existentes: OCT en dominio temporal y OCT en dominio frecuencial (ésta última a su vez con dos modalidades, espectral y swept source), indicando sus ventajas e inconvenientes. Asimismo, se expone brevemente el estado actual del OCT en el campo de la Oftalmología, en el que la técnica ha tenido un gran desarrollo por su capacidad para proporcionar imágenes en alta resolución de tejidos con haces de luz de baja intensidad. En un primer estadio su aplicación se centró en imagen retiniana, pero posteriormente se ha extendido también a la visualización del segmento anterior, como en el caso de esta tesis doctoral. No obstante, si además de visualizar las estructuras oculares se quiere obtener información cuantitativa de su geometría, es necesario corregir las imágenes de las diferentes distorsiones que las afectan.

### **7.1.1. Objetivos**

Los objetivos de esta tesis son:

- Investigar el efecto de la corrección o inducción de aberraciones de alto orden en la precisión de la respuesta acomodativa.
- Investigar el efecto de la corrección o inducción de aberraciones de alto orden en las fluctuaciones de dicha respuesta.
- Estudiar qué sucede si eliminamos la interacción óptica entre aberraciones y desenfoque y directamente emborronamos el estímulo acomodativo con aberraciones de alto orden.
- Demostrar la capacidad de la Tomografía de Coherencia Óptica para hacer imagen tridimensional del segmento anterior para diferentes estados acomodativos.
- Demostrar la capacidad de la Tomografía de Coherencia Óptica para hacer imágenes dinámicas del segmento anterior para diferentes estados acomodativos.
- Investigar la influencia de las aberraciones de alto orden en las fluctuaciones de la respuesta acomodativa

## **7.2. Métodos**

En el capítulo de métodos (Capítulo 2) se describen los tres sistemas que se han utilizado durante el transcurso de esta tesis doctoral.

En primer lugar, un sistema de Óptica Adaptativa desarrollado en el laboratorio de Óptica Visual y Biofotónica. Este sistema se compone principalmente de un diodo superluminiscente, un sistema de Badal motorizado que permite tanto corregir el error refractivo del sujeto como inducir demandas acomodativas, un espejo deformable que corrige/induce aberraciones, un sensor Hartmann-Shack de frente de onda para medir la respuesta acomodativa y las aberraciones y una pantalla en la que se proyecta el estímulo de fijación. El sistema cuenta también con un sistema de posicionamiento del sujeto en x-y-z y una cámara conjugada con la pupila para alinearla adecuadamente con el sistema.

En el capítulo se detallan las características de los diferentes componentes del sistema de óptica adaptativa indicados anteriormente, así como de las diferentes calibraciones y pruebas realizadas para garantizar la precisión y validez de los resultados. Así, se describe en primer lugar, la calibración del sistema de Badal, realizada por una parte colocando lentes de prueba de potencia conocida en el plano de pupila que compensen el desenfoque inducido y registrando la imagen; y posteriormente registrando el

desenfoque inducido con el sensor de frente de onda. También se describe el funcionamiento del sistema de óptica adaptativa, mostrándose la calibración del sensor de frente de onda a partir de la comparación con las aberraciones de ojo artificial con aberraciones conocidas, la estabilidad y planitud del espejo deformable y la capacidad de corrección de aberraciones del sistema. Y por último, se detalla los programas desarrollados en VisualC++.Net y VisualBasic.Net para el control y sincronización del sistema de Badal, el espejo deformable, el sensor de frente de onda y la cámara de pupila durante las sesiones experimentales.

El segundo sistema empleado es un retinoscopio dinámico que fue usado durante una estancia breve en el laboratorio de Philip B. Kruger en la Universidad Estatal de Nueva York (EEUU). El sistema permite la proyección de estímulos acomodativos cuya vergencia cambia dinámicamente siguiendo una dependencia sinusoidal. Monitorizando la respuesta acomodativa con el retinoscopio, se puede investigar la capacidad del sujeto para seguir dinámicamente este estímulo. Este sistema ha sido utilizado en el pasado para estudiar el papel de las aberraciones cromáticas como posible pista de la dirección de acomodación.

En el capítulo se describe brevemente el sistema, cuyos principales componentes son una pantalla de proyección del estímulo acomodativo, un sistema de Badal motorizado, un diafragma de 3 mm de diámetro y un retinoscopio que mide la respuesta acomodativa a 100 Hz.

El tercer y último sistema utilizado en esta tesis es un sistema de OCT espectral (en el dominio frecuencial). Este sistema fue desarrollado en colaboración con la Universidad Nicholas Copernicus, en Torun (Polonia). Para la realización de esta tesis, se incorporó al sistema original un canal para la estimulación de la acomodación.

En el capítulo se describe el funcionamiento y las diferentes partes del sistema de OCT. El sistema es básicamente un interferómetro en el que procedente de un diodo superluminiscente se divide en dos haces por acción de un divisor de fibra óptica: un haz de referencia que termina en un espejo y un haz objeto en el que dos espejos actúan como escáneres dirigiendo el haz de medida al ojo. La luz reflejada por el espejo del haz de referencia y por las estructuras del ojo es devuelta al divisor de fibra que las combina y envía a un sensor lineal que registra la interferencia. Realizando la Transformada de Fourier de la señal, se obtiene la información de la imagen de la muestra. Un elemento clave del sistema es el módulo piezoeléctrico pegado al espejo de referencia, que permite el desdoblamiento de la imagen para multiplicar por dos el rango de medida y evitar la ambigüedad asociada a la parte compleja de la transformada de Fourier.

Al final de esta sección se exponen también los resultados de las calibraciones del sistema de OCT y del módulo de Badal. Se indican también los programas utilizados para controlar el aparato y para procesar sus imágenes, además del programa desarrollado para controlar el sistema de Badal, análogo al utilizado en el sistema de Óptica Adaptativa.

## **7.3. Resultados**

### **7.3.1. Influencia de las aberraciones de alto orden en la acomodación**

En el capítulo 3 se estudia el impacto de las aberraciones de alto orden en la respuesta acomodativa y en las fluctuaciones de la acomodación. Para ello se realiza un experimento en cinco sujetos jóvenes en el que se estimula la acomodación con el

sistema de Badal desde 0D hasta 6D (en intervalos de 1D, durante 5 segundos para cada demanda) y se registra el frente de onda a 13 Hz para analizar la respuesta acomodativa. El experimento se realiza para cinco condiciones diferentes: (1) corrigiendo con el espejo sólo las aberraciones residuales del sistema, de manera que el sujeto observa el estímulo con sus aberraciones naturales; (2) corrigiendo las aberraciones del sujeto; (3) induciendo +1  $\mu\text{m}$  de aberración esférica en 6 mm de pupila; (3) induciendo -1  $\mu\text{m}$  de aberración esférica en 6 mm de pupila; e (3) induciendo +2  $\mu\text{m}$  de coma en 6 mm de pupila. Se realizan 5 sets de medidas, siempre con pupilas naturales (sin dilatación).

La respuesta acomodativa se calcula a partir de los coeficientes de Zernike de los términos de desenfoque y aberración esférica de cuarto y sexto orden, promediando los valores obtenidos durante los 5 segundos para cada demanda. Las fluctuaciones de la respuesta acomodativa se calculan obteniendo la desviación estadística de los valores durante los 5 segundos. Asimismo, se realiza un análisis frecuencial de la respuesta acomodativa. Por otro lado, la medida con el sensor de frente de ondas también nos permite calcular el cambio de las aberraciones de alto orden con la acomodación.

El resultado más relevante del estudio es que la precisión en la respuesta acomodativa mejora significativamente cuando las aberraciones de alto orden se corrigen mediante óptica adaptativa, mientras que empeora cuando se inducen aberraciones de alto orden. No obstante, la inducción de aberración esférica de signo negativo tiene un efecto positivo en la precisión acomodativa: esto se debe a que la contribución de la aberración esférica negativa se hace menor al reducirse la pupila con la acomodación, mejorando la precisión acomodativa.

Los resultados de las fluctuaciones de la acomodación muestran que éstas aumentan con el esfuerzo acomodativo. Aunque apenas existen diferencias significativas entre las distintas condiciones de aberración estudiadas, se observa que los valores de las fluctuaciones con respecto a la condición natural tienden a ser mayores cuando se inducen aberraciones y prácticamente iguales cuando son corregidas.

Otros resultados del estudio confirman la disminución del tamaño de la pupila y el cambio de la aberración esférica hacia valores más negativos al aumentar el esfuerzo acomodativo. En cambio, no se observan de cambios sistemáticos en otras aberraciones que sean comunes a todos los sujetos del estudio.

También se ha comparado el cálculo de la respuesta acomodativa a partir de los coeficientes de los términos de Zernike rotacionalmente simétricos (sólo desenfoque, desenfoque y aberración esférica de cuarto orden o incluyendo también hasta el término de esférica de sexto orden) con otra métrica que considera el desenfoque necesario para minimizar el volumen bajo la MTF (calculado a partir del frente de onda). Esta comparación muestra que es necesario considerar también los términos de aberración esférica de cuarto y sexto orden para tener un valor más preciso de la respuesta acomodativa calculada a partir de los coeficientes de Zernike.

### **7.3.2. Acomodación dinámica ante estímulos emborronados con aberraciones de alto orden**

En el capítulo 4 se ha estudiado el efecto en la precisión acomodativa de la presencia de aberraciones de alto orden haciendo uso de óptica adaptativa. Al inducir ópticamente las aberraciones, se permitía la interacción entre éstas y el desenfoque asociado a la demanda acomodativa. En este cuarto capítulo, en cambio, se presenta un estudio que

investiga el impacto en la acomodación dinámica de emborronar directamente el estímulo con las aberraciones. De esta manera, podemos analizar el efecto aislado que tiene la degradación del estímulo asociada a ciertos tipos y cantidades de aberraciones sobre la precisión de la respuesta acomodativa.

En el capítulo se detalla cómo se ha llevado a cabo este estudio. En primer lugar, se han generado los estímulos emborronados. Para ello, a partir de un código escrito en Matlab se han generado las funciones de esparcimiento de punto correspondientes a  $0.3\ \mu\text{m}$  y  $1\ \mu\text{m}$  (para una pupila de 3 mm) de desenfoque, coma vertical, trefoil vertical y aberración esférica, y se han convolucionado con el estímulo original.

El estudio se ha realizado en cinco sujetos que han visualizado cada uno de los nueve estímulos generados (el original y los ocho emborronados con aberraciones) con una vergencia que variaba sinusoidalmente entre 1D y 3D, a una frecuencia de 0.195 Hz y durante 40.96 segundos. La respuesta acomodativa se ha medido con un retinoscopio a 100 Hz. Para minimizar el efecto de las aberraciones propias del sujeto, se ha ubicado en el sistema un diafragma de 3 mm de diámetro conjugado con la pupila del sujeto.

Aplicando una Transformada de Fourier a cada respuesta temporal, se puede obtener la amplitud a la misma frecuencia de 0.195 Hz. De esta manera, se calcula la ganancia dinámica como el coeficiente entre la amplitud de la respuesta y la del estímulo y se compara este parámetro entre las distintas condiciones. También se puede calcular el retraso temporal existente la respuesta y el estímulo. Como condición para formar parte del estudio, era necesario que la amplitud de la respuesta acomodativa fuese al menos de 0.2 D; seis sujetos fueron descartado por no cumplir este requisito.

Los resultados muestran que la ganancia disminuye al emborronar los estímulos, de manera significativa cuando el emborronamiento se ha realizado con aberraciones de  $1\ \mu\text{m}$  (para 3 mm de pupila). El efecto es mayor para el desenfoque y la aberración esférica y menor para el trefoil.

Para cuantificar el distinto efecto que las diferentes aberraciones tienen sobre el emborronamiento del estímulo, se ha calculado para cada una de ellas el volumen bajo la MTF en el rango de 3-5 c/deg, el más relevante para la acomodación de acuerdo con Mathews y Kruger [1994]. Se ha encontrado una alta correlación entre el volumen bajo la MTF y los valores de la ganancia y del retraso acomodativo.

### **7.3.3. Geometría estática y dinámica del cristalino durante la acomodación usando tomografía de coherencia óptica tridimensional cuantitativa**

En el capítulo 5 se presenta un estudio que caracteriza la geometría del cristalino (radios de curvatura de las superficies anterior y posterior) para diferentes demandas acomodativas usando el sistema de OCT, con los algoritmos de corrección de distorsiones que permiten obtener valores cuantitativos. Los diferentes pasos en los que consiste el algoritmo de procesamiento de imágenes se describen en la sección de métodos.

En primer lugar, se tomaron imágenes tridimensionales del segmento anterior de cuatro sujetos jóvenes, de 0 a 6 D de demanda acomodativa en pasos de 1 D. En total se adquirieron 15 tandas de datos tridimensionales: 5 de la cornea, 5 de la superficie anterior del cristalino y 5 de la superficie posterior. Cada imagen cubría una zona de 6 mm (en horizontal) x 15 mm (en vertical) usando 40 B-scans y 600 A-scans, obtenidos en menos de 1 segundo para minimizar movimientos del sujeto durante la medida. Las

imágenes de la córnea y de la superficie anterior del cristalino se superpusieron usando el limbo como anclaje, mientras que las imágenes de las dos superficies del cristalino se superpusieron usando la pupila como referencia común.

En la segunda parte del trabajo, se adquirieron imágenes dinámicas a 14 Hz de la sección horizontal central en uno de los sujetos. El rango axial de imagen se aumentó gracias al módulo piezoeléctrico, con el objetivo de adquirir simultáneamente las superficies anterior y posterior del cristalino. Se tomaron una imagen tridimensional de la cornea y 5 sets de imágenes del meridiano central del cristalino (15 mm, 1668 A-scan) para cada demanda acomodativa (0 a 6 D, en pasos de 1 D).

A partir de las imágenes corregidas de ambos estudios, se obtuvieron los valores de los radios de curvatura del cristalino, de la posición de las superficies anterior y posterior y del espesor del cristalino y la profundidad de la cámara anterior con la demanda acomodativa. Con esos datos se estimó el cambio en la potencia del cristalino con la acomodación y, haciendo uso de un modelo de ojo esquemático y bajo la aproximación paraxial, se estimó la potencia total del ojo. También se estimaron las fluctuaciones de la acomodación a partir de las imágenes bidimensionales, estimando la contribución a dichas fluctuaciones de los cambios en los radios de curvatura del cristalino, en su espesor y en su posición media axial. Para ello se realizó un análisis de sensibilidad, variando cada magnitud y dejando constantes las demás.

Los resultados tridimensionales muestran que, como era de esperar, los radios de curvatura del cristalino disminuyen con la demanda acomodativa. También disminuye la profundidad de cámara anterior y el tamaño de la pupila, mientras que el espesor del cristalino aumenta.

A partir de los datos tridimensionales, la estimación del cambio en la potencia óptica del cristalino (promediada para los cuatro ojos) con la acomodación es de 0.82 dioptrías por dioptría de demanda acomodativa, mientras que el cambio en la potencia total del ojo es algo menor: 0.62 dioptrías por dioptría de demanda acomodativa. Los cálculos de las fluctuaciones de la acomodación apuntan en la misma dirección, ya que en promedio son 0.12 D menores cuando se considera la potencia total del ojo que cuando se estima la contribución aislada del cristalino. Además, las fluctuaciones aumentan con la demanda acomodativa, en 0.0044 D/D.

Por último, el análisis de sensibilidad de las fluctuaciones muestra que éstas están dominadas por la variabilidad de los radios de curvatura del cristalino, especialmente de la superficie posterior.

## **7.4. Conclusiones**

En esta tesis se han investigado varios aspectos del proceso de acomodación: se aborda la influencia de las aberraciones de orden alto en la precisión de la acomodación y de sus fluctuaciones, así como los cambios cuantitativos en la geometría del cristalino con la acomodación.

### **7.4.1. Logros**

En esta tesis se han alcanzado los siguientes logros:

- Desarrollo de un sistema AO para la manipulación de las aberraciones de alto orden y medición de la respuesta acomodativa, junto con un optómetro de Badal motorizado para estimular la acomodación.
- Por primera vez, se ha medido sistemáticamente la respuesta acomodativa en diferentes condiciones de aberración para estudiar la influencia de la calidad óptica en el retraso acomodativo.
- Se ha explorado el efecto sobre la acomodación de la aberración esférica de distinto signo inducida ópticamente.
- Se ha estudiado el impacto de sobre la acomodación dinámica del emborronamiento del estímulo acomodativo con aberraciones de alto orden.
- Por primera vez, se han obtenido imágenes cuantitativas tridimensionales del cristalino para un amplio rango de demandas acomodativas.
- También por primera vez, las diferentes aportaciones del cristalino a las fluctuaciones de la acomodación han sido exploradas.

#### 7.4.2. Conclusiones

1. La corrección de aberraciones de alto orden resulta en una mejor respuesta acomodativa, mientras que la inducción de aberraciones ópticas de alto orden empeora la precisión en la acomodación (Capítulo 3)
2. La presencia de una cantidad elevada de aberración esférica positiva es perjudicial para la respuesta acomodativa: no sólo emborrona el estímulo, sino que el efecto combinado de la disminución de tamaño de la pupila con el esfuerzo acomodativo afecta negativamente a la precisión acomodativa. En cambio, la presencia de aberración esférica negativa disminuye el retraso acomodativo (capítulo 3).
3. Para estimar con precisión la respuesta acomodativa a partir de las aberraciones es necesario tener en cuenta no sólo el desenfoque, sino también los términos de aberración esférica de cuarto y sexto orden (Capítulo 3).
4. El emborronamiento del estímulo acomodativo con aberraciones de alto orden afecta a la acomodación dinámica, de forma proporcional al emborronamiento. Los efectos sólo son significativos para valores de las aberraciones más altos que los valores típicos (capítulo 4).
5. La disminución en la ganancia de la acomodación dinámica está correlacionado con el valor de la MTF para las frecuencias relevantes para la acomodación (capítulo 4).
6. La disminución de la respuesta acomodativa en presencia de aberraciones de alto orden es, en parte, debida a una mayor tolerancia al emborronamiento (capítulo 4).
7. Las fluctuaciones de la acomodación aumentan sistemáticamente con la respuesta acomodativa entre 0 y 6 dioptrías de demanda acomodativa. Este resultado se ha obtenido de forma independiente en dos estudios distintos. El aumento de las fluctuaciones es de 0.049 dioptrías por dioptría de esfuerzo acomodativo en el estudio de AO (Capítulo 3) y de 0.044 dioptrías por dioptría de demanda acomodativa en el estudio con OCT (capítulo 5).
8. Las fluctuaciones de la acomodación tienden a ser mayores en presencia de grandes valores de aberraciones de alto orden, que pueden estar asociados a la mayor profundidad de enfoque (Capítulo 3).
9. De acuerdo con un análisis de sensibilidad, las fluctuaciones de la acomodación son debidas principalmente a los cambios dinámicos en las superficies del

- cristalino, especialmente a cambios en el radio de curvatura de su superficie posterior (capítulo 5).
10. La Tomografía de Coherencia Óptica en el dominio frecuencial con alta velocidad y alta resolución -y provista de algoritmos de corrección de la distorsión- permite obtener imágenes cuantitativas tanto estáticas en 3-D como dinámicas en 2-D del cristalino durante la acomodación. La técnica permite evaluar los cambios en los radios de curvatura y la posición de las superficies del cristalino (capítulo 5).
  11. Usando imágenes tridimensionales de OCT, hemos encontrado radios promedio entre cuatro sujetos jóvenes del cristalino desacomodado de  $12.90 \pm 0.64$  mm para la superficie anterior y  $6.20 \pm 0.59$  mm para la superficie posterior. Los radios de curvatura disminuyen en valor absoluto con la demanda acomodativa (entre 0 y 6 D): el radio anterior en 0.73 mm/D y el posterior, en 0.20 mm/D.
  12. Las imágenes de TCO también han permitido reportar cambios biométricos con la demanda acomodativa de -0.057 mm/D en la profundidad de la cámara anterior y 0.081 mm/D en el espesor de la lente.

### 7.4.3. Trabajo futuro

En esta tesis, se han utilizado un sistema de Óptica Adaptativa y un sistema de OCT en el dominio espectral para explorar diferentes aspectos del mecanismo de acomodación. La utilización independiente o combinada de estas dos técnicas de gran alcance puede proporcionar nuevos conocimientos sobre la acomodación. La Óptica Adaptativa permite la corrección y la inducción de aberraciones, lo que posibilita la simulación de diferentes correcciones y el estudio de la percepción visual, la función visual y la adaptación neuronal a las mismas. Las posibilidades de simulación son múltiples e incluyen, por ejemplo, lentes intraoculares esféricas, correcciones multifocales y aberraciones de otros sujetos.

El OCT cuantitativo es también una excelente herramienta para la evaluación del funcionamiento de las lentes intraoculares *premium*, tales como lentes intraoculares acomodativas. Además, la biometría 3D basada en OCT previa a la cirugía permitirá la selección más precisa de lentes intraoculares, a partir del trazado de rayos en los modelos de ojo personalizados a la anatomía del paciente.

Las capacidades cuantitativas del OCT se pueden ampliar para caracterizar completamente el cristalino, más allá de los radios de curvatura y de las distancias axiales. Actualmente se están llevando a cabo estudios para determinar la topografía de ambas superficies del cristalino, tanto *in vivo* como *ex vivo*, incluyendo cambios en los mapas de aberraciones con la acomodación. En un futuro próximo, también se investigará la geometría de la lente en función de la edad y los defectos de refracción.

Además, un trabajo reciente ha hecho uso del mismo sistema de OCT para reconstruir la distribución de gradiente de índice del cristalino, y el cambio de la misma con la acomodación y el envejecimiento.

## 8. BIBLIOGRAPHY

### A

- Aggarwala, K. R., Kruger, E. S., Mathews, S., & Kruger, P. B. (1995). Spectral bandwidth and ocular accommodation. *JOSA A*, *12*(3), 450–455.
- Aggarwala, K. R., Nowbotsing, S., & Kruger, P. B. (1995). Accommodation to monochromatic and white-light targets. *Investigative Ophthalmology and Visual Science*, *36*(13), 2695–2705.
- Aldaba, M., Vilaseca, M., Díaz-Doutón, F., Arjona, M., & Pujol, J. (2012). Measuring the accommodative response with a double-pass system: comparison with the Hartmann-Shack technique. *Vision research*, *62*, 26-34.
- Alpern, M. (1958). Variability of accommodation during steady fixation at various levels of illuminance. *JOSA*, *48*(3), 193-197.
- Alpern, M., Mason, G. L., & Jardinico, R. E. (1961). Vergence and accommodation. V. Pupil size changes associated with changes in accommodative vergence. *American Journal of Ophthalmology*, *52*(2), 762-767.
- Applegate, R. A., Marsack, J. D., Ramos, R., & Sarver, E. J. (2003a). Interaction between aberrations to improve or reduce visual performance. *Journal of Cataract & Refractive Surgery*, *29*(8), 1487-1495.
- Applegate, R. A., Ballentine, C., Gross, H., Sarver, E. J., & Sarver, C. A. (2003b). Visual acuity as a function of Zernike mode and level of root mean square error. *Optometry and Vision Science*, *80*(2), 97–105.
- Artal, P., Marcos, S., Navarro, R., & Williams, D. R. (1995). Odd aberrations and double-pass measurements of retinal image quality. *JOSA A*, *12*(2), 195-201.
- Artal, P., Santamaría, J., & Bescós, J. (1988). Retrieval of wave aberration of human eyes from actual point-spread-function data. *JOSA A*, *5*(8), 1201-1206.
- Artal, P., Berrio, E., Guirao, A., & Piers, P. (2002). Contribution of the cornea and internal surfaces to the change of ocular aberrations with age. *JOSA A*, *19*(1), 137-143.
- Atchison, D. A., Collins, M. J., Wildsoet, C. F., Christensen, J., & Waterworth, M. D. (1995). Measurement of monochromatic ocular aberrations of human eyes as a function of accommodation by the Howland aberroscope technique. *Vision Research*, *35*(3), 313-323.
- Atchison, D. A., Smith, G., & Smith, G. (2000). *Optics of the human eye*. (Butterworth-Heinemann, Oxford).
- Atchison, D. A. (2004). Recent advances in representation of monochromatic aberrations of human eyes. *Clinical and Experimental Optometry*, *87*(3), 138-148.
- Atchison, D. A., Markwell, E. L., Kasthurirangan, S., Pope, J. M., Smith, G., & Swann, P. G. (2008). Age-related changes in optical and biometric characteristics of emmetropic eyes. *Journal of vision*, *8*(4), 29.

Augusteyn, R. C., Jones, C. E., & Pope, J. M. (2008). Age-related development of a refractive index plateau in the human lens: evidence for a distinct nucleus. *Clinical and Experimental Optometry*, 91(3), 296-301.

Avila, M., Li, Y., Song, J. C., & Huang, D. (2006). High-speed optical coherence tomography for management after laser in situ keratomileusis. *Journal of Cataract & Refractive Surgery*, 32(11), 1836-1842.

## **B**

Barbero, S., Marcos, S., Merayo-Llodes, J., & Moreno Barriuso, E. (2002). Validation of the estimation of corneal aberrations from videokeratography in keratoconus. *Journal of Refractive Surgery*, 18(3), 263-270.

Barbero, S. (2006). Refractive power of a multilayer rotationally symmetric model of the human cornea and tear film. *JOSA A*, 23(7), 1578-1585.

Beers, A. P. A., & Van Der Heijde, G. L. (1994a). In vivo determination of the biomechanical properties of the component elements of the accommodation mechanism. *Vision research*, 34(21), 2897-2905.

Beers, A. P. A., & Van der Heijde, G. L. (1994b). Presbyopia and velocity of sound in the lens. *Optometry & Vision Science*, 71(4), 250-253.

Birkenfeld, J., De Castro, A., Ortiz, S., Pascual, D., & Marcos, S. (2013). Contribution of the gradient refractive index and shape to the crystalline lens spherical aberration and astigmatism. *Vision research*, 86, 27-34.

Birkenfeld, J., de Castro, A., & Marcos, S. (2014). Contribution of shape and gradient refractive index to the spherical aberration of isolated human lenses. *Investigative ophthalmology & visual science*, 55(4), 2599-2607.

Bolz, M., Prinz, A., Drexler, W., & Findl, O. (2007). Linear relationship of refractive and biometric lenticular changes during accommodation in emmetropic and myopic eyes. *British journal of ophthalmology*, 91(3), 360-365.

Borja, D., Manns, F., Ho, A., Ziebarth, N., Rosen, A. M., Jain, R., Amelinckx, A., Arrieta, E., Augusteyn, R. C. & Parel, J. M. (2008). Optical power of the isolated human crystalline lens. *Investigative ophthalmology & visual science*, 49(6), 2541-2548.

Brown, N. (1973). The change in shape and internal form of the lens of the eye on accommodation. *Experimental eye research*, 15(4), 441-459.

Brown, N. (1974). The change in lens curvature with age. *Experimental eye research*, 19(2), 175-183.

## **C**

Campbell, C. (1997). Reconstruction of the corneal shape with the MasterVue Corneal Topography System. *Optometry & Vision Science*, 74(11), 899-905.

Campbell, F. W., & Westheimer, G. (1959). Factors influencing accommodation responses of the human eye. *OSA*, 49(6), 568-571.

Campbell, F. W., & Gregory, A. H. (1960). Effect of size of pupil on visual acuity.

- Campbell, F. W., & Gubisch, R. W. (1966). Optical quality of the human eye. *The Journal of Physiology*, 186(3), 558–578.
- Carkeet, A., Luo, H.D., Tong, L., Saw, S.M., & Tan, D.T.H. (2002). Refractive error and monochromatic aberrations in Singaporean children. *Vision Research*, 42(14), 1809-1824.
- Castejon-Mochon, J. F., López-Gil, N., Benito, A., & Artal, P. (2002). Ocular wave-front aberration statistics in a normal young population. *Vision research*, 42(13), 1611-1617.
- Charman, W. N., & Tucker, J. (1977). Dependence of accommodation response on the spatial frequency spectrum of the observed object. *Vision Research*, 17(1), 129–139.
- Charman, W. N., & Tucker, J. (1978). Accommodation and color. *JOSA*, 68(4), 459-471.
- Charman, W. N., & Heron, G. (1988). Fluctuations in accommodation: a review. *Ophthalmic and Physiological Optics*, 8(2), 153-164.
- Charman, W. N. (1991). *Visual optics and instrumentation* (Vol. 1). CRC Press.
- Charman, W. N., & Radhakrishnan, H. (2009). Accommodation, pupil diameter and myopia. *Ophthalmic and Physiological Optics*, 29(1), 72-79.
- Chen, L., Singer, B., Guirao, A., Porter, J. and Williams, D. R. (2005). Image metrics for predicting subjective image quality. *Optometry & Vision Science*, 82(5), 358-369.
- Chen, L., Kruger, P. B., Hofer, H., Singer, B., & Williams, D. R. (2006). Accommodation with higher-order monochromatic aberrations corrected with adaptive optics. *Journal of the Optical Society of America A*, 23(1), 1–8.
- Cheng, H., Barnett, J. K., Vilupuru, A. S., Marsack, J. D., Kasthurirangan, S., Applegate, R. A., & Roorda, A. (2004). A population study on changes in wave aberrations with accommodation. *Journal of Vision*, 4(4), 3.
- Cheng, X., Bradley, A., Hong, X., & Thibos, L. N. (2003). Relationship between refractive error and monochromatic aberrations of the eye. *Optometry & Vision Science*, 80(1), 43-49.
- Cheng, X., Bradley, A., & Thibos, L. N. (2004). Predicting subjective judgment of best focus with objective image quality metrics. *Journal of Vision*, 4(4), 7.
- Chinn, S. R., Swanson, E. A., & Fujimoto, J. G. (1997). Optical coherence tomography using a frequency-tunable optical source. *Optics letters*, 22(5), 340-342.
- Choma, M., Sarunic, M., Yang, C., & Izatt, J. (2003). Sensitivity advantage of swept source and Fourier domain optical coherence tomography. *Optics Express*, 11(18), 2183-2189.
- Choma, M. A., Hsu, K., & Izatt, J. A. (2005). Swept source optical coherence tomography using an all-fiber 1300-nm ring laser source. *Journal of biomedical optics*, 10(4), 044009.
- Collins, M., Davis, B., & Wood, J. (1995a). Microfluctuations of steady-state accommodation and the cardiopulmonary system. *Vision research*, 35(17), 2491-2502.
- Collins, M. J., Wildsoet, C. F., & Atchison, D. A. (1995b). Monochromatic aberrations and myopia. *Vision research*, 35(9), 1157-1163.

Collins, M.J., Goode, A.S., & Atchison, D.A. (1997). Accommodation and spherical aberration. *COE abstract*.

## D

Dai, C., Zhou, C., Fan, S., Chen, Z., Chai, X., Ren, Q., & Jiao, S. (2012). Optical coherence tomography for whole eye segment imaging. *Optics express*, 20(6), 6109-6115.

de Boer, J. F., Cense, B., Park, B. H., Pierce, M. C., Tearney, G. J., & Bouma, B. E. (2003). Improved signal-to-noise ratio in spectral-domain compared with time-domain optical coherence tomography. *Optics letters*, 28(21), 2067-2069.

de Castro, A., Siedlecki, D., Borja, D., Uhlhorn, S., Parel, J. M., Manns, F., & Marcos, S. (2011). Age-dependent variation of the gradient index profile in human crystalline lenses. *Journal of modern optics*, 58(19-20), 1781-1787.

de Castro, A., Birkenfeld, J., Maceo, B., Manns, F., Arrieta, E., Parel, J. M., & Marcos, S. (2013). Influence of shape and gradient refractive index in the accommodative changes of spherical aberration in nonhuman primate crystalline lenses. *Investigative ophthalmology & visual science*, 54(9), 6197-6207.

de la Cera, E. G., Rodríguez, G., De Castro, A., Merayo, J., & Marcos, S. (2007). Emmetropization and optical aberrations in a myopic corneal refractive surgery chick model. *Vision research*, 47(18), 2465-2472.

Delori, F. C., Webb, R. H., & Sliney, D. H. (2007). Maximum permissible exposures for ocular safety (ANSI 2000), with emphasis on ophthalmic devices. *JOSA A*, 24(5), 1250-1265.

Drexler, W., Baumgartner, A., Findl, O., Hitzenberger, C., Sattmann, H., & Fercher, A. (1997). Submicrometer precision biometry of the anterior segment of the human eye. *Invest. Ophthalmol. Vis. Science*, 38(7), 1304-1313

Drexler, W., Findl, O., Schmetterer, L., Hitzenberger, C. K., & Fercher, A. F. (1998). Eye elongation during accommodation in humans: differences between emmetropes and myopes. *Investigative ophthalmology & visual science*, 39(11), 2140-2147.

Du, C., Shen, M., Li, M., Zhu, D., Wang, M. R., & Wang, J. (2012). Anterior segment biometry during accommodation imaged with ultralong scan depth optical coherence tomography. *Ophthalmology*, 119(12), 2479-2485.

Dubbelman, M., & Van der Heijde, G. L. (2001a). The shape of the aging human lens: curvature, equivalent refractive index and the lens paradox. *Vision research*, 41(14), 1867-1877.

Dubbelman, M., & Van der Heijde, G. L. (2001b). The shape of the aging human lens: curvature, equivalent refractive index and the lens paradox. *Vision research*, 41(14), 1867-1877.

Dubbelman, M., Van der Heijde, G. L., & Weeber, H. A. (2001). The thickness of the aging human lens obtained from corrected Scheimpflug images. *Optometry & Vision Science*, 78(6), 411-416.

Dubbelman, M., Weeber, H. A., Van Der Heijde, R. G., & Völker-Dieben, H. J. (2002). Radius and asphericity of the posterior corneal surface determined by corrected Scheimpflug photography. *Acta Ophthalmologica Scandinavica*, 80(4), 379-383.

Dubbelman, M., Van der Heijde, G. L., & Weeber, H. A. (2005). Change in shape of the aging human crystalline lens with accommodation. *Vision research*, 45(1), 117-132.

Dubbelman, M., Sicam, V. A. D. P., & Van der Heijde, G. L. (2006). The shape of the anterior and posterior surface of the aging human cornea. *Vision research*, 46(6), 993-1001.

Dunne, M., Royston, J. M., & Barnes, D. A. (1992). Normal variations of the posterior corneal surface. *Acta ophthalmologica*, 70(2), 255-261.

Dunne, M. C., Davies, L. N., & Wolffsohn, J. S. (2007). Accuracy of cornea and lens biometry using anterior segment optical coherence tomography. *Journal of biomedical optics*, 12(6), 064023.

## E

Edmund, C. (1994). Posterior corneal curvature and its influence on corneal dioptric power. *Acta ophthalmologica*, 72(6), 715-720.

## F

Fercher, A. F., Mengedoht, K., & Werner, W. (1988). Eye-length measurement by interferometry with partially coherent light. *Optics letters*, 13(3), 186-188.

Fercher, A. F., Hitzengerger, C. K., Drexler, W., Kamp, G., & Sattmann, H. (1993) In vivo optical coherence tomography. *American Journal of Ophthalmology*, 116(1), 113-114.

Fernandez, E. J., & Artal, P. (2005). Study on the effects of monochromatic aberrations in the accommodation response by using adaptive optics. *JOSA A*, 22(9), 1732-1738.

Fernandez, E. J., Vabre, L., Hermann, B., Unterhuber, A., Povazay, B., & Drexler, W. (2006). Adaptive optics with a magnetic deformable mirror: applications in the human eye. *Optics Express*, 14(20), 8900-8917.

Fincham, E. F. (1951). The accommodation reflex and its stimulus. *British Journal of Ophthalmology*, 35(7), 381-393.

Fisher, R. F. (1971). The elastic constants of the human lens. *The Journal of Physiology*, 212(1), 147-180.

Fisher, R. F. (1977). The force of contraction of the human ciliary muscle during accommodation. *The Journal of physiology*, 270(1), 51-74.

Fry, G. A. (1955). *Blur of the Retinal Image* (The Ohio State University Press, Columbus)

Furukawa, H., Hiro-Oka, H., Satoh, N., Yoshimura, R., Choi, D., Nakanishi, M., Igarashi, A., Ishikawa, H., Ohbayashi, K., & Shimizu, K. (2010). Full-range imaging of eye accommodation by high-speed long-depth range optical frequency domain imaging. *Biomedical optics express*, 1(5), 1491-1501.

## G

- García de la Cera, E., Rodríguez, G., De Castro, A., Merayo, J., & Marcos, S. (2007). Emmetropization and optical aberrations in a myopic corneal refractive surgery chick model. *Vision research*, 47(18), 2465-2472.
- Garner, L. F., & Smith, G. (1997). Changes in equivalent and gradient refractive index of the crystalline lens with accommodation. *Optometry & Vision Science*, 74(2), 114-119.
- Garner, L. F., & Yap, M. K. (1997). Changes in ocular dimensions and refraction with accommodation. *Ophthalmic and Physiological Optics*, 17(1), 12-17.
- Garner, L. F., Ooi, C. S., & Smith, G. (1998). Refractive index of the crystalline lens in young and aged eyes. *Clinical and Experimental Optometry*, 81(4), 145-150.
- Glasser, A., & Campbell, M. C. (1998). Presbyopia and the optical changes in the human crystalline lens with age. *Vision research*, 38(2), 209-229.
- Glasser, A., & Campbell, M. C. (1999). Biometric, optical and physical changes in the isolated human crystalline lens with age in relation to presbyopia. *Vision research*, 39(11), 1991-2015.
- Glasser, A., Wendt, M., & Ostrin, L. (2006). Accommodative changes in lens diameter in rhesus monkeys. *Investigative ophthalmology & visual science*, 47(1), 278-286.
- Gold, D. H., & Lewis, R. A. (2011). Clinical eye atlas. Oxford University Press.
- Goldsmith, J. A., Li, Y., Chalita, M. R., Westphal, V., Patil, C. A., Rollins, A. M., Izatt, J. A & Huang, D. (2005). Anterior chamber width measurement by high-speed optical coherence tomography. *Ophthalmology*, 112(2), 238-244.
- Gora, M., Karnowski, K., Szkulmowski, M., Kaluzny, B. J., Huber, R., Kowalczyk, A., & Wojtkowski, M. (2009). Ultra high-speed swept source OCT imaging of the anterior segment of human eye at 200 kHz with adjustable imaging range. *Optics Express*, 17(17), 14880-14894.
- Gray, L. S., Winn, B., & Gilmartin, B. (1993a). Accommodative microfluctuations and pupil diameter. *Vision research*, 33(15), 2083-2090.
- Gray, L. S., Winn, B., & Gilmartin, B. (1993b). Effect of target luminance on microfluctuations of accommodation. *Ophthalmic and Physiological Optics*, 13(3), 258-265.
- Grulkowski, I., Gora, M., Szkulmowski, M., Gorczynska, I., Szlag, D., Marcos, S., Kowalczyk, A. & Wojtkowski, M. (2009). Anterior segment imaging with Spectral OCT system using a high-speed CMOS camera. *Optics express*, 17(6), 4842-4858.
- Grulkowski, I., Liu, J. J., Potsaid, B., Jayaraman, V., Lu, C. D., Jiang, J., Cable, A. E. , Duker, J. S. & Fujimoto, J. G. (2012). Retinal, anterior segment and full eye imaging using ultrahigh speed swept source OCT with vertical-cavity surface emitting lasers. *Biomedical optics express*, 3(11), 2733-2751.
- Guirao, A., & Williams, D. R. (2003). A method to predict refractive errors from wave aberration data. *Optometry & Vision Science*, 80(1), 36-42.

Gwiazda, J., Thorn, F., Bauer, J., & Held, R. (1993). Myopic children show insufficient accommodative response to blur. *Investigative ophthalmology & visual science*, 34(3), 690-694.

## H

Hampson, K. M., Paterson, C., Dainty, C., & Mallen, E. A. (2006). Adaptive optics system for investigation of the effect of the aberration dynamics of the human eye on steady-state accommodation control. *JOSA A*, 23(5), 1082-1088.

Harb, E., Thorn, F., & Troilo, D. (2006). Characteristics of accommodative behavior during sustained reading in emmetropes and myopes. *Vision research*, 46(16), 2581-2592.

Hartwig, A., & Atchison, D. A. (2012). Analysis of higher-order aberrations in a large clinical population. *Investigative ophthalmology & visual science*, 53(12), 7862-7870.

Häusler, G., & Lindner, M. W. (1998). “Coherence radar” and “spectral radar”—new tools for dermatological diagnosis. *Journal of biomedical optics*, 3(1), 21-31.

He, J. C., Burns, S. A., & Marcos, S. (2000). Monochromatic aberrations in the accommodated human eye. *Vision Research*, 40(1), 41-48.

He, J. C., Sun, P., Held, R., Thorn, F., Sun, X., & Gwiazda, J. E. (2002). Wavefront aberrations in eyes of emmetropic and moderately myopic school children and young adults. *Vision research*, 42(8), 1063-1070.

He, J. C., Gwiazda, J., Thorn, F., Held, R., & Vera-Diaz, F. A. (2005). The association of wavefront aberration and accommodative lag in myopes. *Vision research*, 45(3), 285-290.

Hee, M. R., Puliafito, C. A., Wong, C., Duker, J. S., Reichel, E., Schuman, J. S., Swanson, E. A. & Fujimoto, J. G. (1995). Optical coherence tomography of macular holes. *Ophthalmology*, 102(5), 748-756.

Hee, M. R., Baumal, C. R., Puliafito, C. A., Duker, J. S., Reichel, E., Wilkins, J. R., Coker, J. G., Schuman, J. S., Swanson, E. A. & Fujimoto, J. G. (1996). Optical coherence tomography of age-related macular degeneration and choroidal neovascularization. *Ophthalmology*, 103(8), 1260-1270.

Hee, M. R., Puliafito, C. A., Duker, J. S., Reichel, E., Coker, J. G., Wilkins, J. R., Schuman, J. S., Swanson, E. A. & Fujimoto, J. G. (1998). Topography of diabetic macular edema with optical coherence tomography. *Ophthalmology*, 105(2), 360-370.

Helmholtz, H. V. (1885) Popular lectures on scientific subjects. New York, Appleton.

Hemenger, R. P., Garner, L. F., & Ooi, C. S. (1995). Change with age of the refractive index gradient of the human ocular lens. *Investigative ophthalmology & visual science*, 36(3), 703-707.

Hermans, E. A., Dubbelman, M., van der Heijde, R. G. L., & Heethaar, R. M. (2008). Equivalent refractive index of the human lens upon accommodative response. *Optometry and Vision Science*, 85(12), 1179-1184.

Hofer, H., Artal, P., Singer, B., Aragón, J. L., & Williams, D. R. (2001). Dynamics of the eye's wave aberration. *JOSA A*, 18(3), 497-506.

Hoffer, K. J. (1993). Axial dimension of the human cataractous lens. *Archives of ophthalmology*, 111(7), 914-918.

Hosny, M., Alio, J. L., Claramonte, P., Attia, W. H., & Perez-Santonja, J. J. (2000). Relationship between anterior chamber depth, refractive state, corneal diameter, and axial length. *Journal of Refractive Surgery*, 16(3), 336-340.

Howland, H. C. (1985). Optics of photoretinoscopy: results from ray tracing. *American journal of optometry and physiological optics*, 62(9), 621-625.

Huang, D., Swanson, E. A., Lin, C. P., Schuman, J. S., Stinson, W. G., Chang, W., ... & Puliafito, C. A. (1991). Optical coherence tomography. *Science*, 254(5035), 1178-1181.

## I

Izatt, J. A., Hee, M. R., Swanson, E. A., Lin, C. P., Huang, D., Schuman, J. S., Puliafito, C. A., & Fujimoto, J. G. (1994). Micrometer-scale resolution imaging of the anterior eye in vivo with optical coherence tomography. *Archives of ophthalmology*, 112(12), 1584-1589.

## J

Jones, C. E., Atchison, D. A., Meder, R., & Pope, J. M. (2005). Refractive index distribution and optical properties of the isolated human lens measured using magnetic resonance imaging (MRI). *Vision research*, 45(18), 2352-2366.

## K

Karnowski, K., Kaluzny, B. J., Szkulmowski, M., Gora, M., & Wojtkowski, M. (2011). Corneal topography with high-speed swept source OCT in clinical examination. *Biomedical optics express*, 2(9), 2709-2720.

Kasthurirangan, S., & Glasser, A. (2005). Characteristics of pupil responses during far-to-near and near-to-far accommodation. *Ophthalmic and Physiological Optics*, 25(4), 328-339.

Kasthurirangan, S., Markwell, E. L., Atchison, D. A., & Pope, J. M. (2011). MRI study of the changes in crystalline lens shape with accommodation and aging in humans. *Journal of vision*, 11(3), 19.

Katz M. & Kruger, P. B. (2009). The human eye as an optical system. Cap. 33, Vol I of W. Tasman y E. Jaeger, (eds). *Duane's Ophthalmology*. 15<sup>a</sup> ed. Philadelphia, Pa: Lippincott Williams & Wilkins.

Kaufman, H.E., Barron, B.A., & McDonald, M.B. (1998.) The cornea. Butterworth-Heinemann, Newton.

Khurana, R. N., Li, Y., Tang, M., Lai, M. M., & Huang, D. (2007). High-speed optical coherence tomography of corneal opacities. *Ophthalmology*, 114(7), 1278-1285.

Koeppl, C., Findl, O., Menapace, R., Kriechbaum, K., Wirtitsch, M., Buehl, W., Sacu, S., & Drexler, W. (2005). Pilocarpine-induced shift of an accommodating intraocular lens: AT-45 Crystalens. *Journal of Cataract & Refractive Surgery*, 31(7), 1290-1297.

- Koretz, J. F., Handelman, G. H., & Brown, N. P. (1984). Analysis of human crystalline lens curvature as a function of accommodative state and age. *Vision research*, 24(10), 1141-1151.
- Koretz, J. F., & Handelman, G. H. (1986). Modeling age-related accommodative loss in the human eye. *Mathematical Modelling*, 7(5), 1003-1014.
- Koretz, J. F., Cook, C. A., & Kuszak, J. R. (1994). The zones of discontinuity in the human lens: development and distribution with age. *Vision research*, 34(22), 2955-2962.
- Koretz, J. F., Cook, C. A., & Kaufman, P. L. (1997). Accommodation and presbyopia in the human eye. Changes in the anterior segment and crystalline lens with focus. *Investigative ophthalmology & visual science*, 38(3), 569-578.
- Koretz, J. F., Cook, C. A., & Kaufman, P. L. (2001). Aging of the human lens: changes in lens shape at zero-diopter accommodation. *JOSA A*, 18(2), 265-272.
- Koretz, J. F., Strenk, S. A., Strenk, L. M., & Semmlow, J. L. (2004). Scheimpflug and high-resolution magnetic resonance imaging of the anterior segment: a comparative study. *JOSA A*, 21(3), 346-354.
- Kotulak, J. C., & Schor, C. M. (1986a). A computational model of the error detector of human visual accommodation. *Biological cybernetics*, 54(3), 189-194.
- Kotulak, J. C., & Schor, C. M. (1986b). Temporal variations in accommodation during steady-state conditions. *JOSA A*, 3(2), 223-227.
- Kotulak, J. C., Morse, S. E., & Billock, V. A. (1995). Red-green opponent channel mediation of control of human ocular accommodation. *The Journal of physiology*, 482(3), 697-703.
- Krag, S., Olsen, T., & Andreassen, T. T. (1997). Biomechanical characteristics of the human anterior lens capsule in relation to age. *Investigative Ophthalmology & Visual Science*, 38(2), 357-363.
- Kruger, P. B. (1979). Infrared recording retinoscope for monitoring accommodation. *American Journal of Optometry and Physiological Optics*, 56(2), 116-123.
- Kruger, P. B., & Pola, J. (1986). *Stimuli for accommodation: Blur, chromatic aberration and size*. *Vision Research*, 26(6), 957-971.
- Kruger, P. B., Mathews, S., Aggarwala, K. R., & Sanchez, N. (1993). Chromatic aberration and ocular focus: Fincham revisited. *Vision Research*, 33(10), 1397-1411.
- Kruger, P. B., Nowbotsing, S., Aggarwala, K. R., & Mathews, S. (1995). Small amounts of chromatic aberration influence dynamic accommodation. *Optometry and Vision Science*, 72(17), 656-666.
- Kruger, P. B., Aggarwala, K. R., Bean, S., & Mathews, S. (1997). *Accommodation to stationary and moving targets*. *Optometry and Vision Science*, 74(7), 505-510.
- Kruger, P. B., López-Gil, N., & Stark, L. R. (2001). Accommodation and the Stiles-Crawford effect: theory and a case study. *Ophthalmic and Physiological Optics*, 21(5), 339-351.
- Kruger, P. B., Stark, L. R., & Nguyen, H. N. (2004). Small foveal targets for studies of accommodation and the Stiles-Crawford effect. *Vision Research*, 44(24), 2757-2767.

Kubo, E., Kumamoto, Y., Tsuzuki, S., & Akagi, Y. (2006). Axial length, myopia, and the severity of lens opacity at the time of cataract surgery. *Archives of ophthalmology*, 124(11), 1586-1590.

## L

Lai, M. M., Tang, M., Andrade, E. M., Li, Y., Khurana, R. N., Song, J. C., & Huang, D. (2006). Optical coherence tomography to assess intrastromal corneal ring segment depth in keratoconic eyes. *Journal of Cataract & Refractive Surgery*, 32(11), 1860-1865.

Lam, A. K., & Douthwaite, W. A. (1997). Measurement of posterior corneal asphericity on Hong Kong Chinese: A pilot study. *Ophthalmic and Physiological Optics*, 17(4), 348-356.

Lee, J. H., Stark, L. R., Cohen, S., & Kruger, P. B. (1999). Accommodation to static chromatic simulations of blurred retinal images. *Ophthalmic and Physiological Optics*, 19(3), 223-235.

Leibowitz, H. W., & Owens, D. A. (1975). Anomalous myopias and the intermediate dark focus of accommodation. *Science*, 189(4203), 646-648.

Leibowitz, H. W., & Owens, D. A. (1978). New evidence for the intermediate position of relaxed accommodation. *Documenta Ophthalmologica*, 46(1), 133-147.

Li, Y., Shekhar, R., & Huang, D. (2006). Corneal pachymetry mapping with high-speed optical coherence tomography. *Ophthalmology*, 113(5), 792-799.

Li, Y., Meisler, D. M., Tang, M., Lu, A. T., Thakrar, V., Reiser, B. J., & Huang, D. (2008). Keratoconus diagnosis with optical coherence tomography pachymetry mapping. *Ophthalmology*, 115(12), 2159-2166.

Liang, J., Grimm, B., Goelz, S., & Bille, J. F. (1994). Objective measurement of wave aberrations of the human eye with the use of a Hartmann-Shack wave-front sensor. *JOSA A*, 11(7), 1949-1957.

Llorente, L., Diaz-Santana, L., Lara-Saucedo, D., & Marcos, S. (2003). Aberrations of the human eye in visible and near infrared illumination. *Optometry & Vision Science*, 80(1), 26-35.

Llorente, L., Barbero, S., Cano, D., Dorronsoro, C., & Marcos, S. (2004a). Myopic versus hyperopic eyes: axial length, corneal shape and optical aberrations. *Journal of Vision*, 4(4), 5.

Llorente, L., Barbero, S., Merayo, J., & Marcos, S. (2004b). Total and corneal optical aberrations induced by laser in situ keratomileusis for hyperopia. *Journal of Refractive Surgery*, 20(3).

Locke, L. C., & Somers, W. (1989). A comparison study of dynamic retinoscopy techniques. *Optometry & Vision Science*, 66(8), 540-544.

López-Gil, N., Rucker, F. J., Stark, L. R., Badar, M., Borgovan, T., Burke, S., & Kruger, P. B. (2007). Effect of third-order aberrations on dynamic accommodation. *Vision research*, 47(6), 755-765.

Lowe, R. F. (1972). Anterior lens curvature. Comparisons between normal eyes and those with primary angle-closure glaucoma. *The British journal of ophthalmology*, 56(5), 409.

Lowe, R. F., & Clark, B. A. (1973). Posterior corneal curvature. Correlations in normal eyes and in eyes involved with primary angle-closure glaucoma. *The British journal of ophthalmology*, 57(7), 464.

Lu, C., Munger, R., & Campbell, M. C. W. (1993). Monochromatic aberrations in accommodated eyes. In *Technical digest series Vol. 3, ophthalmic and visual optics 1993* (pp. 160-163).

## M

Maddock, R. J., Millodot, M., Leat, S., & Johnson, C. A. (1981). Accommodation responses and refractive error. *Investigative ophthalmology & visual science*, 20(3), 387-391.

Malacara, D. (1988). *Geometrical and Instrumental Optics* (Academic Press, London)

Mallen, E. A. H., J. S. Wolffsohn, et al. (2001). Clinical evaluation of the Shin-Nippon autorefractor SRW 5000 autorefractor in adults. *Ophthalmic and Physiological Optics*, 21(2): 101-107

Manns, F., Fernandez, V., Zipper, S., Sandadi, S., Hamaoui, M., Ho, A., & Parel, J. M. (2004). Radius of curvature and asphericity of the anterior and posterior surface of human cadaver crystalline lenses. *Experimental eye research*, 78(1), 39-51.

Marcos, S., Burns, S. A., Moreno-Barriuso, E., & Navarro, R. (1999a). A new approach to the study of ocular chromatic aberrations. *Vision research*, 39(26), 4309-4323.

Marcos, S., Moreno, E., & Navarro, R. (1999b). The depth-of-field of the human eye from objective and subjective measurements. *Vision research*, 39(12), 2039-2049.

Marcos S, Moreno-Barriuso E, Llorente L, Navarro R, & Barbero S. (2000). Do myopic eyes suffer from larger amount of aberrations? In: *Thorn F, Troilo D, Gwiazda J, eds. Myopia 2000: Proceedings of the 8<sup>th</sup> International Conference on Myopia. Boston, MA: Conference on Myopia 2000, Inc. 2000: 118–121.*

Marcos, S., & Burns, S. A. (2000). On the symmetry between eyes of wavefront aberration and cone directionality. *Vision research*, 40(18), 2437-2447.

Marcos, S., Barbero, S., Llorente, L., & Merayo-Llodes, J. (2001). Optical response to LASIK surgery for myopia from total and corneal aberration measurements. *Investigative ophthalmology & visual science*, 42(13), 3349-3356.

Marcos, S., Sawides, L., Gamba, E., & Dorronsoro, C. (2008). Influence of adaptive-optics ocular aberration correction on visual acuity at different luminances and contrast polarities. *Journal of Vision*, 8(13), 1.

Marcos, S., Ortiz, S., Pérez-Merino, P., Birkenfeld, J., Durán, S., & Jiménez-Alfaro, I. (2014). Three-dimensional evaluation of accommodating intraocular lens shift and alignment in vivo. *Ophthalmology*, 121(1), 45-55.

Marg, E., & Morgan Jr, M. W. (1949). The pupillary near reflex; the relation of pupillary diameter to accommodation and the various components of convergence. *American journal of optometry and archives of American Academy of Optometry*, 26(5), 183.

- Mathews, S., & Kruger, P. B. (1994). Spatiotemporal transfer function of human accommodation. *Vision Research*, 34(15), 1965–1980.
- McClelland, J. F., & Saunders, K. J. (2003). The repeatability and validity of dynamic retinoscopy in assessing the accommodative response. *Ophthalmic and Physiological Optics*, 23(3), 243-250.
- McLellan, J. S., Marcos, S., & Burns, S. A. (2001). Age-related changes in monochromatic wave aberrations of the human eye. *Investigative ophthalmology & visual science*, 42(6), 1390-1395.
- Miege, C. & Denieul, P. (1988). Mean response and oscillations of accommodation for various stimulus vergences in relation to accommodation feedback control. *Ophthalmic and Physiological Optics*, 8(2), 165–171.
- Moffat, B. A., Atchison, D. A., and Pope, J. M. (2002). Age-related changes in refractive index distribution and power of the human lens as measured by magnetic resonance micro-imaging in vitro. *Vision Research*, 42(13), 1683–1693.
- Mundt, G. H., & Hughes, W. F. (1956). Ultrasonics in ocular diagnosis. *American journal of ophthalmology*, 41(3), 488-498.
- Mutti, D. O., Mitchell, G. L., Hayes, J. R., Jones, L. A., Moeschberger, M. L., Cotter, S. A., Kleinstein, R. N., Manny, R. E., Twelker, J. D., & Zadnik, K. (2006). Accommodative lag before and after the onset of myopia. *Investigative ophthalmology & visual science*, 47(3), 837-846.

## N

- Nangia, V., Jonas, J. B., Sinha, A., Matin, A., Kulkarni, M., & Panda-Jonas, S. (2010). Ocular axial length and its associations in an adult population of central rural India: the Central India Eye and Medical Study. *Ophthalmology*, 117(7), 1360-1366.
- Navarro, R., & Losada, M. A. (1997). Aberrations and relative efficiency of light pencils in the living human eye. *Optometry & Vision Science*, 74(7), 540-547.

## O

- Ortiz, S., Siedlecki, D., Remon, L., & Marcos, S. (2009). Optical coherence tomography for quantitative surface topography. *Applied optics*, 48(35), 6708-6715.
- Ortiz, S., Siedlecki, D., Grulkowski, I., Remon, L., Pascual, D., Wojtkowski, M., & Marcos, S. (2010). Optical distortion correction in optical coherence tomography for quantitative ocular anterior segment by three-dimensional imaging. *Optics express*, 18(3), 2782-2796.
- Ortiz, S., Siedlecki, D., Pérez-Merino, P., Chia, N., de Castro, A., Szkulmowski, M., Wojtkowski M, & Marcos, S. (2011). Corneal topography from spectral optical coherence tomography (sOCT). *Biomedical optics express*, 2(12), 3232-3247.
- Ortiz, S., Pérez-Merino, P., Gamba, E., de Castro, A., & Marcos, S. (2012a). In vivo human crystalline lens topography. *Biomedical optics express*, 3(10), 2471-2488.

Ortiz, S., Pérez-Merino, P., Alejandre, N., Gamba, E., Jimenez-Alfaro, I., & Marcos, S. (2012b). Quantitative OCT-based corneal topography in keratoconus with intracorneal ring segments. *Biomedical optics express*, 3(5), 814-824.

Ortiz, S., Pérez-Merino, P., Durán, S., Velasco-Ocana, M., Birkenfeld, J., de Castro, A., Jiménez-Alfaro, I. & Marcos, S. (2013). Full OCT anterior segment biometry: an application in cataract surgery. *Biomedical optics express*, 4(3), 387-396.

Ostrin, L., Kasthurirangan, S., Win-Hall, D., & Glasser, A. (2006). Simultaneous measurements of refraction and A-scan biometry during accommodation in humans. *Optometry & Vision Science*, 83(9), 657-665.

## P

Paquin, M. P., Hamam, H., & Simonet, P. (2002). Objective measurement of optical aberrations in myopic eyes. *Optometry & Vision Science*, 79(5), 285-291.

Park, B., Pierce, M. C., Cense, B., Yun, S. H., Mujat, M., Tearney, G., Bouma, B. E., & de Boer, J. (2005). Real-time fiber-based multi-functional spectral-domain optical coherence tomography at 1.3  $\mu\text{m}$ . *Optics Express*, 13(11), 3931-3944.

Patel, S., Marshall, J., & Fitzke, F. W. (1992). Shape and radius of posterior corneal surface. *Refractive & corneal surgery*, 9(3), 173-181.

Patel, S., Reinstein, D. Z., Silverman, R. H., & Coleman, D. J. (1998). The shape of Bowman's layer in the human cornea. *Journal of Refractive Surgery*, 14, 636-640.

Pavlin, C. J., Sherar, M. D., & Foster, F. S. (1990). Subsurface ultrasound microscopic imaging of the intact eye. *Ophthalmology*, 97(2), 244-250.

Pérez-Merino, P., Ortiz, S., Alejandre, N., Jiménez-Alfaro, I., & Marcos, S. (2013). Quantitative OCT-Based Longitudinal Evaluation of Intracorneal Ring Segment Implantation in Keratoconus. *Investigative ophthalmology & visual science*, 54(9), 6040-6051.

Phillips, S., & Stark, L. (1977). Blur: a sufficient accommodative stimulus. *Documenta Ophthalmologica*, 43(1), 65-89.

Plainis, S., Ginis, H. S., & Pallikaris, A. (2005). The effect of ocular aberrations on steady-state errors of accommodative response. *Journal of Vision*, 5(5), 7.

Plainis, S., & Pallikaris, I. G. (2006) Ocular monochromatic aberration statistics in a large emmetropic population. 3rd European Meeting in Physiological Optics. London, ENGLAND, Taylor & Francis Ltd.

Podoleanu, A., Charalambous, I., Plesea, L., Dogariu, A., & Rosen, R. (2004). Correction of distortions in optical coherence tomography imaging of the eye. *Physics in medicine and biology*, 49(7), 1277.

Porter, J., Guirao, A., Cox, I. G., & Williams, D. R. (2001). Monochromatic aberrations of the human eye in a large population. *JOSA A*, 18(8), 1793-1803.

Povazay, B., Bizheva, K., Unterhuber, A., Hermann, B., Sattmann, H., Fercher, A. F., Drexler, W., Apolonski, A., Wadsworth, W. J., Knight, J. C., Russell, P. St. J., Vetterlein, M. & Scherzer, E. (2002). Submicrometer axial resolution optical coherence tomography. *Optics letters*, 27(20), 1800-1802.

Prydal, J. I., Artal, P., Woon, H., & Campbell, F. W. (1992). Study of human precorneal tear film thickness and structure using laser interferometry. *Investigative ophthalmology & visual science*, 33(6), 2006-2011.

## R

Radhakrishnan, S., Huang, D., & Smith, S. D. (2005). Optical coherence tomography imaging of the anterior chamber angle. *Ophthalmology Clinics of North America*, 18(3), 375-81.

Richdale, K., Bullimore, M. A., & Zadnik, K. (2008). Lens thickness with age and accommodation by optical coherence tomography. *Ophthalmic and Physiological Optics*, 28(5), 441-447.

Roorda, A., Bobier, W. R., & Campbell, M. C. (1998). An infrared eccentric photometer. *Vision research*, 38(13), 1913-1924.

Rosales, P., Dubbelman, M., Marcos, S., & Van der Heijde, R. (2006). Crystalline lens radii of curvature from Purkinje and Scheimpflug imaging. *Journal of Vision*, 6(10), 5.

Rosales, P., Wendt, M., Marcos, S., & Glasser, A. (2008). Changes in crystalline lens radii of curvature and lens tilt and decentration during dynamic accommodation in rhesus monkey. *Journal of Vision* 8,(1) 1-12.

Rosales, P., & Marcos, S. (2009). Pentacam Scheimpflug Quantative Imaging of the crystalline lens and intraocular lens. *Journal of Refractive Surgery*, 25(5), 421-428.

Royston, J. M., Dunne, M. C. M., & Barnes, D. A. (1990). Measurement of the posterior corneal radius using slit lamp and Purkinje image techniques. *Ophthalmic and Physiological Optics*, 10(4), 385-388.

Ruggeri, M., Uhlhorn, S. R., De Freitas, C., Ho, A., Manns, F., & Parel, J. M. (2012). Imaging and full-length biometry of the eye during accommodation using spectral domain OCT with an optical switch. *Biomedical optics express*, 3(7), 1506-1520.

## S

Salaroli, C. H. R., Li, Y., & Huang, D. (2009). High-resolution optical coherence tomography visualization of LASIK flap displacement. *Journal of Cataract & Refractive Surgery*, 35(9), 1640-1642.

Salmon, T. O., & van de Pol, C. (2006). Normal-eye Zernike coefficients and root-mean-square wavefront errors. *Journal of Cataract & Refractive Surgery*, 32(12), 2064-2074.

Santamaría, J., Artal, P., & Bescós, J. (1987). Determination of the point-spread function of human eyes using a hybrid optical-digital method. *JOSA A*, 4(6), 1109-1114.

Satoh, N., Shimizu, K., Goto, A., Igarashi, A., Kamiya, K., & Ohbayashi, K. (2013). Accommodative changes in human eye observed by Kitasato anterior segment optical coherence tomography. *Japanese journal of ophthalmology*, 57(1), 113-119.

Savini, G., Goto, E., Carbonelli, M., Barboni, P., & Huang, D. (2009). Agreement between Stratus and Visante optical coherence tomography systems in tear meniscus measurements. *Cornea*, 28(2), 148-151.

- Schachar, R. A. (1993). Zonular function: a new hypothesis with clinical implications. *Annals of ophthalmology*, 26(2), 36-38.
- Schachar, R. A., Cudmore, D. P., & Black, T. D. (1993). Experimental support for Schachar's hypothesis of accommodation. *Annals of ophthalmology*, 25(11), 404-409.
- Schaeffel, F., Farkas, L., & Howland, H. C. (1987). Infrared photoretinoscope. *Applied Optics*, 26(8), 1505-1509.
- Schaeffel, F., Wilhelm, H., & Zrenner, E. (1993). Inter-individual variability in the dynamics of natural accommodation in humans: relation to age and refractive errors. *The Journal of Physiology*, 461(1), 301-320.
- Schuman, J. S., Hee, M. R., Arya, A. V., Pedut-Kloizman, T., Puliafito, C. A., Fujimoto, J. G., & Swanson, E. A. (1995). Optical coherence tomography: a new tool for glaucoma diagnosis. *Current opinion in ophthalmology*, 6(2), 89-95.
- Shao, Y., Tao, A., Jiang, H., Shen, M., Zhong, J., Lu, F., & Wang, J. (2013). Simultaneous real-time imaging of the ocular anterior segment including the ciliary muscle during accommodation. *Biomedical optics express*, 4(3), 466-480.
- Shen, M., Wang, M. R., Yuan, Y., Chen, F., Karp, C. L., Yoo, S. H., & Wang, J. (2010). SD-OCT with prolonged scan depth for imaging the anterior segment of the eye. *Ophthalmic Surgery Lasers and Imaging* 41(6), 65-69.
- Silverman, R. H. (2009). High-resolution ultrasound imaging of the eye—a review. *Clinical & experimental ophthalmology*, 37(1), 54-67.
- Smith, G. (1983). The accommodative resting states, instrument accommodation and their measurement. *Journal of Modern Optics*, 30(3), 347-359.
- Smith, G., Cox, M. J., Calver, R., & Garner, L. F. (2001). The spherical aberration of the crystalline lens of the human eye. *Vision research*, 41(2), 235-243.
- Smithline L. M. (1974). Accommodative response to blur. *Journal of the Optical Society of America*, 64(11), 1512–1516
- Stark, L., Takahashi, Y., & Zames, G. (1965). Nonlinear servoanalysis of human lens accommodation. *Systems Science and Cybernetics, IEEE Transactions on*, 1(1), 75-83.
- Stark, L. R., & Atchison, D. A. (1997). Pupil size, mean accommodation response and the fluctuations of accommodation. *Ophthalmic and Physiological Optics*, 17(4), 316-323.
- Stark, L. R., Lee, R. S., Kruger, P. B., Rucker, F. J., & Fan, H. Y. (2002). Accommodation to simulations of defocus and chromatic aberration in the presence of chromatic misalignment. *Vision Research*, 42(12), 1485–1498.
- Stark, L. R., Strang, N. C., & Atchison, D. A. (2003). Dynamic accommodation response in the presence of astigmatism. *JOSA A*, 20(12), 2228-2236.
- Stark, L. R., Kruger, P. B., Rucker, F. J., Swanson, W. H., Schmidt, N., Hardy, C., et al. (2009). Potential signal to accommodation from the Stiles–Crawford effect and ocular monochromatic aberrations. *Journal of Modern Optics*, 56(20), 2203–2216.
- Strenk, S.A., Semmlow, J.L., & Strenk, L.M. (1999). Age-related changes in human ciliary muscle and the lens: a magnetic resonance imaging study. *Invest. Ophthalmol. Vis. Science*, 40, 1162:1169.

Strenk, S. A., Strenk, L. M., Semmlow, J. L., & DeMarco, J. K. (2004). Magnetic resonance imaging study of the effects of age and accommodation on the human lens cross-sectional area. *Investigative ophthalmology & visual science*, 45(2), 539-545.

Strenk, S. A., Strenk, L. M., & Koretz, J. F. (2005). The mechanism of presbyopia. *Progress in retinal and eye research*, 24(3), 379-393.

Sun, M., Birkenfeld, J., de Castro, A., Ortiz, S., & Marcos, S. (2014). OCT 3-D surface topography of isolated human crystalline lenses. *Biomedical optics express*, 5(10), 3547-3561.

Swanson, E. A., Izatt, J. A., J. S., Hee, Huang, D., Lin, C. P., Schuman, M. R., Puliafito, C. A., & Fujimoto, J. G. (1993). In vivo retinal imaging by optical coherence tomography. *Optics letters*, 18(21), 1864-1866.

Szkulmowski, M., Grulkowski, I., Szlag, D., Szkulmowska, A., Kowalczyk, A., & Wojtkowski, M. (2009). Flow velocity estimation by complex ambiguity free joint Spectral and Time domain Optical Coherence Tomography. *Optics express*, 17(16), 14281-14297.

## T

Takada, K., Yokohama, I., Chida, K., & Noda, J. (1987). New measurement system for fault location in optical waveguide devices based on an interferometric technique. *Applied optics*, 26(9), 1603-1606.

Tamm, S., Tamm, E., & Rohen, J. W. (1992). Age-related changes of the human ciliary muscle. A quantitative morphometric study. *Mechanisms of ageing and development*, 62(2), 209-221.

Tang, M., Li, Y., Avila, M., & Huang, D. (2006). Measuring total corneal power before and after laser in situ keratomileusis with high-speed optical coherence tomography. *Journal of Cataract & Refractive Surgery*, 32(11), 1843-1850.

Theagarayan, B., Radhakrishnan, H., Allen, P. M., Calver, R. I., Rae, S. M., & O'Leary, D. J. (2009). The effect of altering spherical aberration on the static accommodative response. *Ophthalmic and Physiological Optics*, 29(1), 65-71.

Thibos, L. N., Applegate, R. A., Schwiegerling, J. T., & Webb, R. (2002a). Standards for reporting the optical aberrations of eyes. *Journal of Refractive Surgery*, 18(5), S652-S660.

Thibos, L. N., Hong, X., Bradley, A., & Cheng, X. (2002b). Statistical variation of aberration structure and image quality in a normal population of healthy eyes. *JOSA A*, 19(12), 2329-2348.

Thibos, L. N., Hong, X., Bradley, A., & Applegate, R. A. (2004). Accuracy and precision of objective refraction from wavefront aberrations. *Journal of Vision*, 4(4), 9.

Thorn, F., Held, R., Gwiazda, J., & He, J.C. (2003). Patent Application. US2003/0058404 A1 US.

Tscherning, M. H. E. (1920). *Physiologic Optics: Dioptrics of the Eye, Functions of the Retina Ocular Movements and Binocular Vision*. Keystone Publishing Company.

Tucker, J., & Charman, W. N. (1979). Reaction and response times for accommodation. *American journal of optometry and physiological optics*, 56(8), 490-503.

## U

Uhlhorn, S. R., Borja, D., Manns, F., & Parel, J. M. (2008). Refractive index measurement of the isolated crystalline lens using optical coherence tomography. *Vision research*, 48(27), 2732-2738.

## V

van der Heijde, G. L., Beers, A. P. A., & Dubbelman, M. (1996). Microfluctuations of steady-state accommodation measured with ultrasonography. *Ophthalmic and Physiological Optics*, 16(3), 216-221.

Vilupuru, A. S., & GLASSER, A. (2003). Dynamic accommodative changes in rhesus monkey eyes assessed with A-scan ultrasound biometry. *Optometry & Vision Science*, 80(5), 383-394.

## W

Walsh, G., & Charman, W. N. (1989). The effect of defocus on the contrast and phase of the retinal image of a sinusoidal grating. *Ophthalmic and Physiological Optics*, 9(1), 398-404.

Wang, L., & Koch, D. D. (2003). Anterior corneal optical aberrations induced by laser in situ keratomileusis for hyperopia. *Journal of Cataract & Refractive Surgery*, 29(9), 1702-1708.

Westphal, V., Rollins, A., Radhakrishnan, S., & Izatt, J. (2002). Correction of geometric and refractive image distortions in optical coherence tomography applying Fermat's principle. *Optics Express*, 10(9), 397-404.

Wilson, B. J., Decker, K. E., & Roorda, A. (2002). Monochromatic aberrations provide an odd-error cue to focus direction. *JOSA A*, 19(5), 833-839.

Winn, B., Pugh, J. R., Gilmartin, B., & Owens, H. (1990). Arterial pulse modulates steady-state ocular accommodation. *Current eye research*, 9(10), 971-975.

Winn, B., & Gilmartin, B. (1992). Current perspective on microfluctuations of accommodation. *Ophthalmic and Physiological Optics*, 12(2), 252-256.

Wojtkowski, M., Bajraszewski, T., Targowski, P., & Kowalczyk, A. (2003). Real-time in vivo imaging by high-speed spectral optical coherence tomography. *Optics letters*, 28(19), 1745-1747.

Wolfe, J. M., & O'Connell, K. M. (1987). Adaptation of the resting states of accommodation. *Investigative ophthalmology & visual science*, 28(6), 992-996.

## Y

Yadav, R., Ahmad, K., & Yoon, G. (2010). Scanning system design for large scan depth anterior segment optical coherence tomography. *Optics letters*, 35(11), 1774-1776.

Youngquist, R. C., Carr, S., & Davies, D. E. (1987). Optical coherence-domain reflectometry: a new optical evaluation technique. *Optics Letters*, *12*(3), 158-160.

Yun, S., Tearney, G., de Boer, J., Iftimia, N., & Bouma, B. (2003). High-speed optical frequency-domain imaging. *Optics Express*, *11*(22), 2953-2963.

## Z

Zadnik, K., Mutti, D. O., & Adams, A. J. (1992). The repeatability of measurement of the ocular components. *Investigative ophthalmology & visual science*, *33*(7), 2325-2333.

Zadnik, K., Mutti, D.O., Fusaro, R.E., & Adams, A.J. (1995). Longitudinal evidence of crystalline lens thinning in children. *Invest. Ophthalmol. Vis. Sci.*, *36*, 1581-1587.

Zernike, F. (1934). Diffraction theory of the knife-edge test and its improved form, the phase-contrast method. *Monthly Notices of the Royal Astronomical Society*, *94*, 377-384.

Zhao, M., Kuo, A. N., & Izatt, J. A. (2010). 3D refraction correction and extraction of clinical parameters from spectral domain optical coherence tomography of the cornea. *Optics express*, *18*(9), 8923-8936.

Zhou, C., Wang, J., & Jiao, S. (2009). Dual channel dual focus optical coherence tomography for imaging accommodation of the eye. *Optics express*, *17*(11), 8947-8955.

## AGRADECIMIENTOS

*La realización de esta tesis ha llevado tanto tiempo que la sección de agradecimientos tiene que estar a la altura. Espero no dejarme a nadie, pero pido disculpas por adelantado porque sé que será imposible.*

*Ante todo, gracias a Susana por dirigirme esta tesis de manera siempre clara, por ofrecerme la oportunidad de asistir a numerosos congresos científicos y de enriquecer mi experiencia investigadora con dos estancias breves. Gracias también por tu insistencia para que este trabajo no quedara inconcluso. Pero sobre todo me quedo con tu ejemplo científico, con tu pasión y dedicación.*

*Tengo mucho que agradecer a mis padres por su ejemplo de esfuerzo y sacrificio, a un nivel que yo nunca seré capaz de llegar. Y en especial a mi madre, por haberme dado una educación tratando de pulir mis talentos y mejorar mis defectos. Gracias también por aceptarme como soy y haberme dejado la libertad de elegir lo que quería, aún cuando yo no lo tuviera del todo claro. También quiero agradecer a mis tíos Luis y María Jesús-mis segundos padres- y a mis hermanos por estar siempre ahí cuando lo he necesitado.*

*A lo largo de mi educación tuve algunos profesores clave que influyeron en mi carrera científica a los que quiero recordar, como Margarita Cubillo e Isabel Lanas en el Instituto Navarro Villoslada de Pamplona, o Miguel Ángel Rebolledo, Jesús Atencia y Vicky Collados en la Universidad de Zaragoza. Algún día espero devolver a otros lo que ellos me dieron.*

*Y qué decir de mis compañeros de clase en la Universidad, en especial de Pepa, mi compañera de prácticas durante tantos años. O también de mis compañeras de piso (Salas, Itziar, Cristina, Elena) con las que aprendí a convivir y que hicieron tan llevadero eso de estar lejos de casa.*

*Y ya en Madrid, tengo mucho que agradecer a mis compañeros del Grupo de Óptica y Biofotónica del Instituto de Óptica: en primer lugar a Lucie, con quien tanto aprendí por su experiencia previa con Óptica Adaptativa y tan bien lo pasé los primeros meses en el laboratorio. A Lourdes, por sus consejos, experiencia, ejemplo y muchas conversaciones por los pasillos; a Carlos por su ayuda en muchos momentos y por su visión; a Sergio Barbero por su ejemplo distinto, pero mucho más por su compañía, sus excursiones y el tiempo compartido bajo un mismo techo; A Alberto por su divertida seriedad que tanto admiro; a María por insuflar vida allá donde pasa y por revolucionar el despacho; a Sergio Ortiz, por su enorme ayuda con las imágenes de OCT y su inigualable capacidad de trabajo, además de ese sentido del humor aragonés; a Judith, por esos bailes y risas en el sótano; a Pablo de Gracia, por los algoritmos de simulación de la PSF y sus originales punto de vista; a Patricia y Requejo por facilitarme la adaptación. A Laura, por su buen humor y disposición a ayudar... Pero sobre todo a Pablo Pérez, por tantos momentos compartidos dentro y fuera: el mundo sería mucho mejor si todosuviésemos un PPM en nuestras vidas.*

*I do not want to forget all the people I met during my short stays at New York and Berkeley. Thank you very much to Phil Kruger and Cliff Schor, and to all their students: Yinan, Kathy, Humza... I had a very good time working in both places, and I learned a lot from them.*

*También me quiero acordar del resto de compañeros y amigos del IO: Elena, Sara, Andrés, Dani, Rafa, Jesús... y muchos otros que no nombro para no extenderme. Gracias a todos por crear un ambiente tan agradable y divertido, fuera y dentro del CSIC. Y también quiero recordar a todos los integrantes del IOSA, por el éxito en la creación del grupo y la gran experiencia vivida durante su creación y funcionamiento. Para mí es uno de los mejores recuerdos de mi etapa en el CSIC.*

*And thank you very much to all my colleagues at i-Óptics (Dirk, Wouter, Harry, Yannis...) for keeping asking the uncomfortable question: when are you going to finish your PhD? And to all my friends in Delft, for all these funny moments.*

*No quiero terminar sin acordarme de mi cuadrilla de amigos de Pamplona (Gonzalo, Amaia,...). Por más vueltas que dé por el mundo, siempre cuento con su apoyo y amistad, que s que no perderé nunca aunque muchas veces descuide por la distancia.*

*Y por supuesto, y sobre todo, esta tesis no habría llegado a buen puerto después de una travesía tan larga sin el apoyo del otro Enrique. Gracias por estar ahí todos los días, ahora a mi lado, antes al otro lado del teléfono, pero siempre apoyándome, animándome a seguir y pinchándome lo suficiente para que no lo dejase pasar. Ahora, por fin, ya se ha terminado. Lo de la tesis, porque lo nuestro es para siempre.*



